Chem Soc Rev

REVIEW ARTICLE

View Article Online
View Journal | View Issue

Check for updates

Cite this: *Chem. Soc. Rev.*, 2017, **46**, 4042

Electromagnetic theories of surface-enhanced Raman spectroscopy

Song-Yuan Ding, *[ab] En-Ming You, [a] Zhong-Qun Tian [ab] and Martin Moskovits *[c]

Surface-enhanced Raman spectroscopy (SERS) and related spectroscopies are powered primarily by the concentration of the electromagnetic (EM) fields associated with light in or near appropriately nanostructured electrically-conducting materials, most prominently, but not exclusively high-conductivity metals such as silver and gold. This field concentration takes place on account of the excitation of surface-plasmon (SP) resonances in the nanostructured conductor. Optimizing nanostructures for SERS, therefore, implies optimizing the ability of plasmonic nanostructures to concentrate EM optical fields at locations where molecules of interest reside, and to enhance the radiation efficiency of the oscillating dipoles associated with these molecules and nanostructures. This review summarizes the development of theories over the past four decades pertinent to SERS, especially those contributing to our current understanding of SP-related SERS. Special emphasis is given to the salient strategies and theoretical approaches for optimizing nanostructures with hotspots as efficient EM near-field concentrating and far-field radiating substrates for SERS. A simple model is described in terms of which the upper limit of the SERS enhancement can be estimated. Several experimental strategies that may allow one to approach, or possibly exceed this limit, such as cascading the enhancement of the local and radiated EM field by the multiscale EM coupling of hierarchical structures, and generating hotspots by hybridizing an antenna mode with a plasmonic waveguide cavity mode, which would result in an increased local field enhancement, are discussed. Aiming to significantly broaden the application of SERS to other fields, and especially to material science, we consider hybrid structures of plasmonic nanostructures and other material phases and strategies for producing strong local EM fields at desired locations in such hybrid structures. In this vein, we consider some of the numerical strategies for simulating the optical properties and consequential SERS performance of particle-on-substrate systems that might guide the design of SERS-active systems. Finally, some current theoretical attempts are briefly discussed for unifying EM and non-EM contribution to SERS.

Received 3rd April 2017

DOI: 10.1039/c7cs00238f

rsc.li/chem-soc-rev

Published on 29 Junie 2017. Downloaded by Fail Open on 2025-05-07 9:23:53 vm..

1 Introduction

Surface-enhanced Raman scattering is a phenomenon associated with the amplification by several orders of magnitude of Raman signals of analytes located at or very close to metallic nanostructures. It is almost universally accepted that the enhancement is largely due to the amplification of the local electromagnetic (EM) fields owing to the excitation of surface-plasmon resonance.[1–5] SERS can provide rich structural information at the molecular level with a sensitivity that is often comparable to that of fluorescence. Ultrahigh SERS sensitivity even down to the single-molecule level can be achieved on some well-designed coinage-metal (for example, Au and Ag) nanostructures.[6–9] After four decades of development, SERS is now being applied to trace-molecule detection, biomolecule analysis and material characterization, among multiple other applications. The discovery and development of SERS also contributed significantly to the current interest in and development of the field of plasmonics, which traces its roots back to the discoveries in the 1970s related to SERS.

SERS enhancement strongly depends on the characteristics of the laser excitation (*e.g.* wavelength, polarization and incident direction), detection configuration (*e.g.* scattering configuration, polarizer, solid angle for collection), the intrinsic Raman cross-section of probe molecules or materials, the dielectric properties of the ambient environment and the optical properties of SERS substrates.[4] A great deal of current research has been devoted to the optimization of SERS substrates for high enhancement and

---

[a] *State Key Laboratory of Physical Chemistry of Solid Surfaces (PCOSS), Collaborative Innovation Centre of Chemistry for Energy Materials (iChEM), and Department of Chemistry, College of Chemistry and Chemical Engineering, Xiamen University, Xiamen 361005, China. E-mail: syding@xmu.edu.cn*

[b] *Graphene Industry and Engineering Research Institute, Xiamen University, Xiamen 361005, China*

[c] *Department of Chemistry and Biochemistry, University of California, Santa Barbara, California, 93106, USA. E-mail: moskovits@chem.ucsb.edu*

This journal is © The Royal Society of Chemistry 2017

Published on 29 Junie 2017. Downloaded by Fail Open on 2025-05-07 9:23:53 vm..

for greater ease of use. Beginning with its discovery on roughened silver electrodes,[10–12] the history of SERS is largely the story of the development of SERS substrates.[5] In the 1970s and 1980s, the SERS-active substrates explored largely consisted of roughened Au and Ag electrodes, island films, colloidal aggregates and surfaces structures using microlithographic techniques[3,10–14] (Fig. 1). Thereafter, SERS benefited considerably from the developments made in nanoscience and nanotechnology in the 1990s,[15] including new synthesis methods of SERS-active nanoparticles (NPs), nanofabrication methods of structured surfaces and powerful analysis methods for characterizing the prepared nanostructures. Au and Ag nanoparticles with nanometre-sized gaps; nanometre-sized shells; nanometre-sized tips, edges and structured surfaces with nanometre-sized holes, voids, bumps, grooves or ridges were among the nanostructures used for SERS (Fig. 1).[6,15,17–27,29,30]

Most SERS-active substrates are based on Au or Ag metals because the metal nanostructures can support surface plasmons, the collective oscillating modes of the conduction electrons at metal/dielectric interfaces.[1,31,32] Nanomaterials that can support surface plasmons are referred to as plasmonic materials.[33,34] Surface plasmons are often separated into two categories: (i) localized surface plasmons (LSP, as shown in Fig. 2a), in which the electrons coherently oscillate locally within and in the vicinity of a nanostructure and (ii) propagating surface plasmons or surface-plasmon polaritons (SPPs, as shown in Fig. 2b), in which the coherent electron oscillation propagates as a longitudinal wave along the metal surface.[31,35,36]

LSPs in plasmonic nanomaterials can be excited by far-field incident light, whose energy can be consequentially concentrated at nanoscale features, *i.e.* edges, tips or crevices, to enhance the local EM field intensity by 2–5 orders of magnitude. LSPs can also be excited by local oscillating sources (dipoles, quadrupoles, *etc.*), which re-radiate into the far field by means of the plasmonic nanostructures.[5] Nanomaterials with strategically

Song-Yuan Ding

Song-Yuan Ding received his BSc in Chemical Physics at the University of Science and Technology of China in 2005 and his PhD in Chemistry under the supervision of Prof. Zhong-Qun Tian at Xiamen University in 2012. He is a Research Fellow in the Collaborative Innovation Center of Chemistry for Energy Materials (iChEM) at Xiamen University. Currently, his research interests include surface-enhanced Raman spectroscopy for general materials, AFM-based infrared and Raman nanospectroscopy and imaging, ab initial interfacial electrochemistry and the theory of catalyzed molecular assembly.

En-Ming You

En-Ming You received his BSc at Nanjing University. He is now a PhD student at Xiamen University under the supervision of Prof. Zhong-Qun Tian and Dr Song-Yuan Ding working on surface-enhanced Raman spectroscopy, AFM-based infrared nanospectroscopy and imaging.

Zhong-Qun Tian

Zhong-Qun Tian obtained his BSc at Xiamen University in 1982 and his PhD under the supervision of Prof. Martin Fleischmann at the University of Southampton in 1987. He has been a full Professor of Chemistry at Xiamen University since 1991. Professor Tian is a Member of the Chinese Academy of Sciences and the Elected President of the International Society of Electrochemistry. Currently, his main research interests include surface-enhanced Raman spectroscopy, spectroelectrochemistry, nanochemistry, plasmonics and catalyzed molecular assembly.

Martin Moskovits

Martin Moskovits has degrees in Physics and Chemistry from the University of Toronto, where he obtained his PhD in Chemical Physics in 1971. He has been a full professor since 1982 and has been working at the University of California, Santa Barbara, since 2000. Professor Moskovits is a Fellow of the American Association for the Advancement of Science, a Fellow of the Optical Society of America and a Fellow of the Royal Society of Canada. His research interests include surface-enhanced Raman spectroscopy, generally and more recently as applied to biosensing, plasmonics for sustainable energy and nanomaterials and nanoelectronics.

Published on 29 Junie 2017. Downloaded by Fail Open on 2025-05-07 9:23:53 vm..

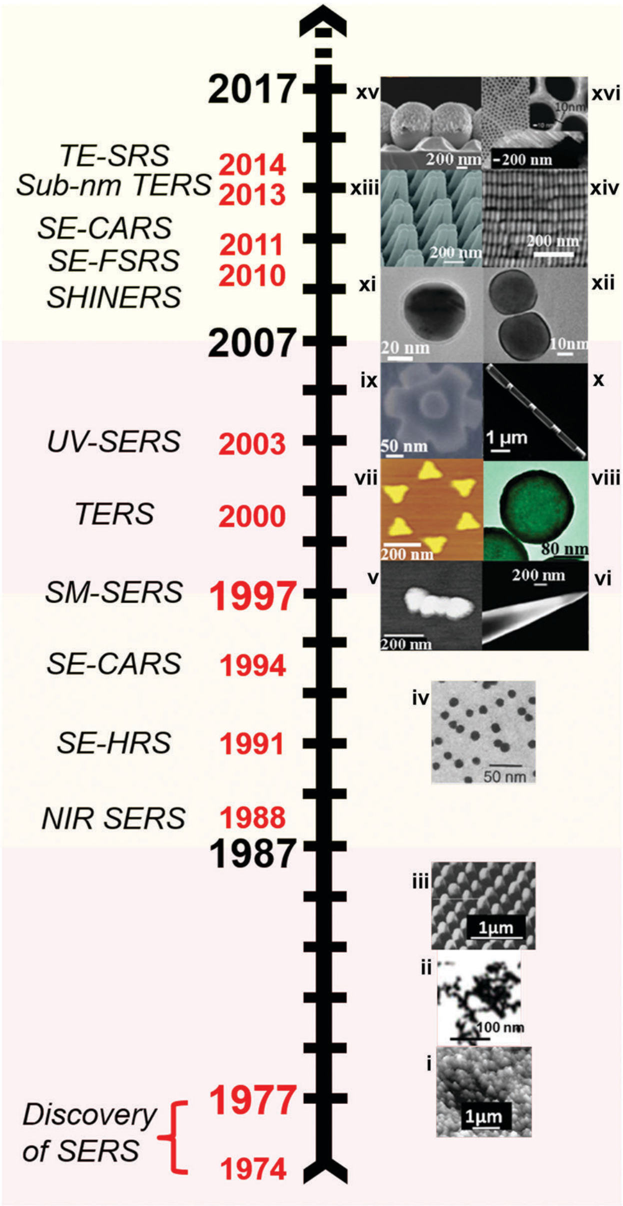

Fig. 1 Milestones related to SERS. Development of new methods of plasmon-enhanced Raman spectroscopies (left), and representative SERS-active substrates (right) in the past four decades. For the full names of the abbreviations of the SERS methods, please see the main text. Image (ii) adapted from ref. 16 with permission, copyright (1981) Elsevier; image (iii) adapted from ref. 14 with permission, copyright (1981) Elsevier; image (iv) adapted from ref. 17 with permission, copyright (1995) AAAS; image (v) adapted from ref. 6 with permission, copyright (1997) AAAS; image (vi) adapted from ref. 15 with permission, copyright (2007) Royal Society of Chemistry; image (vii) adapted from ref. 18 with permission, copyright (2003) American Chemical Society; image (viii) adapted from ref. 19 with permission, copyright (2007) American Chemical Society; image (ix) adapted from ref. 20 with permission, copyright (2010) American Chemical Society; image (x) adapted from ref. 21 with permission, copyright (2006) National Academy of Sciences; image (xi) adapted from ref. 22 with permission, copyright (2010) Nature Publishing group; Image (xii) adapted from ref. 23 with permission, copyright (2009) American Chemical Society; image (xiii) adapted from ref. 24 with permission, copyright (2010) American Chemical Society; image (xiv) adapted from ref. 25 with permission, copyright (2011) National Academy of Sciences; image (xv) adapted from ref. 26 with permission, copyright (2013) American Chemical Society; image (xvi) adapted from ref. 27 with permission, copyright (2015) Wiley-VCH Verlag GmbH & Co kGaA, Weinheim.

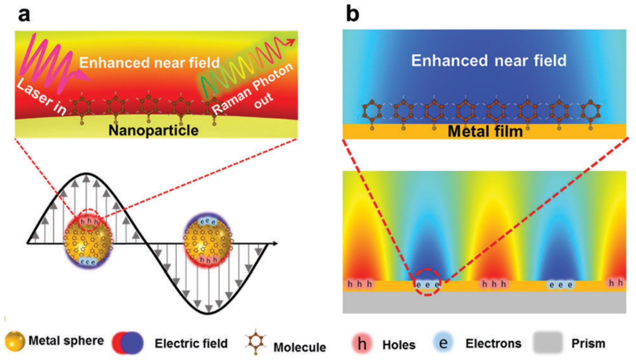

Fig. 2 (a) Localized surface plasmon, and (b) surface-plasmon polariton. Image adapted from ref. 28 with permission. Copyright (2017) American Chemical Society.

tailored plasmonic characteristics have greatly expanded the application of SERS.[37–43]

Understanding such LSPR-based mechanisms of local EM field enhancement also led to the development of a wide range of surface-enhanced Raman methods, including two important variants of SERS: tip-enhanced Raman spectroscopy (TERS)[44–47] and shell-isolated nanoparticle-enhanced Raman spectroscopy (SHINERS),[22] as well as ultraviolet SERS[48,49] and near-infrared SERS.[50] Other Raman spectroscopies inspired by SERS, such as surface-enhanced Raman optical activity (SE-ROA) spectroscopy[51,52] and surface-enhanced nonlinear Raman spectroscopy including surface-enhanced coherent anti-Stokes Raman spectroscopy (SE-CARS),[53,54] surface-enhanced femtosecond stimulated Raman spectroscopy (SE-FSRS),[55] tip-enhanced stimulated Raman spectroscopy (TE-SRS)[56] and surface-enhanced hyper-Raman spectroscopy (SE-HRS)[57] have also been reported.[58] Collectively, the above-mentioned techniques are often referred to as plasmon-enhanced Raman spectroscopy (PERS),[59] whose timeline of key developments is summarized in Fig. 1.

Parallel to the development of SERS-active substrates, theoretical advances in our understanding of the SERS mechanism have directed the development of the field, guiding the development of new design and synthesis strategies for producing high functioning SERS nanostructures, and broadening the range of applications to which SERS can be applied. The milestones in the development of SERS with emphasis on classical electrodynamics are summarised in Fig. 3.

Prior to 1985, several mechanisms were proposed to account for SERS.[1,60–67] SERS is normally performed on molecules that form chemical bonds of varying strengths and complexities with metallic surfaces. Such surface chemical interactions must themselves be understood in order to interpret the SERS spectrum appropriately. The plasmonic model for SERS was developed between the late 1970s and the mid-1980s, primarily by Moskovits,[2,68] Creighton,[3,69,70] Chen,[71] Chang,[72,73] Pettinger,[74] Tsang,[75] Gersten,[76,77] Gersten and Nitzan,[78] McCall,[79,80] Kerker,[63,81,82] Metiu,[64,83,84] and Schatz,[65,85,86] among others (Fig. 3).

In 1973, Dignam and Moskovits reported that the optical properties of rough metal films could be understood if one assumed that the roughness layer behaved as an effective

Published on 29 Junie 2017. Downloaded by Fail Open on 2025-05-07 9:23:53 vm..

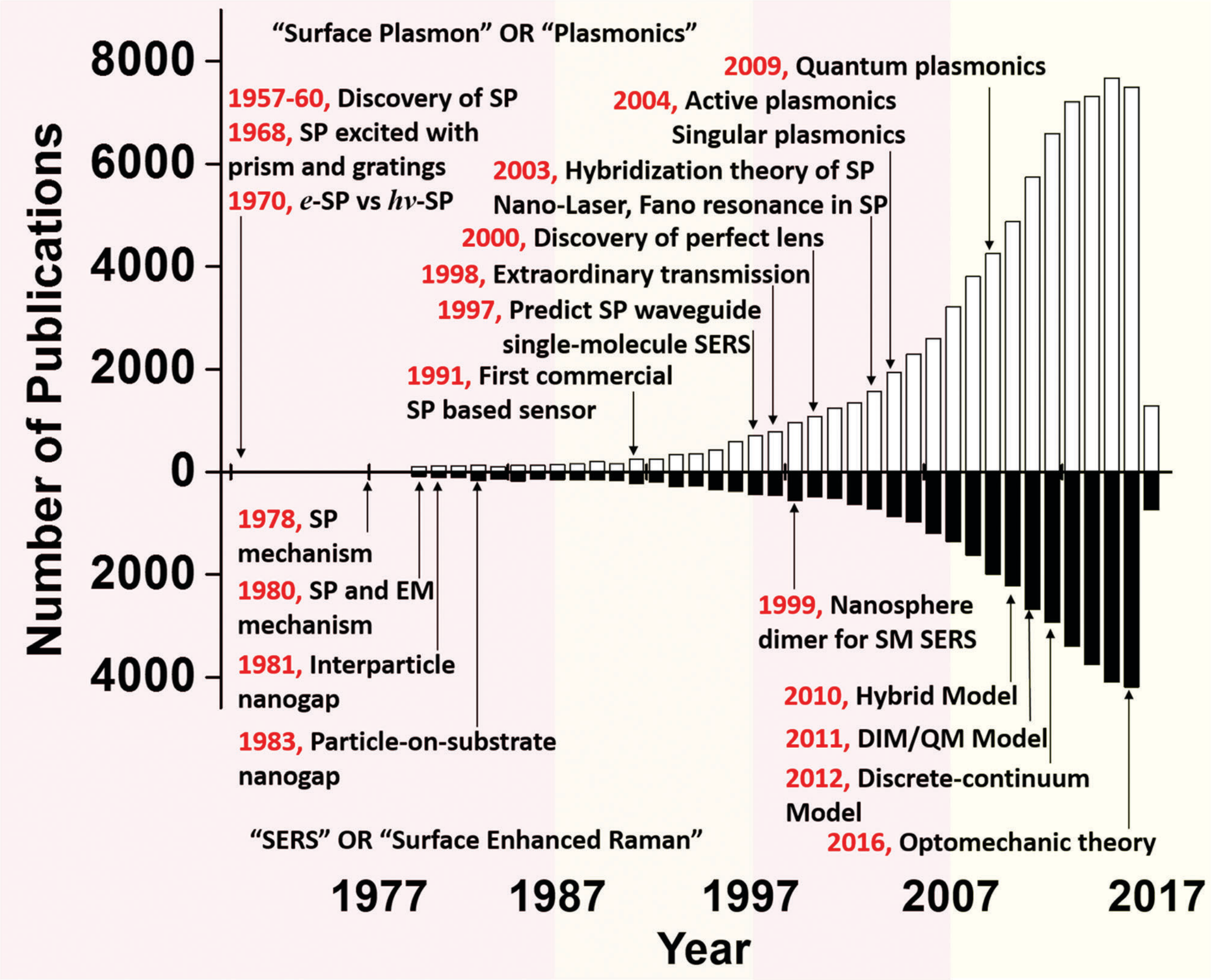

Fig. 3 Milestones related to surface plasmon (up), and surface-plasmon-based SERS theory (down). The number of publications in the 1977–2017 period searched through the ISI Web of Science® using the keywords 'surface plasmon' OR 'plasmonics' from 1973 to 2017. The number of publications in the 1977–2017 period searched through the ISI Web of Science® using the keywords 'SERS' OR 'surface-enhanced Raman' from 1977 to 2017. The abbreviations in this figure: surface plasmon for SP, electromagnetic for EM, discrete interaction model/quantum mechanics for DIM/QM.

medium of nanoparticles, which, for metals such as Cu and Ag showed plasmonic resonances.[87] Moskovits applied this idea to interpret the SERS effect in 1978, and used it to account for the opposite wavelength-dependent SERS intensity trends reported by van Duyne and Creighton, ascribing the difference to the differing roughening procedures of the silver electrodes. Taking the argument further, Moskovits predicted that similar enhancements would be observed in true silver and copper colloids covered with adsorbates.[2]

In 1979, Creighton and coworkers published a comprehensive paper on SERS from Ag/Au colloidal surfaces,[3] in which they correlated the sizes and materials of metallic colloids and the wavelength of SPR with SERS. The authors pointed that it was the surface plasma resonance of metallic colloids or Mie scattering that leads to the giant surface-enhanced Raman effect, which the authors called 'plasma resonance-enhanced Raman'. Finally, Creighton and coworkers concluded that the dielectric functions of the metal colloids determined which materials were effective for SERS. Creighton's pioneering work expanded the range of SERS substrates beyond electrochemically roughened electrodes or cold deposited surfaces to include colloidal particles, at the same time augmenting interest in the use of SERS to a broad scientific and engineering community embracing such disciplines as electrochemistry, heterogeneous catalysis, biochemistry, polymer science, *etc.*

Creighton and coworkers showed that the aggregation of Ag/Au colloids resulted in more intense SERS spectra,[69] leading, in time, to one of the key concepts in SERS: the SERS hotspot. In 1981, Metiu and coworkers calculated the extinction and local field enhancement of a nanosphere dimer as a function of the inter-particle distance.[83] In 1983, Metiu and coworkers also calculated the local field enhancement in a structure consisting of a metallic sphere approaching a flat metallic surface.[84] The two results predicted that Au or Ag nanoparticle dimers, or particle-on-film plasmonic nanostructures with nanogaps, would be uniquely important in generating intense SERS. These two theoretical

Published on 29 Junie 2017. Downloaded by Fail Open on 2025-05-07 9:23:53 vm..

papers founded the notion of the SERS hotspot, and the larger insight that most SERS spectra were dominated by the Raman scattering from such hotspots, which could oftentimes be few in number.

The dominant role that nanoparticle dimers or aggregates with clefts or nanogaps played was not well recognized by a large portion of the SERS community even after the revolutionary discovery of single-molecule SERS (SM-SERS)[6,7] in 1997. In 1999, Käll and coworkers calculated the local field enhancement in a Ag nanosphere dimer by analytically solving the full electrodynamic equations pertinent to generalized Mie theory, and experimentally proposed that the SERS of single-molecule haemoglobin was due to molecules situated between Ag nanoparticles.[88]

Over 2500 articles involving SERS currently appear per year (according to the Web of Science using the keywords 'SERS' OR 'surface-enhanced Raman'); also, over 500 review articles on SERS and related topics have appeared. These have comprehensively covered the development of the theory of SERS, including variants of the plasmonic theory, related theories such as image dipole theories[78,89,90] that, in principle, should also operate at smooth metal surfaces, and non-electromagnetic contributions, often referred to as chemical enhancement.[66,67,91–104] Accordingly, we will focus this review on aspects of SERS in which hotspots and related collective plasmonic effects are implicated, since, in our view, these systems underlie most of the current studies involving SERS and offer us the largest opportunity to produce a review that minimizes overlaps with previous articles. For context, however, we will very briefly summarize the conceptual journey that brought us to this point.

Gersten and Nitzan were among the first to study in detail contributions of the SPR, the lightning rod effect and image dipoles to SERS[78] using a metal ellipsoid or semi-ellipsoid as the model. They (and independently Kerker[82]) also introduced the *ansatz* of computing the SERS enhancement as the fourth power of the local EM field. Schatz and coworkers also considered assemblies of particles.[85,86] Kerker and coworkers calculated the local electric fields contributing to SERS of a molecule adsorbed on a metallic sphere, as a function of such key factors as the size of the particle, dipolar re-radiation effects, the position and orientation of the adsorbed molecules, and polarization of the incident light and its wavelength.[82]

Surface plasmons can also be excited at the surface of smooth films, using a coupling prism. Such a configuration was shown theoretically by Chen and coworkers in 1976 to produce a Raman enhancement of approximately 100 when using the Kretchmann attenuated total reflection (ATR) configuration to measure the Raman and ATR-CARS.[71] Because a surface-plasmon polariton (SPP) is launched in such systems, the ATR-Raman studies contributed to our early understanding of SERS on roughened surfaces. In 1979, Chang and coworkers experimentally compared ATR-Raman from a Ag-film-coated hemi-cylindrical prism with SERS from Ag islands, demonstrating the contribution of surface-plasmon excitation to SERS.[72] Pettinger and coworkers observed the strong dependence of surface Raman intensity on the exciting frequency and on the angle of incidence of the exciting light for roughened Au, Ag and Cu electrodes, providing additional evidence for the surface-plasmon origin of SERS.[74] Finally, Tsang and coworkers reported similar results for SERS on Ag gratings[75] in which a SP polariton could be excited by direct illumination.

Surface plasmons excited by energetic electrons in electron energy loss spectroscopy (EELS) were extensively studied in the late-1950s.[105,106] The Kretchmann[107] and Otto[108] configurations for optically exciting propagating surface plasmons at metal/air interfaces were reported in 1968 and remain actively used in surface spectroscopy, sensing, and other plasmonic applications. In 1970, Kreibig successfully correlated the optical properties of Ag nanoparticles of various sizes with the LSPR spectra of a Ag colloid excited by fast electrons.[109]

Here, we only briefly touch on the chemical enhancement contribution to SERS. Persson,[91] Otto,[66,102] Efrima & Metiu,[92,93] Ueba,[94,95,110] Furtak,[111] Gersten & Schatz,[89] Campion[67] and Lombardi[96] are among those who made significant early contributions to the development of our understanding of chemical enhancement. As summarized in ref. 104, 112 and 113, chemical enhancement embraces several phenomena. Among these are: (1) ground states interactions, such as surface-complexation or chemisorption-induced increases in the adsorbate's Raman polarizability which could contribute even far from resonance;[111,114–117] (2) resonance-like Raman processes, that can also contribute to the Raman polarizability of the free molecule or of the surface complex;[100] (3) new resonances that become possible through photon-driven charge-transfer transitions between electronic states that have primarily a metal character to those that have largely a molecular character and *vice versa*;[98–100,116] (4) enlarged (static or dynamic) polarizabilities due to the solvation of molecules resulting in electron-rich electrochemical interfaces under extremely negative applied voltage.[118,119] Defined in this way, it is clear that the magnitude of chemical enhancement depends critically on the nature of the molecular states and on the specific location or environment of the substrate surface where the adsorbates resides. Research on the chemical contributions to SERS has helped interpret the surface chemical context of the information conveyed in the SERS spectra. Because of the diversity of phenomena that is encompassed by chemical enhancement, a unified theory has not yet been constructed; although, of course, the chemical and electromagnetic contributions to SERS will likely merge into one holistic theory when, at some future time, a fully quantum mechanical theory of SERS is formulated.

In the following section, we cover, very briefly, elements of the rudiments of EM theory of SERS before continuing to key concepts related to 'hotspots' and theories related to EM interactions between illuminated nano-systems. Finally, we discuss and assess some new designs of SERS substrates.

2 Electromagnetic theory of SERS

Electromagnetic SERS enhancement is often discussed as a two-step process: the local field enhancement and the radiation enhancement.[4,5,82,120–123]

Published on 29 Junie 2017. Downloaded by Fail Open on 2025-05-07 9:23:53 vm..

2.1 Theory of Raman of an isolated molecule in free space

The linear Raman intensity of a free molecule depends on the induced dipole $\boldsymbol{p}_{\mathrm{m},0}(\omega_{\mathrm{R}}, \boldsymbol{r}_{\mathrm{m}})$ at the Raman-scattered frequency (ω_{R}). The induced dipole $\boldsymbol{p}_{\mathrm{m},0}(\omega_{\mathrm{R}}, \boldsymbol{r}_{\mathrm{m}})$ at position $\boldsymbol{r}_{\mathrm{m}}$ can be expressed as the inner product of the incident electric field strength $\boldsymbol{E}_0$, and the derived Raman polarizability tensor $\boldsymbol{\alpha}^{\mathrm{I}}_{\mathrm{m}}(\omega_{\mathrm{R}}, \omega_0)$, which reflects the modulation of the local incident photons at frequency ω_0 by the molecular vibration, yielding the inelastic Raman photons at frequency ω_{R}:

$$\boldsymbol{p}_{\mathrm{m},0}(\omega_{\mathrm{R}}, \boldsymbol{r}_{\mathrm{m}}) = \boldsymbol{\alpha}^{\mathrm{I}}_{\mathrm{m}}(\omega_{\mathrm{R}}, \omega_0)\boldsymbol{E}_0(\omega_0, \boldsymbol{r}_{\mathrm{m}}) \qquad (1)$$

The oscillating $\boldsymbol{p}_{\mathrm{m},0}(\omega_{\mathrm{R}},\boldsymbol{r}_{\mathrm{m}})$ in free space or homogeneous medium radiates an EM field into the far field. The measured electric field strength at $\boldsymbol{R}$ where the observer is located is:[124]

$$\boldsymbol{E}_{\mathrm{m},0}(\omega_{\mathrm{R}}, \boldsymbol{R}) = {\omega_{\mathrm{R}}}^2\mu\mu_0\overleftrightarrow{\mathbf{G}}_0(\boldsymbol{R}, \boldsymbol{r}_{\mathrm{m}}) \cdot \boldsymbol{p}_{\mathrm{m},0}(\omega_{\mathrm{R}}, \boldsymbol{r}_{\mathrm{m}}) \qquad (2)$$

where μ and μ_0 are the relative permeability, and permeability in vacuum, and $\overleftrightarrow{\mathbf{G}}_0$ denotes the dyadic Green's function in the homogenous medium:

$$\overleftrightarrow{\mathbf{G}}_0(\boldsymbol{r}, \boldsymbol{r}_{\mathrm{m}}) = \left[\overleftrightarrow{\mathbf{I}} + \frac{1}{k^2}\nabla\nabla\right]\frac{\exp(ik|\boldsymbol{r}-\boldsymbol{r}_{\mathrm{m}}|)}{4\pi|\boldsymbol{r}-\boldsymbol{r}_{\mathrm{m}}|} \qquad (3)$$

The measured Raman power $P_{\mathrm{m},0}$ in the far field over all the solid angles is the radiated power:

$$P_{\mathrm{m},0} = \oiint_{\mathrm{S}} 1/2\mathrm{Re}\left\{\boldsymbol{E}_{\mathrm{m},0}(\omega_{\mathrm{R}}, \boldsymbol{R}) \times \boldsymbol{H}_{\mathrm{m},0}{}^{*}(\omega_{\mathrm{R}}, \boldsymbol{R})\right\} \cdot \boldsymbol{n}\mathrm{d}s \qquad (4)$$

where $\boldsymbol{n}$ is the unit vector normal to the integration surface element ds.

Since $P_{\mathrm{m},0}$ refers to the isolated oscillating dipole $\boldsymbol{p}_{\mathrm{m},0}(\omega_{\mathrm{R}}, \boldsymbol{r}_{\mathrm{m}})$, it can be directly calculated using:[124]

$$\begin{aligned} P_{\mathrm{m},0} &= \frac{1}{2}\omega_{\mathrm{R}}\mathrm{Im}\left[\boldsymbol{p}_{\mathrm{m},0}(\omega_{\mathrm{R}}, \boldsymbol{r}_{\mathrm{m}}) \cdot \boldsymbol{E}_{\mathrm{m},0}(\omega_{\mathrm{R}}, \boldsymbol{r}_{\mathrm{m}})\right] \\ &= \frac{\omega^3|\boldsymbol{p}_{\mathrm{m},0}|^2}{2c^2\varepsilon_0\varepsilon_{\mathrm{m}}}\left[\boldsymbol{n}_{\mathrm{p},0} \cdot \mathrm{Im}\overleftrightarrow{\boldsymbol{G}}_0(\boldsymbol{r}_{\mathrm{m}}, \boldsymbol{r}_{\mathrm{m}}) \cdot \boldsymbol{n}_{\mathrm{p},0}\right] \end{aligned} \qquad (5)$$

where $\boldsymbol{E}_{\mathrm{m},0}(\omega_{\mathrm{R}}, \boldsymbol{r}_{\mathrm{m}})$ is the local field produced by the isolated oscillating dipole $\boldsymbol{p}_{\mathrm{m},0}(\omega_{\mathrm{R}}, \boldsymbol{r}_{\mathrm{m}})$, and $\boldsymbol{n}_{\mathrm{p},0}$ is the unit vector along the direction of the free oscillating dipole moment.

2.2 Local field enhancement in SERS

SERS is primarily a result of the local electric field enhancement, which takes advantage of optical resonance processes, such as those enabled by localized surface-plasmon resonance (LSPR) (Fig. 2a). Such processes can enhance the local electric field strength at the molecule $\boldsymbol{E}_{\mathrm{loc}}(\omega_0, \boldsymbol{r}_{\mathrm{m}})$ as shown in eqn (6).

$$\boldsymbol{E}_{\mathrm{loc}}(\omega_0, \boldsymbol{r}_{\mathrm{m}}) = g_1(\omega_0, \boldsymbol{r}_{\mathrm{m}})\boldsymbol{E}_0(\omega_0) \qquad (6)$$

where $\boldsymbol{E}_{\mathrm{loc}}(\omega_0, \boldsymbol{r}_{\mathrm{m}})$ is the local electric field strength at position $\boldsymbol{r}_{\mathrm{m}}$ where the molecule is located. The enhancement factor of the incident electric field strength is $g_1(\omega_0, \boldsymbol{r}_{\mathrm{m}})$. The enhanced local field, in turn, produces a stronger oscillating dipole $\boldsymbol{p}_{\mathrm{m}}(\omega_{\mathrm{R}}, \boldsymbol{r}_{\mathrm{m}})$ at the Raman scattering frequency ω_{R}:

$$\boldsymbol{p}_{\mathrm{m}}(\omega_{\mathrm{R}}, \boldsymbol{r}_{\mathrm{m}}) = \boldsymbol{\alpha}^{\mathrm{I}}_{\mathrm{m}}(\omega_{\mathrm{R}}, \omega_0)\boldsymbol{E}_{\mathrm{loc}}(\omega_0, \boldsymbol{r}_{\mathrm{m}}) \qquad (7)$$

The resulting power enhancement factor at $\boldsymbol{r}_{\mathrm{m}}$ is:

$$M_{\mathrm{loc}}(\omega_0, \boldsymbol{r}_{\mathrm{m}}) = |g_1|^2 = \left|\frac{\boldsymbol{E}_{\mathrm{loc}}(\omega_0, \boldsymbol{r}_{\mathrm{m}})}{\boldsymbol{E}_0(\omega_0, \boldsymbol{r}_{\mathrm{m}})}\right|^2 \qquad (8)$$

which, as shown in Fig. 4, varies significantly with the incident wavelength, showing resonances associated with the LSPR for the isolated Ag nanosphere and for its dimer. More importantly, the local field enhancement in the gap between the Ag nanospheres in the dimer is much stronger than that at any point on the surface of the isolated Ag nanosphere.

2.3 Radiation enhancement in SERS

The radiation characteristics of an oscillating dipole $\boldsymbol{p}_{\mathrm{m}}(\omega_{\mathrm{R}}, \boldsymbol{r}_{\mathrm{m}})$ are significantly affected by the dielectric properties of its surroundings and their consequential optical resonances processes.[4,5,82,120,122,125] Similarly, the Raman-scattered fields are themselves enhanced in a subsequent process of radiation enhancement, such that the overall SERS enhancement is approximately the product of the incident and Raman enhancement processes.

Expressing the SERS enhancement as a two-step process, although easy to visualize is not strictly correct, leading to conceptual difficulties related to understanding where the power comes from for the second enhancement step. Solving the problem as a coupled electromagnetic problem of a radiating dipole in the presence of a plasmonic nanostructure in the presence of an oscillating electromagnetic field produces the correct result. The total power P_{tot} radiated by the oscillating dipole $\boldsymbol{p}_{\mathrm{m}}(\omega_{\mathrm{R}}, \boldsymbol{r}_{\mathrm{m}})$ in the presence of plasmonic nanostructures is given by:[124]

$$P_{\mathrm{tot}}(\omega_{\mathrm{R}}, \boldsymbol{r}_{\mathrm{m}}) = \frac{1}{2}\omega_{\mathrm{R}}\mathrm{Im}[\boldsymbol{p}_{\mathrm{m}}{}^{*}(\omega_{\mathrm{R}}, \boldsymbol{r}_{\mathrm{m}}) \cdot \boldsymbol{E}_{\mathrm{m}}(\omega_{\mathrm{R}}, \boldsymbol{r}_{\mathrm{m}})] \qquad (9)$$

The local field $\boldsymbol{E}_{\mathrm{m}}(\omega_{\mathrm{R}}, \boldsymbol{r}_{\mathrm{m}})$ produced by the oscillating dipole $\boldsymbol{p}_{\mathrm{m}}(\omega_{\mathrm{R}}, \boldsymbol{r}_{\mathrm{m}})$ in the presence of a plasmonic nanostructure is calculated using Maxwell equations and assuming the oscillating dipole source, $\boldsymbol{p}_{\mathrm{m}}(\omega_{\mathrm{R}}, \boldsymbol{r}_{\mathrm{m}})$.

The total power P_{tot} at the Raman-scattered frequency ω_{R} is dissipated in two ways, some is radiated into the far field, the so-called radiative power P_{Rad}, while some is dissipated as heat in plasmonic nanostructures (the nonradiative power P_{NR}.[4])

$$P_{\mathrm{tot}}(\omega_{\mathrm{R}}, \boldsymbol{r}_{\mathrm{m}}) = P_{\mathrm{Rad}} + P_{\mathrm{NR}} \qquad (10)$$

The Raman radiation field $\boldsymbol{E}_{\mathrm{R}}(\omega_{\mathrm{R}}, \boldsymbol{R})$ at the observer coordinate $\boldsymbol{R}$ in the far field is composed of two parts:

$$\boldsymbol{E}_{\mathrm{R}}(\omega_{\mathrm{R}}, \boldsymbol{R}) = \boldsymbol{E}_{\mathrm{m}}(\omega_{\mathrm{R}}, \boldsymbol{R}) + \boldsymbol{E}_{\mathrm{DR}}(\omega_{\mathrm{R}}, \boldsymbol{R}) \qquad (11)$$

where $\boldsymbol{E}_{\mathrm{m}}(\omega_{\mathrm{R}}, \boldsymbol{R})$ is the field emitted from the molecular oscillating dipole $\boldsymbol{p}_{\mathrm{m}}(\omega_{\mathrm{R}}, \boldsymbol{r}_{\mathrm{m}})$, and $\boldsymbol{E}_{\mathrm{DR}}(\omega_{\mathrm{R}}, \boldsymbol{R})$ is the secondary field scattered from the enhancer, which is excited by $\boldsymbol{p}_{\mathrm{m}}(\omega_{\mathrm{R}}, \boldsymbol{r}_{\mathrm{m}})$ nearby. The secondary field $\boldsymbol{E}_{\mathrm{DR}}(\omega_{\mathrm{R}}, \boldsymbol{R})$ is the dipole re-radiation (DR) field.[122]

The total measured Raman intensity integrated over all the solid angles is:

$$P_{\mathrm{Rad}} = \oiint_{\mathrm{S}} \frac{1}{2}\mathrm{Re}\{\boldsymbol{E}_{\mathrm{R}}(\omega_{\mathrm{R}}, \boldsymbol{R}) \times \boldsymbol{H}_{\mathrm{R}}{}^{*}(\omega_{\mathrm{R}}, \boldsymbol{R})\} \cdot \boldsymbol{n}\mathrm{d}s \qquad (12)$$

Published on 29 Junie 2017. Downloaded by Fail Open on 2025-05-07 9:23:53 vm..

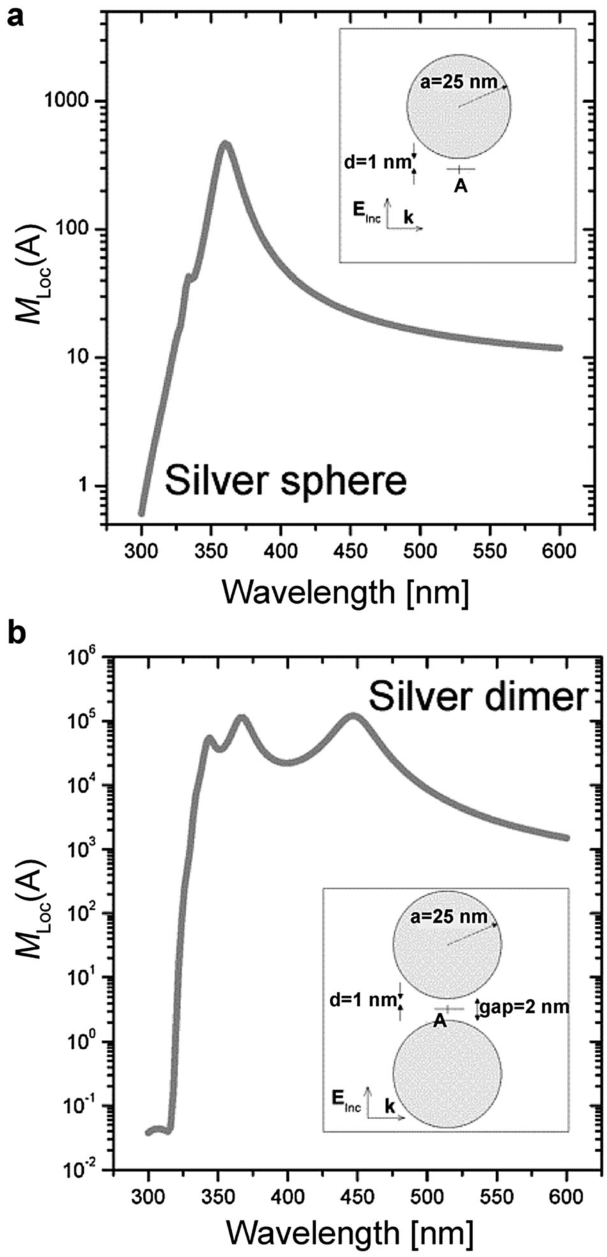

Fig. 4 Example of a modification of the incident local electromagnetic field intensity, $|g_1|^2$, at point *A*, at a distance d = 1 nm (shown in the insets) from the surface of an isolated Ag nanosphere (a) and from the surface of its dimer (b). Image adapted from ref. 4 with permission. Copyright (2009) Elsevier, Amsterdam.

and the nonradiative power can be calculated by volume integration of the Joule heat dissipated in the plasmonic structures V with the local conductivity σ:

$$P_{\mathrm{NR}} = \iiint \frac{1}{2}\mathrm{Re}\{\sigma \boldsymbol{E}(\omega_{\mathrm{R}}, \boldsymbol{r}) \cdot \boldsymbol{E}^{*}(\omega_{\mathrm{R}}, \boldsymbol{r})\}\mathrm{d}v \tag{13}$$

Fig. 5 shows that the power radiated by the coupled dipole–Ag-nanosphere or dipole–Ag-dimer system into the far field can be remarkably enhanced in a certain wavelength range when the direction of the dipole is perpendicular to the surface.

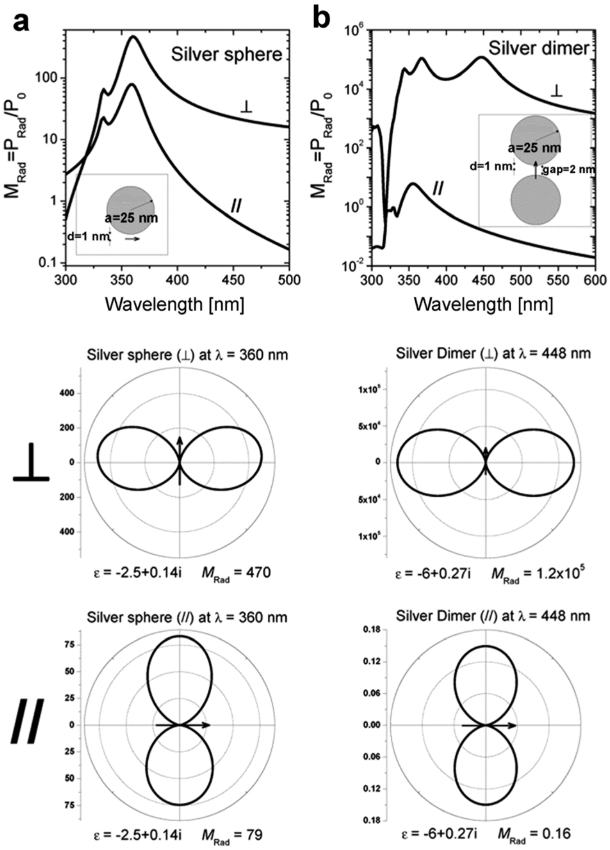

Fig. 5 The extraordinary role of SERS hotspots. Modification of the radiation power ratio calculated from P_{Rad}/P_0 at a distance d = 1 nm at point *A* (shown in the insets) from the surface of an isolated Ag nanosphere (a) and from the surface of its dimer (b). Image adapted from ref. 4 with permission. Copyright (2009) Elsevier, Amsterdam.

The radiation enhancement depends critically on the orientation of the oscillating dipole. Normally, dipoles perpendicular to the surface result in a greater radiation enhancement.[4]

Considering eqn (9), (10) and (13), the power of the total Raman-scattered radiation, P_{Rad}, over all the solid angles, is given by:

$$\begin{aligned} P_{\mathrm{Rad}} &= \frac{1}{2}\omega_{\mathrm{R}}\mathrm{Im}[\boldsymbol{p}_{\mathrm{m}}{}^{*}(\omega_{\mathrm{R}}, \boldsymbol{r}_{\mathrm{m}}) \cdot \boldsymbol{E}_{\mathrm{m}}(\omega_{\mathrm{R}}, \boldsymbol{r}_{\mathrm{m}})] \\ &\quad - \frac{1}{2}\iiint \mathrm{Re}\{\sigma \boldsymbol{E}(\omega_{\mathrm{R}}, \boldsymbol{r}) \cdot \boldsymbol{E}^{*}(\omega_{\mathrm{R}}, \boldsymbol{r})\}\mathrm{d}v \end{aligned} \tag{14}$$

In the absence of a nearby plasmonic nanostructure, the radiant power from an isolated oscillating dipole $\boldsymbol{p}_{\mathrm{m}}(\omega_{\mathrm{R}}, \boldsymbol{r}_{\mathrm{m}})$ would be given by the surface integral of the Poynting vector in the far field, or equivalently by:

$$\begin{aligned} P_0 &= \frac{1}{2}\omega_{\mathrm{R}}\mathrm{Im}\left[\boldsymbol{p}_{\mathrm{m}}{}^{*}(\omega_{\mathrm{R}}, \boldsymbol{r}_{\mathrm{m}}) \cdot \boldsymbol{E}_{\mathrm{m}}{}'(\omega_{\mathrm{R}}, \boldsymbol{r}_{\mathrm{m}})\right] \\ &= \frac{\omega^{3}|\boldsymbol{p}_{\mathrm{m}}|^{2}}{2c^{2}\varepsilon_{0}\varepsilon_{\mathrm{m}}}\left[\boldsymbol{n}_{\mathrm{p}} \cdot \mathrm{Im}\overleftrightarrow{\mathbf{G}}_{0}(\boldsymbol{r}_{\mathrm{m}}, \boldsymbol{r}_{\mathrm{m}}) \cdot \boldsymbol{n}_{\mathrm{p}}\right] \end{aligned} \tag{15}$$

where $\boldsymbol{E}_{\mathrm{m}}{}'(\omega_{\mathrm{R}}, \boldsymbol{r}_{\mathrm{m}})$ is the virtual local field at $\boldsymbol{r}_{\mathrm{m}}$ produced by the isolated oscillating dipole $\boldsymbol{p}_{\mathrm{m}}(\omega_{\mathrm{R}}, \boldsymbol{r}_{\mathrm{m}})$ assuming there is no

Published on 29 Junie 2017. Downloaded by Fail Open on 2025-05-07 9:23:53 vm..

plasmonic nanostructure nearby and $\boldsymbol{n}_p$ is the unit vector in the direction of the oscillating dipole moment $\boldsymbol{p}_m(\omega_R, \boldsymbol{r}_m)$.

The radiation enhancement M_{Rad} can then be exactly calculated by:

$$M_{Rad}(\omega_0,\boldsymbol{r}_m)=\frac{P_{Rad}}{P_0} \tag{16}$$

M_{Rad} is usually approximated using the optical reciprocity theorem:

$$M_{Rad}(\omega_0,\boldsymbol{r}_m)\approx\left|\frac{\boldsymbol{E}_{loc}(\omega_R,\boldsymbol{r}_m)}{\boldsymbol{E}_0(\omega_R,\boldsymbol{r}_m)}\right|^2 \tag{17}$$

where $\boldsymbol{E}_{loc}(\omega_R,\boldsymbol{r}_m)$ is the local fields produced by a plane-wave light field $\boldsymbol{E}_0(\omega_R, \boldsymbol{r}_m)$ at the frequency ω_R, which are discussed in greater detail in Section 3.6 and in the ref. 4 and 122.

The SERS enhancement factor at $\boldsymbol{r}_m$ is given by:

$$\mathrm{EF}(\omega_0,\omega_R,\boldsymbol{r}_m)=\frac{P_{Rad}}{P_{m,0}}=\frac{P_0}{P_{m,0}}\cdot\frac{P_{Rad}}{P_0}=\frac{P_0}{P_{m,0}}M_{Rad}(\omega_0,\boldsymbol{r}_m) \tag{18}$$

where M_{Rad} is the radiation enhancement of SERS and

$$\frac{P_0}{P_{m,0}}=\frac{\dfrac{\omega^3|\boldsymbol{p}_m|^2}{2c^2\varepsilon_0\varepsilon_m}\left[\boldsymbol{n}_p\cdot\mathrm{Im}\overset{\leftrightarrow}{\mathbf{G}}_0(\boldsymbol{r}_m,\boldsymbol{r}_m)\cdot\boldsymbol{n}_p\right]}{\dfrac{\omega^3|\boldsymbol{p}_{m,0}|^2}{2c^2\varepsilon_0\varepsilon_m}\left[\boldsymbol{n}_{p,0}\cdot\mathrm{Im}\overset{\leftrightarrow}{\mathbf{G}}_0(\boldsymbol{r}_m,\boldsymbol{r}_m)\cdot\boldsymbol{n}_{p,0}\right]} \tag{19}$$

$$\approx\left|\frac{\boldsymbol{E}_{loc}(\omega_0,\boldsymbol{r}_m)}{\boldsymbol{E}_0(\omega_0,\boldsymbol{r}_m)}\right|^2=M_{loc}$$

The SERS enhancement factor at $\boldsymbol{r}_m$ can be approximated by:

$$\mathrm{EF}(\omega_0, \omega_R, \boldsymbol{r}_m) = M_{loc}(\omega_0, \boldsymbol{r}_m)M_{Rad}(\omega_R, \boldsymbol{r}_m) \tag{20}$$

by ignoring the effects that the direction of the oscillating dipole $\boldsymbol{n}_p$ in the dipole-nanostructure system is different from the direction of $\boldsymbol{n}_{p,0}$ in free space due to the possible change of the polarization of the local field $\boldsymbol{E}_{loc}(\omega_0, \boldsymbol{r}_m)$ in contrast to that of the incident lasers $\boldsymbol{E}_0(\omega_0, \boldsymbol{r}_m)$.[4,126]

When the frequency of the Raman-scattered light is very close to that of the incident light eqn (20) simplifies to:

$$\mathrm{EF}(\omega_0,\omega_R,\boldsymbol{r}_m)\approx\left|\frac{\boldsymbol{E}_{loc}(\omega_0,\boldsymbol{r}_m)}{\boldsymbol{E}_0(\omega_0,\boldsymbol{r}_m)}\right|^2\cdot\left|\frac{\boldsymbol{E}_{loc}(\omega_R,\boldsymbol{r}_m)}{\boldsymbol{E}_0(\omega_R,\boldsymbol{r}_m)}\right|^2\approx\left|\frac{\boldsymbol{E}_{loc}(\omega_0,\boldsymbol{r}_m)}{\boldsymbol{E}_0(\omega_0,\boldsymbol{r}_m)}\right|^4. \tag{21}$$

Eqn (21) is the well-known $|\boldsymbol{E}|^4$-approximation for the SERS enhancement factor, which is discussed in detail in Section 3.6.

The second enhancement could be considered to be the modified spontaneous emission due to the local excitation of the LSP by the induced dipole.

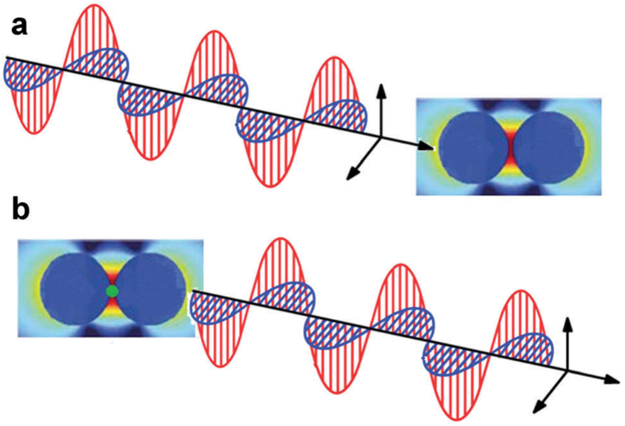

Fig. 6 Schematic of the two-step SERS enhancement mechanism: (a) local field enhancement, (b) radiation enhancement.

In summary, in the first-step enhancement, an optical antenna collects light from an effectively larger volume (as the 'antenna volume') and concentrates much of it in a 'hot-spot'; in the second enhancement step, the local electric field due to emission by the molecules resident in the hotspot then drives the entire antenna to radiate resonantly (Fig. 6) (Please also see the simple formula for estimating the SERS EF presented in Section 3.2.2). Viewed in this way, SERS is light scattered by the plasmonic nanostructure modulated at the frequency of the molecule's vibration. Simplistically this accounts for the large enhancement.

It should be noted that the enhancement factors defined in eqn (17) and (21) are position-dependent quantities. The surface-averaged SERS enhancement factor defined by averaging SERS $\mathrm{EF}(\omega_0, \omega_R, \boldsymbol{r}_m)$ over the surface of the plasmonic nanostructures is also often reported.

2.4 Practical numerical simulations of the local-field and far-field properties of plasmonic nanoparticles, and their SERS performance

Classical electrodynamic simulations have greatly helped us quantitatively understand SERS and the materials, nano-architectural, and excitation and collection optics variables responsible for high enhancements. These insights have guided the design of SERS substrates with better performance. Several numerical methods are commonly used to help interpret a wide range of nano-optical and spectroscopic experiments, and to determine the optical properties of particles or particle–substrate hybrid structures. Popular numerical methods include the discrete dipole approximation (DDA), the finite difference time domain (FDTD) method, the finite element method (FEM), volume integral methods, *etc.*[127] The typical geometry of nanoparticles, such as a nanosphere dimer, embedded in the surrounding media, such as water, is defined in Fig. 7.

Two approaches are used to compute the extinction spectra. The first is to define ports through which the electromagnetic energy enters or exits the system. After solving the full-field Maxwell equation, one calculates the transmission coefficient, T, of the structure using an $\mathbf{S}$ matrix calculation. The extinction at this wavelength is computed from $(1 - T)$, and the spectrum determined by repeating the process at various wavelengths.

If the functional form of the background field $\boldsymbol{E}_{bg}$ in the absence of the nanoparticle is known, this can be included in the scattered field calculation, otherwise one assumes $\boldsymbol{E}_{bg}$ to be a plane wave, Gaussian beam or the field of a dipole source,

Published on 29 Junie 2017. Downloaded by Fail Open on 2025-05-07 9:23:53 vm..

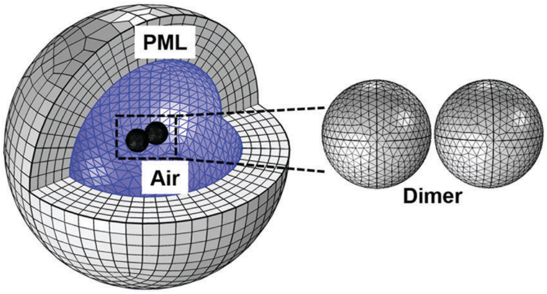

Fig. 7 Model of the approach used to compute the field in the vicinity of a nanoparticle dimer. The dimer is positioned at the origin. The zoom-in view of the meshed dimer is shown on the right. The surrounding medium is assumed to be an aqueous solution and the outside layer is PML. The blue boundary denotes the outside boundary of the surrounding medium, which is also the boundary for the far-field calculation.

among other options. The scattering power P_{sca} is defined by surface integral of the relative Poynting vector over the appropriate closed surfaces,[128]

$$P_{\text{sca}} = P_{\text{rel}} = \oiint_S \frac{1}{2}\text{Re}\{\boldsymbol{E}_{\text{rel}} \times \boldsymbol{H}_{\text{rel}}{}^*\} \cdot \boldsymbol{n}\text{d}s \qquad (22)$$

where $\boldsymbol{E}_{\text{rel}} = \boldsymbol{E} - \boldsymbol{E}_{\text{bg}}$ and $\boldsymbol{H}_{\text{rel}} = \boldsymbol{H} - \boldsymbol{H}_{\text{bg}}$ are the electric field and magnetic field values relative to the background field, respectively. The $\boldsymbol{n}$ is the outward normal vector over the closed surface for detection. The absorption power P_{abs} can be calculated by summing the volume integrals of the Joule heat dissipated in all the lossy units,

$$P_{\text{abs}} = \sum_k \iiint_{\Omega_k} \frac{1}{2}\text{Re}\{\sigma_k \boldsymbol{E} \cdot \boldsymbol{E}^*\}\text{d}v \qquad (23)$$

where $\boldsymbol{E}$ is the total electric field including the background and scattering part in the k^{th} unit Ω_k and σ_k is the conductivity of the material in the k^{th} unit.

The extinction power P_{ext} is:

$$P_{\text{ext}} = P_{\text{sca}} + P_{\text{abs}} \qquad (24)$$

P_{ext} can also be calculated by the surface integral:

$$P_{\text{ext}} = -\oiint_S \frac{1}{2}\text{Re}\{\boldsymbol{E}_{\text{rel}} \times \boldsymbol{H}^* + \boldsymbol{E} \times \boldsymbol{H}_{\text{rel}}{}^*\} \cdot \boldsymbol{n}\text{d}s \qquad (25)$$

The full extinction spectrum is obtained by repeating the calculation at various wavelengths.

The plasmon modes can be analyzed in terms of the local field distribution and in particular, by the (phase-dependent) surface charge distribution, which can be calculated using the integral form of Gauss' law:

$$Q(\boldsymbol{r}) = \varepsilon_{\text{m}}\varepsilon_0 \oiint_S (\boldsymbol{E} \cdot \boldsymbol{n})\text{d}s = \varepsilon_{\text{m}}\varepsilon_0 \oiint_S (n_x \cdot E_x + n_y \cdot E_y + n_z \cdot E_z)\text{d}s \qquad (26)$$

where ε_0 is the permittivity of the vacuum, ε_{m} is the relative permittivity of the surrounding medium, $\boldsymbol{n} = (n_x, n_y, n_z)$ is the outward normal vector of the metal surface and $\boldsymbol{E} = (E_x, E_y, E_z)$ is the local electric field strength at the vicinity of the surface.

The surface charge at each point, $\text{d}q(x_0, y_0, z_0)$, on the surface is:

$$\text{d}q(x_0, y_0, z_0) = \varepsilon_{\text{m}}\varepsilon_0(\boldsymbol{n}_0\cdot\text{d}\boldsymbol{E}) = \varepsilon_{\text{m}}\varepsilon_0(n_{0x}\cdot\text{d}E_x + n_{0y}\cdot\text{d}E_y + n_{0z}\cdot\text{d}E_z) \qquad (27)$$

where ε_0 is the permittivity of the vacuum, ε_{m} is the relative permittivity of the surrounding medium, $\boldsymbol{n}_0 = (n_{0x}, n_{0y}, n_{0z})$ is the outward normal vector of point (x_0, y_0, z_0) on the metal surface and $\text{d}\boldsymbol{E} = (\text{d}E_x, \text{d}E_y, \text{d}E_z)$ is the difference in the local electric field strength going across the surface of point (x_0, y_0, z_0). In COMSOL, the '*up*' and '*down*' operators were used to calculate $\text{d}\boldsymbol{E}$ as:

$$\text{d}\boldsymbol{E}(x_0, y_0, z_0) = \text{up}(\boldsymbol{E}(x_0, y_0, z_0)) - \text{down}(\boldsymbol{E}(x_0, y_0, z_0)) \qquad (28)$$

Furthermore, the manner used to estimate the average SERS enhancement factor (EF) according to the $|\boldsymbol{E}|^4$-approximation is important. We should pre-define the to-be-averaged surface S or volume V. The average SERS EF of the surface was obtained using the surface integral:

$$\text{EF}_{\text{ave},S} = \frac{\iint \left|\dfrac{\boldsymbol{E}_{\text{loc}}}{\boldsymbol{E}_0}\right|^4 \cdot \text{d}s}{\iint 1 \cdot \text{d}s} \qquad (29)$$

While, the average SERS EF of the volume can be obtained by applying the volume integral:

$$\text{EF}_{\text{ave},V} = \frac{\iiint \left|\dfrac{\boldsymbol{E}_{\text{loc}}}{\boldsymbol{E}_0}\right|^4 \cdot \text{d}v}{\iiint 1 \cdot \text{d}v} \qquad (30)$$

In order to calculate the radiation enhancement, the molecular electric point dipole, $\boldsymbol{p}_{\text{m}}(\omega_{\text{R}}, \boldsymbol{r}_{\text{m}})$ is created by a current filament carrying a uniform current $\boldsymbol{I}$ oscillating with frequency ω_{R}, and with a small length, d. The radiation field $\boldsymbol{E}_{\text{R}}(\omega_{\text{R}}, \boldsymbol{R})$ is calculated by solving the pertinent Maxwell equations.

The total power P_{tot} extracted from the oscillating dipole $\boldsymbol{p}_{\text{m}}(\omega_{\text{R}}, \boldsymbol{r}_{\text{m}})$ is obtained from eqn (9). P_{Rad} over each solid angle is calculated using the surface integral, eqn (12), over a closed surface enclosing the dipole, yielding the radiation power in the far field at a specified angle. While the direction-dependent Raman signals $P_{\text{Rad}}(\Omega)$ are calculated using the following surface integral over the selected surface element Γ.

$$P_{\text{Rad}}(\Omega) = \iint_{\Gamma} \frac{1}{2}\text{Re}\{\boldsymbol{E}_{\text{R}}(\omega_{\text{R}}, \boldsymbol{R}) \times \boldsymbol{H}_{\text{R}}{}^*(\omega_{\text{R}}, \boldsymbol{R})\} \cdot \boldsymbol{n}\text{d}s \qquad (31)$$

3 SERS hotspots

The EM field near a plasmonic nanostructured material is, in general, non-uniformly distributed, and often highly localized in spatially narrow regions ('SERS hotspots'), such as, nanotips, interparticle nanogaps or particle–substrate nanogaps.[5,83,84,88,129–140] Molecules resident in SERS hotspots (1–5 nm) often dominate the measured SERS spectrum. For example, for a molecular monolayer uniformly covering the surface of a Ag nanosphere dimer with a gap of 2 nm, and assuming the SERS intensity can be approximated using the fourth power of a local EM field as in eqn (21), the

Published on 29 Junie 2017. Downloaded by Fail Open on 2025-05-07 9:23:53 vm..

molecules resident in the hotspot account for less than 1% of the total area, but contribute for over 50% of the total SERS signal.[141]

3.1 First-generation hotspots

First-generation hotspots have been generated in assemblies of single nano-objects, such as nanospheres or nanorods suspended in a homogeneous medium. These hotspots exhibit moderate SERS activity. However, assemblies of rationally designed single nanoparticles with nanoshells, sharp corners, ridges, grooves, tips and/or with intra-particle gaps, such as Au and Ag nanocubes, nanobars, nanostars, triangular nanoprisms, cauliflower-like and other multi-branched nanostructures, and mesocages exhibit much more intense SERS activity.[20,42,142–145] Other systems, such as a TERS tip and SERS substrates composed of, for example, nanocubes and cauliflower-like nanostructures with sharp corner, edges, *etc.* that do not show well-defined LSPR resonances at commonly used laser wavelengths, could nevertheless show respectable SERS activity, implying that the local field in their vicinities were enhanced. Matrix-isolated metal clusters are special nanostructures supporting first-generation hotspots. Moskovits and coworkers reported that the Raman enhancement per monoxide (CO) ligand in $Ag_{50}CO_{40}$ could reach up to 1830 to 1350 for laser excitation ranging from 457.9 to 514.5 nm, and in principle could reach up to 12 000 at the plasmon resonant wavelength at 370 nm.[146]

3.2 Second-generation hotspots

Achieving intense SERS signals largely hinges on devising substrates that possess efficient SERS 'hotspots' and placing the desired analyte in them. Originally that meant creating nanoparticle aggregates, while more recently, this entails appropriately nano-engineering substrates. The SERS enhancement at a properly engineered hotspot can be as great as 10^{11}. However, when averaged over the substrate as a whole, the average enhancement will have contributions both from molecules adsorbed at the hotspot and the many more, less-enhancing sites. This will rarely exceed 10^7 or 10^8.

Second-generation SERS hotspots arise from coupled nanostructures with controllable inter-particle nanogaps. Typical examples are the Au or Ag NP dimers that were used for single-molecule SERS[23,147–150] (Fig. 8a and b) and core@shell nanoparticle dimers[15,28,142] (Fig. 8c and d), nanoparticle aggregates or oligomers[3,147,151–153] (Fig. 8e), nanoparticle arrays such as core–satellite structures,[154,155] nanoparticle assemblies with controllable nanogaps[156–158] (Fig. 8f) or inter-unit nanogaps in nanopatterned surfaces (Fig. 8g and h). Second-generation hotspots exhibit excellent SERS activity. Typically, the average SERS intensities from coupled plasmonic nanostructures are four orders of magnitude greater than those from single nanostructures.[135,159]

3.2.1 Hotpots in the gap regions of a dimer. The local EM field in the gap between Au or Ag nanoparticle dimers and oligomers with inter-particle nanogaps is very intense due to the strong EM coupling. The extinction spectra of the Au or Ag dimer and the SERS EFs in the nanogap of Ag or Au oligomers depend critically on the gap size. For example, reducing the gap size in a Au nanosphere dimer from 10 to 2 nm, increases the SERS EF from 10^5 to 10^9 (Fig. 9).

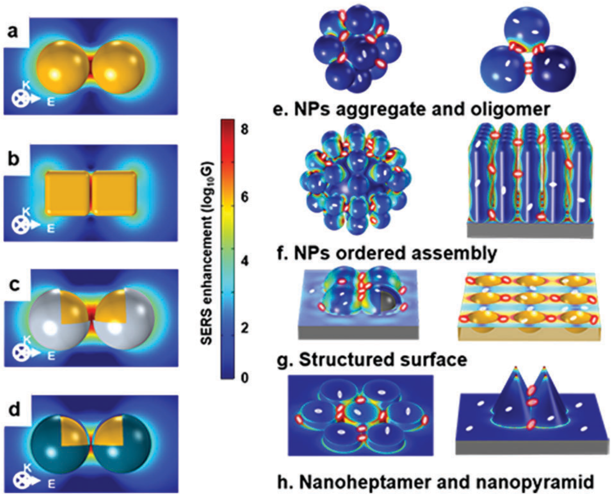

Fig. 8 Second-generation hotspots generated in coupled nanoparticles. (a–d) FEM simulations of the SERS-enhancement distribution in typical Au nanoparticles. (a) A nanosphere dimer (60 nm in diameter, 2 nm gap size in water; excitation line at 585 nm; an average SERS EF over the whole outer surface of a NP, denoted $\langle G_{NP} \rangle$, of 1.47 × 10^6, and a SERS maximum EF at the outer surface, denoted G_{NP}^{max}, of 4.11 × 10^9). (b) Nanocube dimer (60 nm in side length; 2 nm gap size; in water; excitation line at 725 nm; $\langle G_{NP} \rangle$ = 2.41 × 10^5 and G_{NP}^{max} = 1.24 × 10^8). (c) A Au@SiO_2 core@shell nanosphere dimer (60 nm in diameter of core; 2 nm in shell thickness; in water; excitation line at 600 nm; $\langle G_{NP} \rangle$ = 1.01 × 10^5 and G_{NP}^{max} = 1.21 × 10^7). (d) A Au@Pt core@shell nanosphere dimer (60 nm in diameter of core; 2 nm in shell thickness; in water; excitation line at 645 nm; $\langle G_{NP} \rangle$ = 2.35 × 10^5 and G_{NP}^{max} = 8.74 × 10^7). (e–h) Schematic illustrations of typical coupled nanostructures as second-type SERS hotspots for trace-molecule detection. (e) Ag or Au NP aggregates with multiple hotspots (left) and their oligomer (right). (f) A core–satellite nanostructured assembly with small Au NPs assembled on a larger Au NP (left) or a vertical self-assembly of Au nanorods on supporters (right). (g) Nanostructured surfaces with nanobumps (left) or nanovoid arrays (right) by the deposition of Ag on pre-assembled SiO_2 or polystyrene spheres, and (h) an individual nanoheptamer (left) and a nanocone quadrumer (right). In (e–h), the adsorbed target molecules are depicted as white points. Images (a, b) and (e, f) adapted from ref. 5 with permission. Copyright (2016) Nature Publishing group; image (c and d) adapted from ref. 28 with permission. Copyright (2017) American Chemical Society.

Schatz and coworkers studied the gap-size (g) dependence of the field enhancement factor $|\boldsymbol{E}_{loc}|^2/|\boldsymbol{E}_0|^2$ using both FEM calculations and a semi-analytical model, and showed that for small gaps down to 1 nm, the local field enhancement confined in the gap arises from the waveguide mode, and depends on the local field strength as $|\boldsymbol{E}_{loc}|^2/|\boldsymbol{E}_0|^2 \sim 1/g^p$, with $p \approx 1.2$–1.5, rather than as $1/g^2$, as the simple antenna theory predicts.[160]

3.2.2 Model for estimation of the SERS enhancement factor and its indications. SERS enhancement in the hotspots could also be estimated by an order of magnitude calculation that establishes some upper bounds for the SERS EF.

The model. Assuming the total radiative power (incident, absorbed, emitted and scattered) for a single molecule sitting in the gap of a nanosphere dimer is a conserved quantity; accordingly:

$$V_A \rho_0 = (V_A - V_{HS})\rho_A + V_{HS}\rho_{HS} \tag{32}$$

Published on 29 Junie 2017. Downloaded by Fail Open on 2025-05-07 9:23:53 vm..

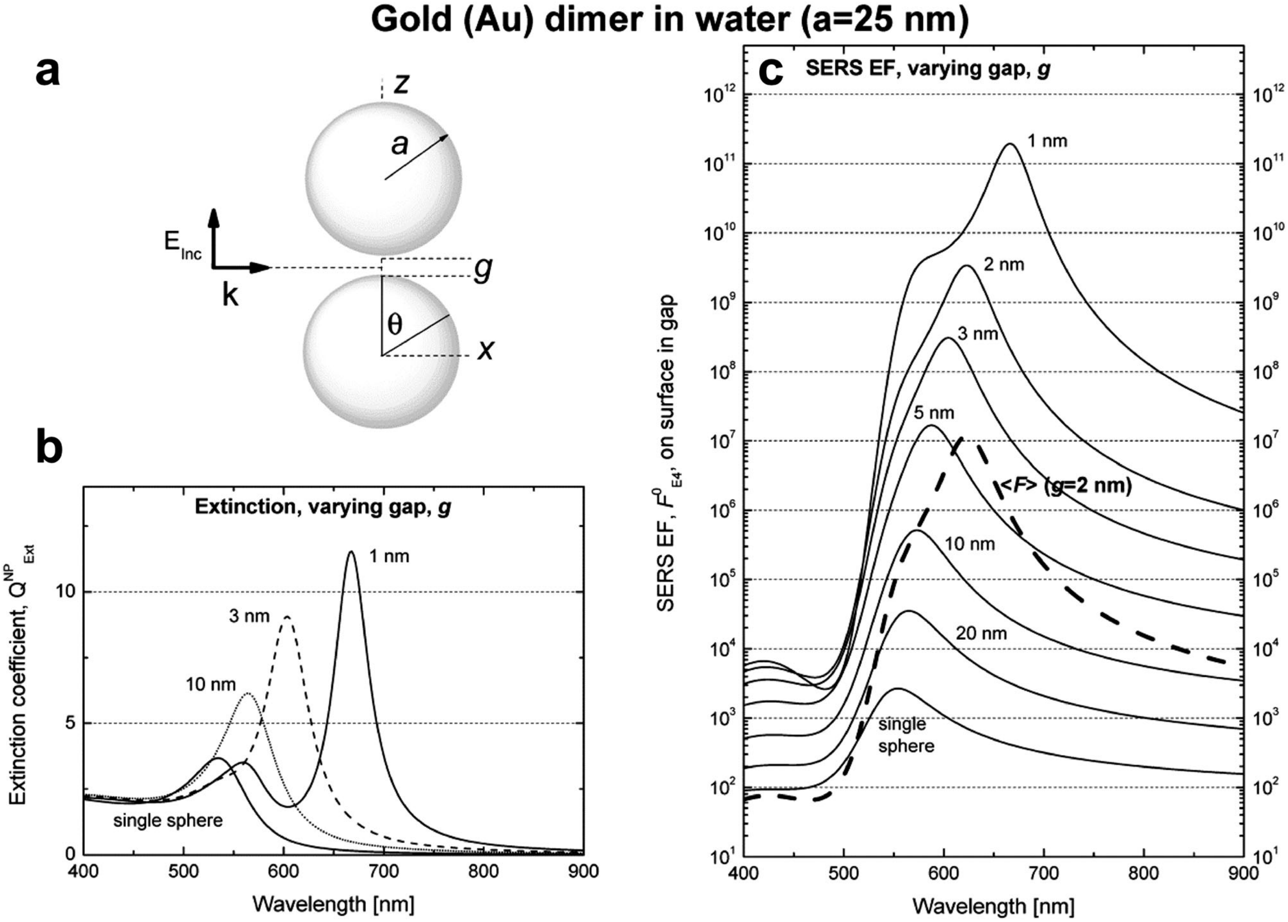

Fig. 9 (a) Configuration of a dimer (along *z*) formed by two Au nanospheres of radii *a* and separated by a gap *g*. The incident plane wave is polarized along *z* (the axis of the dimer) with the wavevector *k* along *x*. (b) The simulated extinction coefficient spectra for varying gap sizes. (c) The simulated SERS EF (according to $|\boldsymbol{E}|^4$-approximation) at the surface of one of the spheres in the gap along the *z* direction. Also shown (thick dashed line) is the average SERS EF for g = 2 nm. Image adapted from ref. 4 with permission. Copyright (2009) Elsevier, Amsterdam.

where V_A and V_HS are, respectively, the effective interaction volume of incident light with the nanoantenna and the volume of hotspots region (Fig. 10), while ρ_A, ρ_HS and ρ_0 are, respectively, the radiation densities flowing per unit time through V_A and V_HS at the steady state, and through V_A initially. In the above model, one assumes that the radiation will be redistributed from the initial almost uniform value, ρ_0, outside the dimer to its steady state value with a highly localized photon density in the nanogap.

By re-arranging eqn (32), and assuming that $\rho_\mathrm{HS} \gg \rho_0 \gg \rho_\mathrm{A}$, we get:

$$\frac{V_\mathrm{A}}{V_\mathrm{HS}} = \frac{\rho_\mathrm{HS} - \rho_\mathrm{A}}{\rho_0 - \rho_\mathrm{A}} \approx \frac{\rho_\mathrm{HS}}{\rho_0} \tag{33}$$

Since the SERS EF is approximately proportional to the fourth power of the local field enhancement, the EF computed in this way is approximately:

$$\mathrm{EF} \cong \left(\frac{\rho_\mathrm{HS}}{\rho_0}\right)^2 \approx \left(\frac{V_\mathrm{A}}{V_\mathrm{HS}}\right)^2 \tag{34}$$

For $V_\mathrm{A} \sim 200 \times 100 \times 100$ nm^3, and $V_\mathrm{HS} \sim 10$ nm^3, the estimated SERS EF is $\sim 4 \times 10^{10}$. This is the maximum EF for a molecule in a hotspot, and does not take into account the number of molecules 'sacrificed' at the non-enhancing parts of the nanostructure.

The dimensions of V_A and V_HS were chosen as follows. We assumed a wavelength of 1 μm to conform with the recent penchant towards near IR (the upper bounds are even lower for shorter wavelengths), and took account of the fact that, while the larger the antenna, the more radiation it can harvest (being careful not to go beyond the region of resonance with the LSP), the dipolar radiation required for the 'second step' in SERS enhancement makes use of a progressively smaller fraction of the concentrated energy as the antenna's dimensions become of the order of or larger than the wavelength.

Let's now estimate the reduction in the average value of EF when one averages over the full surface of the nanostructure. In other words, one assumes that the surfaces of the antenna region and of the hotspot are saturated with molecules. If so:

$$N_\mathrm{A} \propto V_\mathrm{A}^{\frac{2}{3}} \text{ and } N_\mathrm{HS} \propto V_\mathrm{HS}^{\frac{2}{3}} \tag{35}$$

where N_A and N_HS are the number of molecules located in the antenna region and hotspots region, respectively.

Published on 29 Junie 2017. Downloaded by Fail Open on 2025-05-07 9:23:53 vm..

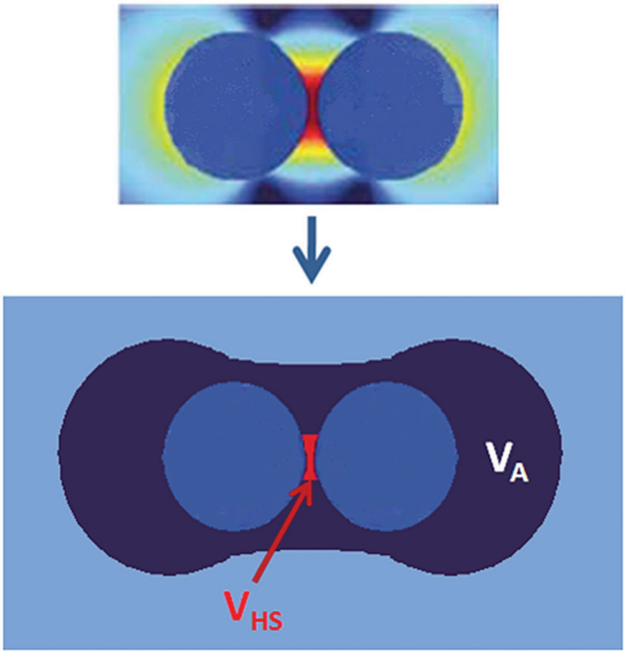

Fig. 10 EM field distribution of a Ag nanosphere dimer and the volume. The area with EM field enhancement is denoted as V_A, and the volume of hotspot at the nanogap is denoted as V_{HS}.

For this case, the averaged EF (AEF) over the nanostructures is approximately given by:

$$\mathrm{AEF} = \frac{N_{\mathrm{HS}}}{N_{\mathrm{A}}}\left(\frac{V_{\mathrm{A}}}{V_{\mathrm{HS}}}\right)^2 = \left(\frac{V_{\mathrm{HS}}}{V_{\mathrm{A}}}\right)^{2/3}\left(\frac{V_{\mathrm{A}}}{V_{\mathrm{HS}}}\right)^2 = \left(\frac{V_{\mathrm{A}}}{V_{\mathrm{HS}}}\right)^{4/3} \quad (36)$$

which yields a value for the SERS AEF of $\sim 1.7 \times 10^7$.

The aforementioned model is highly simplistic; nevertheless, a few insights might be extracted from the expression for the SERS EF eqn (34) and AEF eqn (36). Since SERS EF and AEF depend sensitively on V_A/V_{HS}, one useful strategy for optimizing a plasmonic antenna for SERS is to simply increase the antenna volume. But there is an upper limit, whereby the antenna dimensions cannot be larger than the wavelength.

Optimizing the antenna shape for a much larger effective interaction antenna volume. The field enhancement capability of a dimer of interacting nanoparticles depends critically on the shape of the nanoparticles. For example, the receiving and transmitting efficiencies of dipolar antennas based on nanobars or nanorods are usually much larger than those for a bowtie antenna[161] (Fig. 11) and can be organised in the following order: nanorod dipolar antenna > nanocube dipolar antenna > bowtie antenna.

Designing hierarchical plasmonic structures with multiscale coupling. Another strategy for improving the enhancing capability of such coupled nanostructures is to make a large antenna with a strong optical response that is coupled with a dimer. The large antenna could efficiently collect the incident light from the far-field and concentrate it into the subwavelength region occupied by the dimer. Although superficially this amplification process seems straightforward, in fact, it contains an inconsistency. This is because, reciprocally, the Raman light scattered by a small dimer can couple to the larger antenna, which then redirects the light into a much larger receiving volume. This can potentially be ameliorated by cascading antennas. Because a smaller antenna is able to further concentrate the optical field from dimensions of the order of the subwavelength to a deep-subwavelength volume, such as a nanogap, this field concentration process can be cascaded hierarchically so that ultimately one can concentrate the EM energy initially in a (far field) volume several wavelengths in diameter up to near fields in the hotspot, that are several nanometres in diameter and so on. Such hierarchical field concentrating structures might be the basis of a new generation of PERS-active substrates.

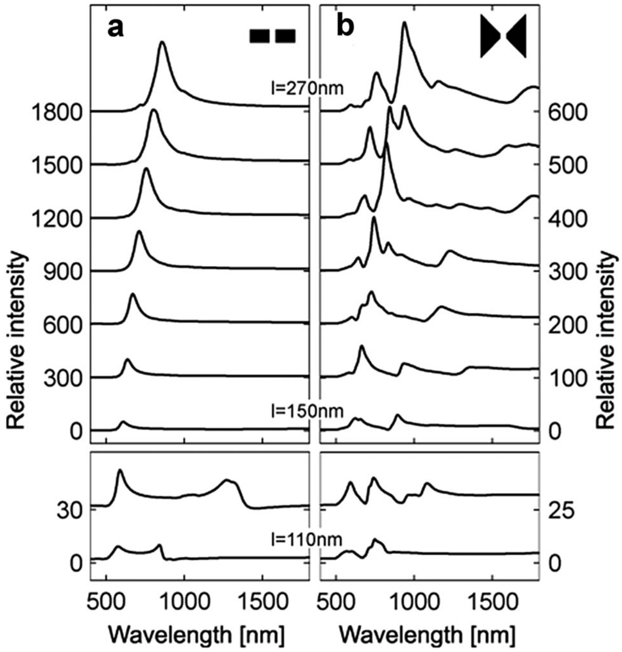

Fig. 11 Relative intensity enhancement in the gap as a function of the antenna length l between l = 110 nm and l = 270 nm in 20 nm increments. (a) Dipole and (b) bowtie geometry (a = 90°). The antenna gap is kept constant (g = 30 nm). Image adapted from ref. 161 with permission. Copyright (2008) Optical Society of America.

Gordon and coworkers reported an example on this concept (Fig. 12). The authors built a large optical antenna based on a resonant ring-reflector, which consisted of a gold film with a circular hole coupled to a Au planar film.[162,163] The two Au films were separated by a dielectric spacer. The larger optical antenna pre-concentrates the emitted beam to the circular hole where the nanoparticle dimer is located. This design proved quite efficient since almost all the incident beam power was focused into a circular area approximately the size of the numerical aperture of the microscope. Furthermore, the emission was directed out of the plane, so as to direct the enhanced Raman appropriately to enable it to be collected using a conventional Raman microscope. Bestowing such helpful directionality on the SERS emissions can also be achieved with the Yagi-Uda or the travelling wave antenna designs.

Published on 29 Junie 2017. Downloaded by Fail Open on 2025-05-07 9:23:53 vm..

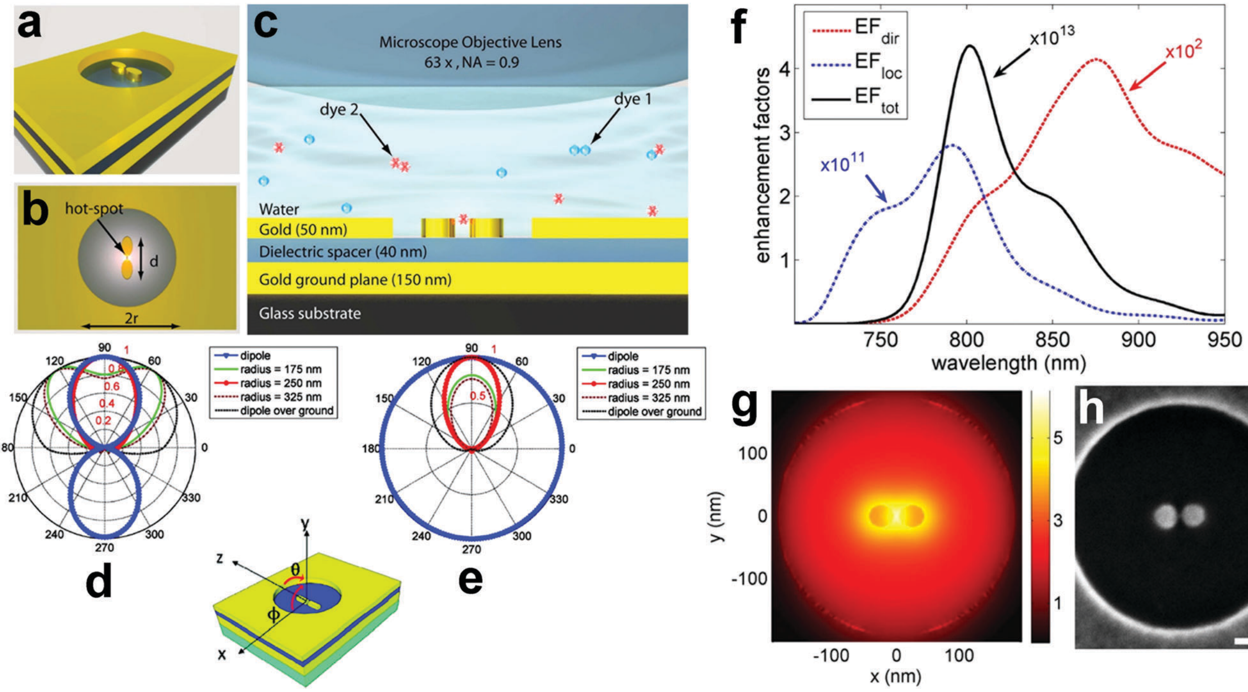

Fig. 12 (a) Schematic of a hierarchical SERS substrate consisting of a nanoparticle dimer (length, 80 nm, gap, 6 nm), and a resonant ring-reflector antenna of radius 190 nm. (b) Top view showing the hotspot. (c) Side view. Simulated radiation patterns of a simple dipole antenna, dipole over ground plane and the nanoantenna structure for various radii of the circular reflector. The patterns are normalized to the maximum in the (d) *yz* plane; (e) *xy* plane. (f) Enhancement factors for (dashed red) the power radiated by the nanoantenna out of the plane of the substrate normalized to that of a dipole over a glass substrate; local (dot-dashed blue), the normalized electric field intensity square $|\boldsymbol{E}_{\text{loc}}/\boldsymbol{E}_0|^4$, that reaches values as high as 10^{11} due to a small feed-gap and the ground reflector; (solid black) the product of directional and local EFs. At 800 nm, a total EF of 4.2×10^{13} is computed. (g) Normalized electric field intensity $|\boldsymbol{E}|^2/|\boldsymbol{E}_0|^2$ profile (log scale) at 800 nm chosen so as to serve both the excitation at 785 nm and the Stokes-shifted radiation at 825 nm. (h) Scanning electron microscopy image of the fabricated nanoantenna with a feed-gap of ∼6 nm and dipole length and width of 80 and 35 nm, respectively. The scale bar is 90 nm. Images (a–c) and (f–h) adapted from ref. 163 with permission, copyright (2012) American Chemical Society; images (d) and (e) adapted from ref. 162 with permission, copyright (2011) American Chemical Society.

The hierarchical field concentration approach can be used for single-molecule SERS detection, even when the nanogap between two nanoparticles is as large as 6 nm.

Crozier and coworkers elucidated the notion of hierarchical field concentration for SERS. They designed and prepared a hierarchical structure consisting of large optical antennas (Au strips and a Au ground plane film) and a Au nanoparticle dimer[164] (Fig. 13). The hierarchical structure produced up to 20-fold enhancements over the dimer alone. Crozier and coworkers reported another optical antenna also based on hierarchically structured arrays to detect single-molecule SERS. The unit of the optical antenna arrays consisted of a dimer of Ag nanorods surrounded by a Ag ring, and a Au ground plane film.[165] Huang and coworkers reported a hierarchical structure consisting of nanoparticles inside a cavity[166] from which they obtained a 10^2 additional enhancement over what the nanocavity produced without nanoparticles (Fig. 14).

The aforementioned examples demonstrate the concept of hierarchical SERS substrates; however, the mechanism of the multiscale EM coupling, and the consequential design principles needed to optimize hierarchical SERS substrates have not yet been fully elucidated, suggesting that future work along these lines may produce SERS substrates with even better performance.

Nanostructures supporting antenna modes coupled with waveguide cavity modes. There are several ways to reduce the volume of hotspots. The first is to prepare coupled plasmonic structures with small gaps. However, the efficiency of such geometries is not solely a function of the size of the gap but also of the geometry of the gap region.[167,168] Nanoparticle dimers produced from particles with flat surfaces, such as nanobars, nanocubes and nanocylinders, possess many of the useful characteristics of a metal–insulator–metal (MIM) waveguide[169] that supports waveguide cavity plasmon modes in addition to the dipolar antenna modes that are excited in, for example, dimers.[170] This additional mode is a Fabry–Perot-like resonance caused by multiple reflections at the entrance and exit slits (which act as two perfect magnetic conductor boundaries), resulting in EM field increases around the entrance and exit slits of the nanoantenna.[169,171,172]

Using nanogaps with flat facets allows one to further optimize the gap for field concentration. For example, one can place high-index dielectric layers on the surfaces (Fig. 15a and b), to increase the wavevector of the guided cavity plasmon, k_{gsp}, in the gap region to improve the resonance condition. With the diameter of the inner and outer cylinder, *d* and *D*, Fabry–Perot resonator resonance condition for such a resonator is given by:[167,170]

$$k'_{\text{gsp}}d + k''_{\text{gsp}}(D - d) = 2\pi \tag{37}$$

Published on 29 Junie 2017. Downloaded by Fail Open on 2025-05-07 9:23:53 vm..

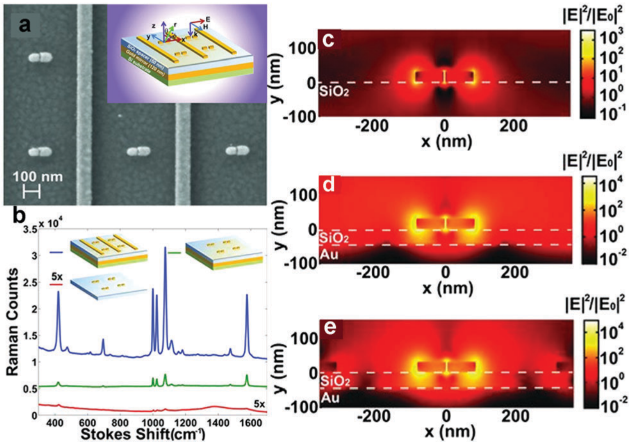

Fig. 13 Schematic of a hierarchical substrate for SERS consisting of Au nanorod dimers integrated with Au strips (30 nm thick, 110 nm wide) and a Au mirror. Each rod is 85 nm long. The outer ends have radii of curvature of 30 nm, while the inner ends are flat. The width of the rods in the y direction is 60 nm. The inner ends of the rods are separated by gaps of 5 nm. The x- and y-periods of the structure are both 730 nm. Calculated intensity enhancement (ratio between the intensity $|\boldsymbol{E}|^2$ of the enhanced local field and the intensity $|\boldsymbol{E}_0|^2$ of the incident wave) in the xz plane resulting from an array of Au nanorods dimers on a SiO_2 substrate (c), that resulting from the array of optical antennas above the Au ground film with a SiO_2 spacer (d) and that resulting from an array of optical antennas integrated with gold strips, a SiO_2 spacer and a gold mirror. Image adapted from ref. 164 with permission. Copyright 2012 John Wiley & Sons, Inc.

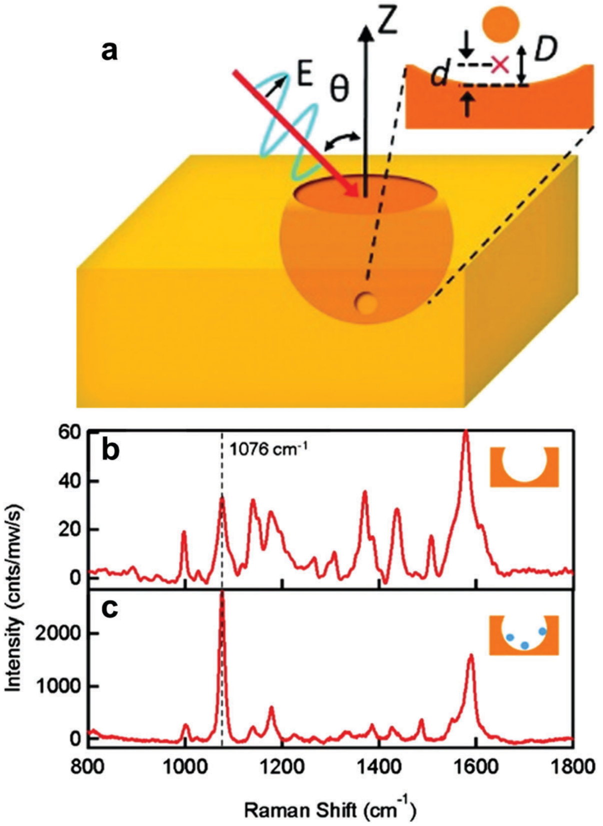

Fig. 14 Schematic of a hierarchical substrate for SERS consisting of a particle-in-cavity geometry (a), the measured SERS spectra of a monolayer of 4-aminothiophenoladsorbed in a 600 nm Au void, without (b) and with (c) 20 nm Ag nanoparticles. Excitation laser, 633 nm. Image adapted from ref. 166 with permission, Copyright (2011) American Chemical Society.

in which k'_{gsp} and k''_{gsp} are the wavevectors of the gap surface plasmon at the dielectric/metal interface, and at the air/metal interface. The local field in the gap region can be significantly enhanced by the plasmon hybridization between the (less radiative) waveguide mode and the (more radiative) dipolar antenna mode. As shown in Fig. 15c and d, the hybridization leads to multiple dips in the scattering spectra, and a much greater overall local field enhancement. Eqn (37) shows that the cavity resonant frequency can be tuned by varying the depth and thickness of the dielectric core. The local field enhancement inside the waveguide cavity is maximized when the waveguide cavity and antenna resonant frequencies coincide with each other.

3.2.3 Quantum effects at small inter-particle distances.

A small gap is preferable for single-molecule SERS; however, the local EM field and SERS EF cannot be increased without limit by decreasing the gap size to the sub-nanometre scale. Crozier and coworkers reported that the maximum SERS EFs measured by wavelength-scanned SERS is reached when the gap-width of a nanodisk dimer is decreased to 0.6 ± 0.1 nm (Fig. 16a). This was attributed to quantum electron tunnelling effects between the coupled NPs.[173–177]

The authors were able to reproduce the experimental observations using a quantum-corrected classic model (QCM) proposed by Aizpurua and coworkers to calculate the local field enhancement.[178] In the QCM, the junction is modelled by a local dielectric function that includes electron tunnelling and the tunnelling resistivity of the gap region. This is achieved by modifying the Drude dielectric function in the gap region as follows:[173]

$$\varepsilon_{\mathrm{g}}(\omega, g) = 1 - \frac{{\omega_{\mathrm{p}}}^2}{\omega(\omega + i\gamma_{\mathrm{g}}(g))} \tag{38}$$

where ω_{p} is the effective plasma frequency of gold, ω is the frequency of the incident light and γ_{g} is a gap-width dependent effective damping frequency related to the tunnelling current and is given by:

$$\gamma_{\mathrm{g}}(g) = \gamma_{\mathrm{Au}} \exp(2qg) \tag{39}$$

Here, $q = 1.12 \times 10^{10}\ \mathrm{m}^{-1}$ is the effective decay rate obtained for a gold dimer, by interpolating the results obtained from a full quantum mechanical (full-QM) simulation carried out by iteratively solving the time-dependent Kohn–Sham equation.[178]

The gap region was then divided into several effective layers with various lengths g and $\varepsilon_{\mathrm{g}}(\omega,g)$. Finally, all the layers in the gap region, and other regions were built into a classical electrodynamic model (CEM) for calculating the EM field distribution and optical response in the far field.[173]

In the paper by Aizpurua and coworkers, the authors found that the QCM approach reproduced the far-field and local field behaviour of a Na dimer when the gap-width was reduced below 0.5 nm, whereas the CEM approach failed[178] (Fig. 17).

Published on 29 Junie 2017. Downloaded by Fail Open on 2025-05-07 9:23:53 vm..

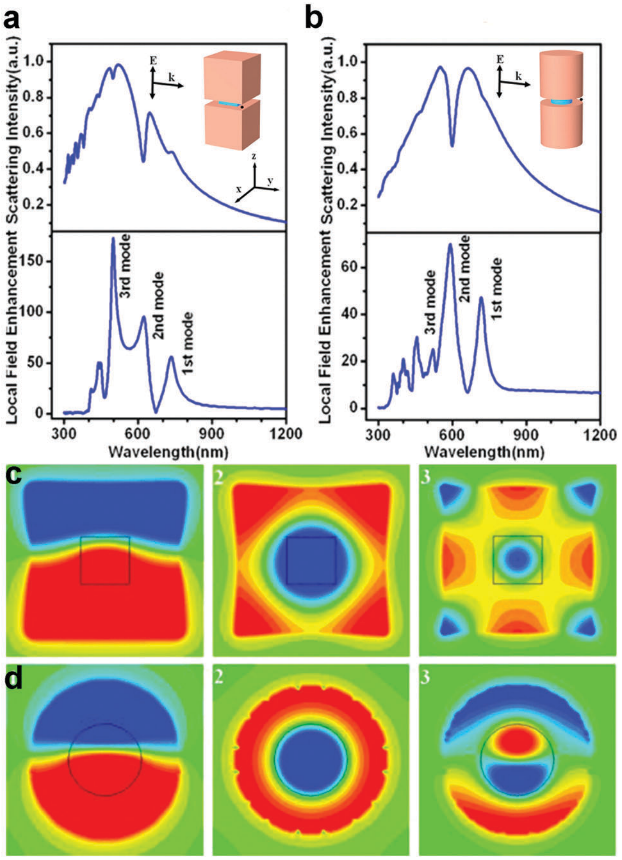

Fig. 15 Simulated far-field scattering spectra and local electric field enhancement at the black dot for (a) a parallel cuboid (depicted in the inset of a) and for (b) a cylinder nanoantenna (depicted in the inset of b). Parameters: (a) Ag: 60 nm × 60 nm × 60 nm; Al_2O_3: 20 × 20 × 2.5 nm. (b) Ag: 60 nm diameter × 80 nm height; Al_2O_3: 30 nm diameter × 2.5 nm height. Snapshots of the local electric fields in the plane through the middle of the dielectric spacer for the parallel cuboid (c) and cylinder (d) nanoantenna. The red region indicates the local maxima and the blue indicates the local minima. The zero amplitude of the electric field is represented by the green regions. The pink colour represents Ag, and the blue represents dielectric materials, Al_2O_3, in the insets of a and b. Image adapted from ref. 167 with permission. Copyright (2010) IEEE.

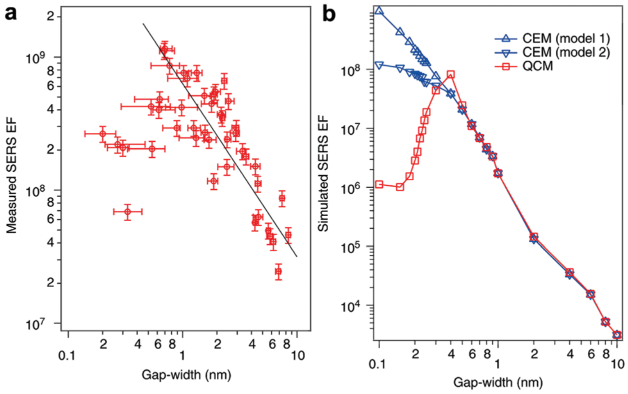

Fig. 16 Effect of quantum mechanical electron tunnelling on SERS EF. (a) Maximum SERS EFs for 45 dimers measured by wavelength-scanned SERS, shown as red circles. The horizontal error bars represent the errors in the gap-width determination. The vertical error bars represent the errors in measuring SERS EFs. Raman measurements for neat thiophenol. The gap-widths range from (2.0 ± 0.6) Å to (9.1 ± 0.4) nm. The maximum SERS EF measured is (1.2 ± 0.2) × 10^9 for Dimer III with a gap-width of (6.7 ± 0.1) Å. Two regions that show opposite trends for SERS EF as a function of gap-width are observed. For gap-widths ranging from 6.7 Å to 9.1 nm, the measured SERS EF generally follows the phenomenological linear fit (in a log–log scale) as log(EF) = 8.8 − 1.3 log(gap-width). The SERS EF generally increases as the gap-width decreases in this region. As the gap-width further decreases from 6.7 to 2.0 Å, the SERS EF does not increase, but instead decreases significantly. (b) Simulated SERS EFs using both QCM and CEM for gap-widths ranging from 1 Å to 10 nm. Only electromagnetic SERS EF is considered, and the simulated EFs are 1–2 orders smaller than the measured values. The CEM simulations of Model 1 assume a monolayer coverage of the thiophenol molecules on the gold surfaces. The CEM simulations of Model 2 consider the hypothetical case for which the thiophenol molecules cannot access the narrowest regions of the gap. Image adapted from ref. 173 with permission. Copyright (2014) Nature Publishing Group.

3.3 Third-generation hotspots

Second-generation hotspots produce very intense field concentrations; however, the widely used materials, such as silicon or ceramics, have proved hard to locate in such small or narrow regions as those shown in Fig. 8. For the surface analysis of materials by SERS, one needs to take account of the EM coupling effect of the probe materials and the SERS-active nanostructures. We refer to hotspots generated from hybrid structures consisting of plasmonic nanostructures and other materials (as shown in Fig. 18) as third-generation hotspots.[5]

Third-generation hotspots result from the hybridization of the EM field scattered from the plasmonic nanoparticles and an EM field reflected from the substrate material surfaces. The resulting SERS EF depends crucially on the dielectric properties of the substrate materials, as shown in the left column of Fig. 18 (a flat Si surface) and in the right column of the same figure (a flat Pt surface). The enhancement can be altered by using various plasmonic nanostructures. For example, the average SERS EF over the projected area of a single Au nanocube on a Si surface (Fig. 18 right) is about two orders of magnitude larger than that of a single Au nanosphere (Fig. 18a, left). The often significant dependence of the SERS EF on the nanoparticle shape is discussed in Section 3.3.1.

3.3.1 An individual coinage-metal nanoparticle on a flat coinage-metal film. Several groups have reported SERS results obtained from molecules interacting with a single particle coupled to a metal film.[179–185] Metiu and coworkers were the first to calculate the local field enhancement of a hybrid structure consisting of a plasmonic nanosphere coupled to a flat, semi-infinite metal substrate with various nanogaps and incident angles (Fig. 19) by analytically solving Laplace's equation in the electrostatic approximation.[84] The results showed that giant local fields and field gradients could be generated in Ag or Au particles separated by a nanogap from the substrate when excited resonantly.

Ciracì and coworkers found that for a Au nanosphere on a flat Au film with a nanogap illuminated by a plane wave incident at 75° from the normal, the propagating surface plasmon was excited in addition to an enhanced local field in the particle–substrate nanogap (Fig. 20). Furthermore, nonlocal

Published on 29 Junie 2017. Downloaded by Fail Open on 2025-05-07 9:23:53 vm..

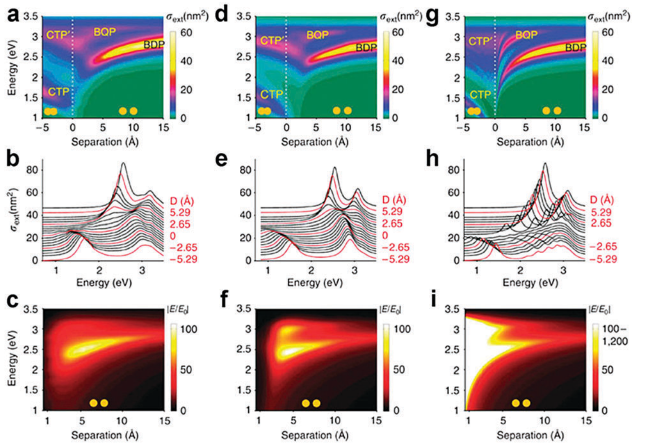

Fig. 17 Optical response of a small metallic dimer within quantum and classical models. Comparison of the optical properties of a metallic dimer obtained with (a and c) the full quantum mechanical model (full-QM), (d and f) with the quantum-corrected classical model (QCM) and (g and i) with a classical electromagnetic model (CEM). The dimer consists of two Na spheres of radius $a \sim 2.17$ nm (40.96 a.u.) in vacuum, separated by a distance g. The incoming field is a plane wave with the electric field $\boldsymbol{E}_0$ polarized along the dimer axis z. The centre of the particles are at $z = \pm(a + g/2)$, and g is negative for overlapping spheres. $g = -2R$ corresponds to the limit of a single sphere. (a, d and g) Show colour plots of the extinction spectra σ_{ext} of the dimers (far-field) as a function of the separation distance g. g is expressed in Angstroms, and the extinction cross-section in nm^2. Zero-separation distance is marked as a vertical dashed line separating the classical non-touching regime and the overlapping regime. Each of these regimes is schematically represented by separated and overlapping yellow dots, respectively. The most relevant modes are identified within the three treatments as following: bonding dimer plasmon (BDP), bonding quadrupolar plasmon (BQP), charge transfer plasmon (CTP) and higher-order charge transfer plasmon (CTP′). (b, e and h) Far-field spectra from selected distances in (a, d and g), respectively. For clarity, a vertical shift proportional to the separation distance is used. Traces in red correspond to separation distances of $D = -5.29$, -2.65, 0, 2.65 and 5.29 Å, as indicated on each graph. (c, f and i) Colour plots of the local field enhancement $|\boldsymbol{E}_{\text{loc}}/\boldsymbol{E}_0|$ (near-field) at the centre of the junction for separations $g > 0.5$ Å. The yellow dots schematically represent the particles in the non-touching regime. Image adapted from ref. 178 with permission. Copyright (2013) Nature Publishing Group.

effects affect the results significantly when the particle–film gap is reduced to 5 nm, and even become the major contributors when the gap is less than 1 nm.[186]

Nordlander and coworkers developed a plasmon hybridization method for treating a solid nanosphere interacting electrostatically with a flat metal surface, in which the conduction electrons of a metal were modelled by a charged, incompressible and irrotational fluid in a uniform, fixed, background of positive ion cores.[19,187] As shown in Fig. 21, there are three distinct regimes of interaction, and the resonance energy and breadth of the hybrid modes strongly depend on the thickness of the flat metal film. The authors found that the interaction between the LSPR of the metal nanoparticle and the SPP of the metal film could result both in virtual resonances with energies in the continuum and in localized states above or below the band, depending on the continuum parameters.

As for plasmon coupling in a nanoparticle dimer with a flat surface in the gap region, the waveguide cavity modes supported by metal-on-substrate systems cannot be ignored.

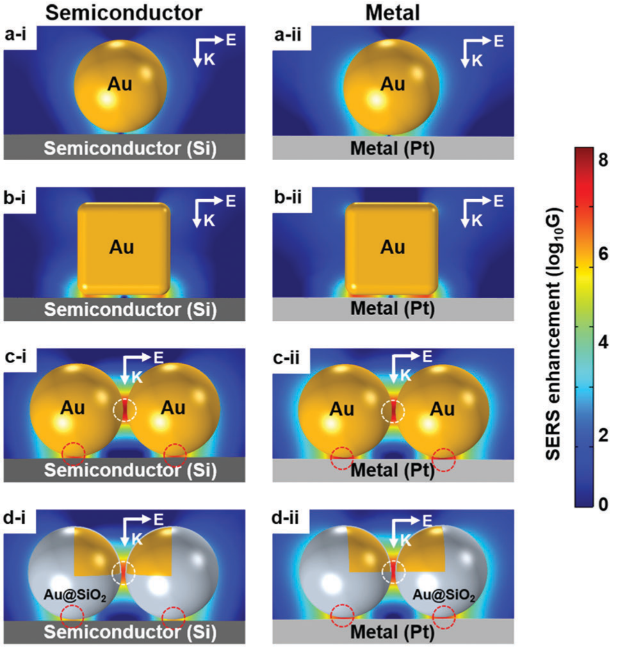

Fig. 18 Third-generation hotspots for surfaces analysis. (a–d) FEM simulations of SERS-enhancement distribution for 'hybrid' nanostructures of SERS-active nanoparticles and Pt and Si probe materials. (a) A bare Au nanosphere monomer on a Si surface (excitation at 530 nm, average SERS EF at substrate $\langle G_{\text{sub}}\rangle = 94$, and SERS maximum EF at substrate $G_{\text{max,sub}} = 2.03 \times 10^3$) and on a Pt surface (excitation at 535 nm, $\langle G_{\text{sub}}\rangle = 1.30 \times 10^3$, $G_{\text{max,sub}} = 4.32 \times 10^4$). (b) A bare Au nanocube monomer on a Si surface (excitation at 660 nm, $\langle G_{\text{sub}}\rangle = 1.48 \times 10^6$, $G_{\text{max,sub}} = 1.42 \times 10^7$) and on a Pt surface (excitation at 825 nm, $\langle G_{\text{sub}}\rangle = 7.31 \times 10^5$, $G_{\text{max,sub}} = 5.15 \times 10^6$). (c) A bare Au nanosphere dimer on a Si surface (excitation at 600 nm, $\langle G_{\text{sub}}\rangle = 1.04 \times 10^5$, G_{max} sub $= 6.85 \times 10^6$, $G_{\text{max,NP}} = 6.76 \times 10^7$) and on a Pt surface (excitation at 630 nm, $\langle G_{\text{sub}}\rangle = 1.02 \times 10^6$, $G_{\text{max,sub}} = 9.01 \times 10^7$, $G_{\text{max,NP}} = 7.19 \times 10^7$). (d) A shell-isolated nanosphere (Au@SiO$_2$) dimer on a Si surface (excitation at 580 nm, $\langle G_{\text{sub}}\rangle = 1.74 \times 10^4$, $G_{\text{max,sub}} = 8.37 \times 10^5$, $G_{\text{max,NP}} = 6.56 \times 10^6$) and on a flat Pt surface (excitation at 600 nm, $\langle G_{\text{sub}}\rangle = 2.07 \times 10^5$, $G_{\text{max,sub}} = 1.16 \times 10^7$, $G_{\text{max,NP}} = 1.39 \times 10^7$). The diameter of the bare Au nanosphere and the core of the Au@SiO$_2$ is 60 nm; the shell thickness of Au@SiO$_2$ is 2 nm. The size of the inter-particle gap (within the region marked with a white dashed circle) in panels (c and d) is 2 nm, and the particle–substrate gap (within the region marked with a red dashed circle) in panels (b and c) is 1 nm. Image adapted from ref. 5 with permission. Copyright (2016) Nature Publishing group.

Xia and coworkers experimentally demonstrated that hotspots with SERS enhancements sufficient for single-molecule detection could be produced by depositing Ag nanocubes on a Au or Ag substrate.[188] Specifically, when a Ag nanocube was placed on a Au or Ag substrate, hotspots were created at the corner sites of the nanocube that were in contact with the metal substrate (Fig. 22).

Bowen and Smith developed a coupled-mode theory to analyse the local-field and far-field properties of film-coupled plasmonic nanocubes with small particle–substrate gaps.[189] Briefly, they found that the local field $\boldsymbol{E}(\boldsymbol{r})$ and $\boldsymbol{H}(\boldsymbol{r})$ under a film-coupled nanocube computed from the inhomogeneous Maxwell's equations:

$$\nabla \times \boldsymbol{H}(\boldsymbol{r}) = j\omega\varepsilon_0\boldsymbol{E}(\boldsymbol{r}) + \boldsymbol{J}_{\text{e}} \tag{40a}$$

$$\nabla \times \boldsymbol{E}(\boldsymbol{r}) = -j\omega\mu_0\boldsymbol{H}(\boldsymbol{r}) - \boldsymbol{J}_{\text{m}} \tag{40b}$$

Published on 29 Junie 2017. Downloaded by Fail Open on 2025-05-07 9:23:53 vm..

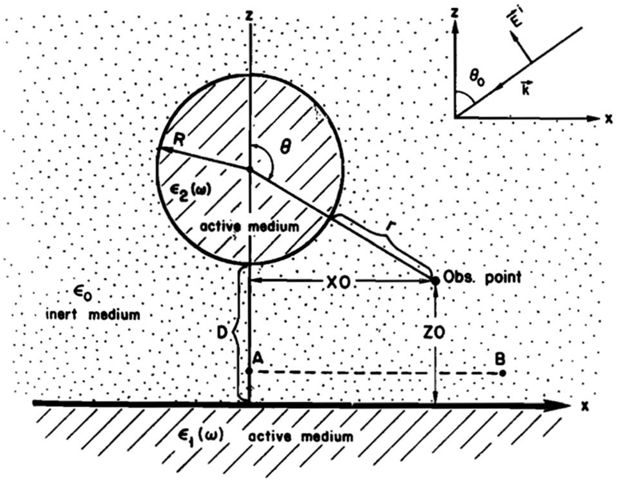

Fig. 19 The geometry of the system: a planar interface separates the active medium of dielectric constant $\varepsilon_1(\omega)$ from the inert medium of dielectric constant $\varepsilon_0(\omega)$. Image adapted from ref. 84 with permission. Copyright (1983) Elsevier.

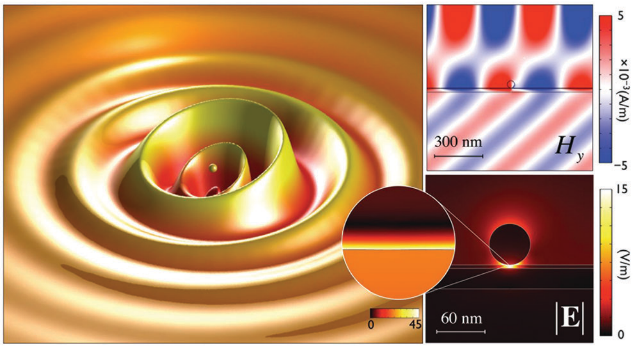

Fig. 20 Simulation of a single film-coupled nanoparticle. (left) Relative electron surface density showing the excited surface-plasmon polariton propagating over the metal film. The nanoparticle can be seen at the centre. (upper right) A plane wave is incident at 75° from the normal on the nanoparticle. (lower right) A close-up of the near fields surrounding the nanosphere; note the large field amplitude directly below the sphere. Looking closer yet, it can be seen that the fields penetrate into the nanosphere by a distance in the order of the Thomas–Fermi screening length. Image adapted from ref. 186 with permission. Copyright (2003) AAAS.

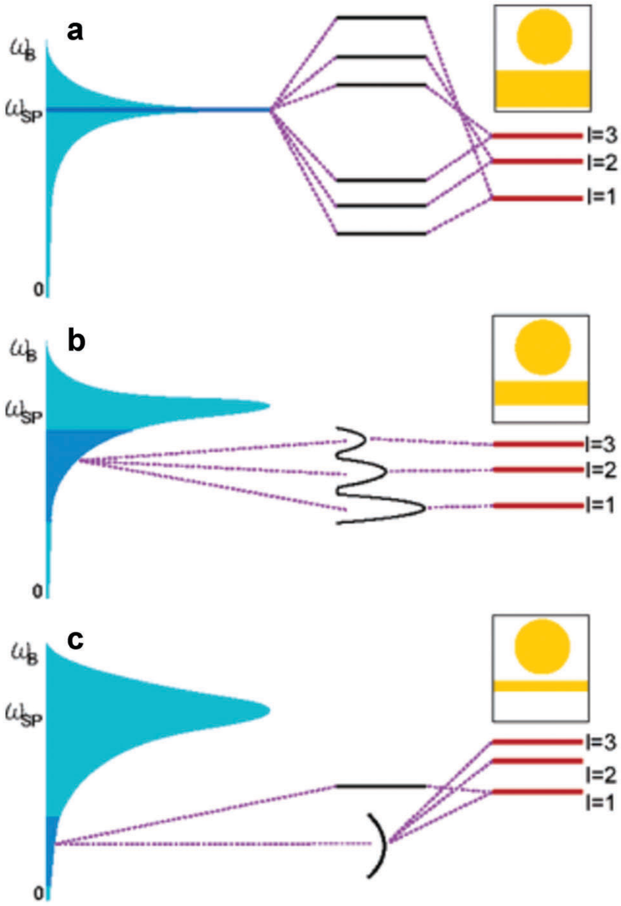

Fig. 21 (a) Schematic (left) depicting the geometrical parameters of the interacting nanoparticle and film and SEM image (right) of a representative experimental sample consisting of dispersed Au nanoparticles on a thin Au film and (b–d) schematics illustrating the three regimes of interaction for the plasmonic continuum of a conducting film (left) with the discrete plasmons of a nanosphere (right): (b) "thick film" ($T > 2Z$), where T is the thickness of the film, Z is the particle–substrate separation; (c) intermediate film thickness ($T \approx Z$); (d) "thin film" ($T < Z/2$). The interactions between nanosphere and thin film plasmons are determined by the effective continuum $\rho V2$ (dark blue), where $\rho(\omega)$ is the plasmon density of states of the film (light blue) and $V(\omega)$ is the interaction between a nanosphere plasmon and a film plasmon of energy ω. Insets show the geometries to approximate scale. Image adapted from ref. 19 with permission. Copyright (2004) American Chemical Society.

could be expanded as a sum over a set of lossless and orthogonal waveguide eigenmodes.

$$\boldsymbol{E}(\boldsymbol{r}) = \sum_{\mu} e_{\mu}(\omega)\boldsymbol{E}_{\mu}(\boldsymbol{r}) \tag{41a}$$

$$\boldsymbol{H}(\boldsymbol{r}) = \sum_{\mu} h_{\mu}(\omega)\boldsymbol{H}_{\mu}(\boldsymbol{r}) \tag{41b}$$

The lossless eigenmodes $\boldsymbol{E}_\mu$ and $\boldsymbol{H}_\mu$ satisfy the homogenous Maxwell's equations:

$$\nabla \times \boldsymbol{H}_{\mu}(\boldsymbol{r}) = j\omega_{\mu}\varepsilon_0\boldsymbol{E}_{\mu}(\boldsymbol{r}) \tag{42a}$$

$$\nabla \times \boldsymbol{E}_{\mu}(\boldsymbol{r}) = -j\omega_{\mu}\mu_0\boldsymbol{H}_{\mu}(\boldsymbol{r}) \tag{42b}$$

The eigenvalue problem in eqn (42) could be solved by using the perfect magnetic conductor (PMC) boundary condition (Fig. 16b) and lossless metal boundary conditions, by assuming that the dielectric function of the metal is a real number. The lowest eigenmodes are shown in Fig. 23. Radiation stimuli and responses such as the coupling of the incident field to the eigenmodes and the radiative losses were determined analytically using the lossless eigenmode fields, with the Ohmic losses taken into account as a perturbation by using an equivalent surface impedance determined by integrating the Poynting vector over the metal surfaces.[189]

In addition to the square patch antenna, circular, elliptical and other regular-shaped patch antenna problems can be calculated analytically using the extended MIM theory. Wei and coworkers calculated the waveguide cavity modes of a circular patch antenna, and also determined the normal waveguide cavity modes.[192]

Published on 29 Junie 2017. Downloaded by Fail Open on 2025-05-07 9:23:53 vm..

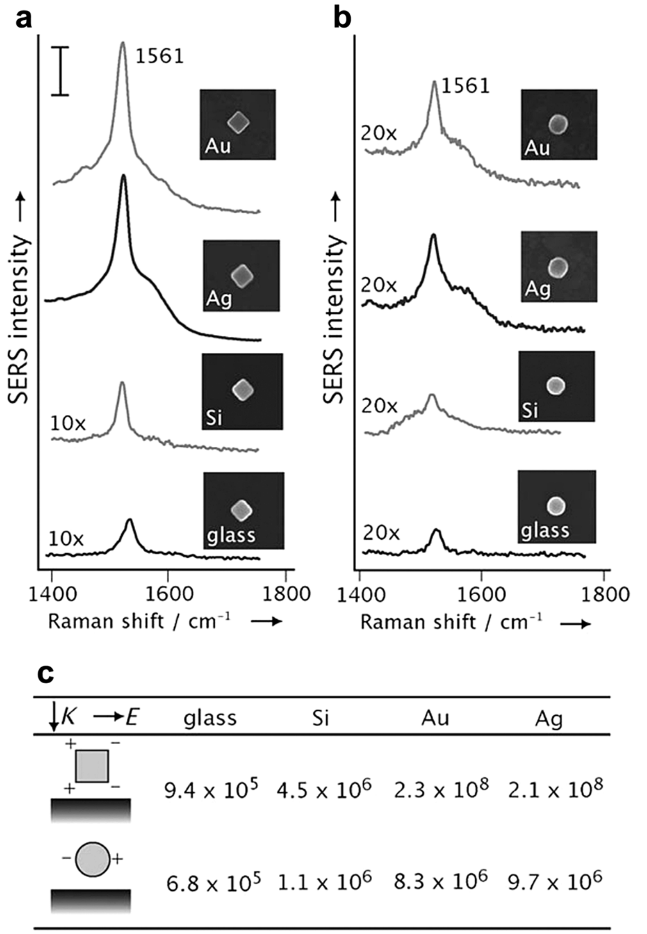

↓K →E	glass	Si	Au	Ag
	9.4×10^5	4.5×10^6	2.3×10^8	2.1×10^8
	6.8×10^5	1.1×10^6	8.3×10^6	9.7×10^6

Fig. 22 The SERS spectra of 1,4-BDT from: (a) nanocubes, (106 ± 5) nm in edge length and (b) nanospheres, (97 ± 7) nm in diameter, on a Au film, Ag film, Si wafer and glass cover slip, respectively. The insets show their corresponding SEM images. The scale bar for the SERS spectra is 10 adu mW^{-1} s^{-1}. (c) The EFs for a single Ag nanocube and nanosphere, respectively, supported on different substrates. Each value reported in this table represents an average of the data from 40 particles. The cartoon shows the propagation and polarization directions of the laser used in this study and a simplified distribution of dipolar charges on each type of particle. Image adapted from ref. 188 with permission. Copyright (2011) Wiley-VCH Verlag GmbH & Co kGaA, Weinheim.

As was found for the dimers of nanocubes or nanocylinders, the local field in the gap region can be significantly enhanced by plasmon coupling waveguide cavity modes to dipolar antenna modes. Aizpurua and coworkers demonstrated that the antenna mode l_1 could hybridize with symmetry-allowed waveguide modes, such as s_{02}, and s_{03} (Fig. 24).[190]

Baumberg and coworkers systematically compared the two fundamentally different resonant gap modes: transverse waveguide (s) and antenna modes (l), which, although both are able to strongly confine light in gaps, have very different near-field and far-field radiation distributions. They showed experimentally and theoretically, that changing the nanoparticle shape from a sphere to cube and varying the gap size alters the coupling of s and l modes, resulting in strongly hybridized (j) modes[191] (Fig. 25).

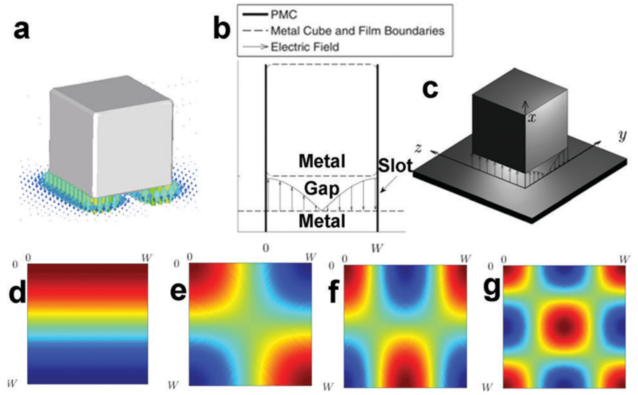

Fig. 23 (a) Fields from a simulated film-coupled nanocube at the resonance frequency of the $\boldsymbol{E}_{01}$ mode. (b) The lossless cavity eigenmode problem, with boundary conditions. (c) Illustration of the coordinate system convention for a film-coupled nanocube. The lossless eigenmodes (d) $\boldsymbol{E}_{0,1}(\boldsymbol{r})$, (e) $\boldsymbol{E}_{1,1}(\boldsymbol{r})$, (f) $\boldsymbol{E}_{2,1}(\boldsymbol{r})$ and (g) $\boldsymbol{E}_{2,2}(\boldsymbol{r})$. Image adapted from ref. 189 with permission. Copyright (2014) American Physical Society.

3.3.2 Multi-particle coupling with a flat metal film for SERS and/or SHINERS.

When a bare Au nanosphere dimer is placed on a Si or Pt surface, hotspots can be simultaneously produced at the particle–substrate and inter-particle nanogaps (Fig. 18c) at certain incident wavelengths. For dielectric materials, the average SERS EF at the surface in the presence of a Au

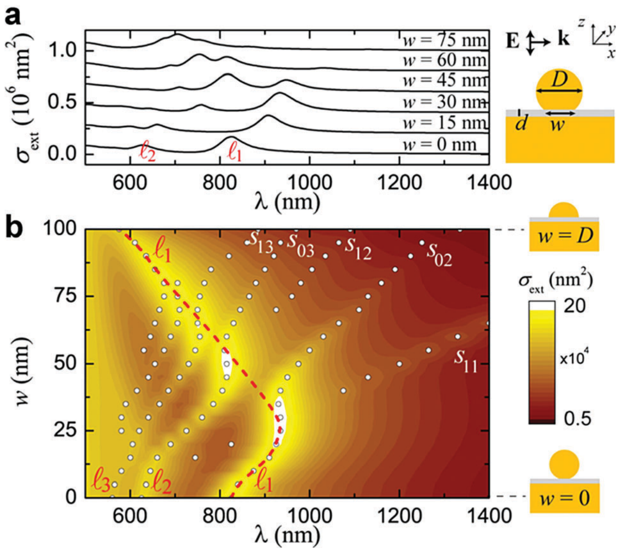

Fig. 24 (a) Extinction spectra for faceted spherical gold NPs with diameter D = 100 nm, separated from a 70 nm-thick gold film by a dielectric spacer of thickness d = 0.6 nm and permittivity ε_d = 1.63, as in the schematic to the right. Consecutive curves correspond to NPs of increasing circular facet diameter from the bottom (w = 0 nm) to the top (w = 75 nm) in steps of 15 nm. The spectra are vertically shifted for clarity. (b) Mapped extinction spectra of the NPoM geometry described in (a) as a function of w (from perfectly spherical NP to hemispherical NP, as in the schematic to the right). Open circles trace the resonance peaks of all the excited modes. Two different sets of modes can be identified and are labelled as l and s modes, according to their symmetry. The red dashed line is a guide to the eye of the l_1 mode. Image adapted from ref. 190 with permission. Copyright (2015) American Physical Society.

Published on 29 Junie 2017. Downloaded by Fail Open on 2025-05-07 9:23:53 vm..

nanosphere dimer (Fig. 18c-i) is about three orders of magnitude larger than that of a single Au nanosphere (Fig. 18a-i). The average SERS EF increases with the increasing refractive index of the dielectric material. For metal surfaces, the average SERS EF at the surface in the presence of a Au nanosphere dimer (Fig. 18c-ii) is about three orders of magnitude larger than that of a single Au nanosphere (Fig. 18a-i) due to the additional plasmonic coupling between the Au nanosphere dimer and the Pt surface.[5] The SERS enhancement also significantly depends on the magnitude of the particle–substrate nanogap and on the wavelength and polarization states of the incident laser.

In shell-isolated nanoparticle-enhanced Raman spectroscopy (SHINERS), hotspots are produced by placing core–shell NPs composed of plasmonic Au or Ag cores with ultrathin (1–5 nm) chemically and electrically inert shells composed of, for example, SiO_2, or Al_2O_3 as probes on a surface. The advantages of SHINERS are two-fold: (1) the ultrathin but pinhole-free shells separate the cores from the material surface (and environment), thus ensuring that there is almost no chemical interference from the Au and Ag cores; (2) the chemically inert shell effectively avoids inter-particle and particle–metal substrate fusion, which significantly improves the stability of the NPs and the probe structures (Fig. 18d). SHINERS has been used for the *in situ* characterization of chemisorption and electrocatalytic reactions on various transition-metal single-crystal surfaces that are difficult to probe using Raman spectroscopy.[22,28,134,193–198]

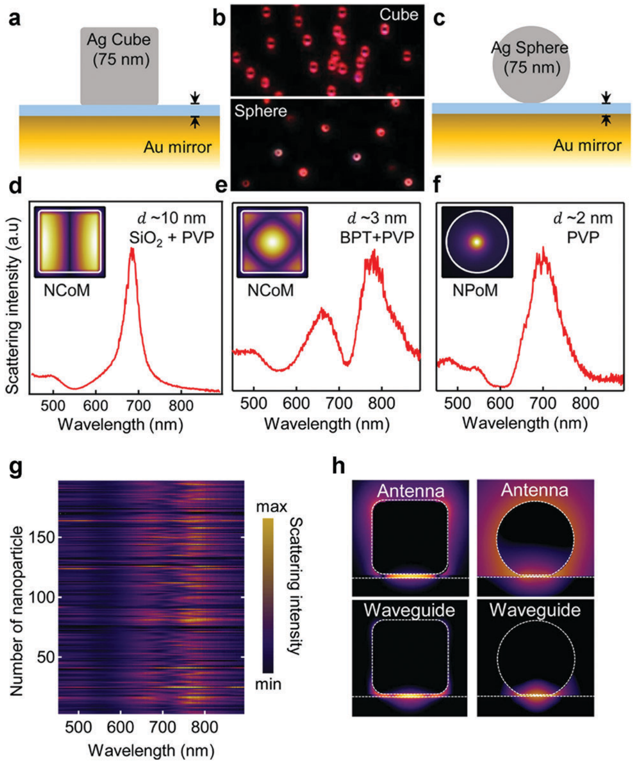

Fig. 25 Nanocube *vs.* nanosphere image dimers. (a) Schematic of a Ag nanocube with 75 nm edge length placed on template-stripped Au with sub-5 nm molecular gaps. (b) Optical dark-field images of (top) nanocubes and (bottom) nanospheres placed on a Au mirror with BPT and PVP spacers, respectively. (c) Schematic of a Ag nanosphere with 75 nm diameter placed on template-stripped Au with sub-5 nm molecule gaps. (d–f) Scattering spectra from 75 nm nanocubes with (d) d = 10 nm SiO_2 spacer and (e) 3 nm BPT spacer and (f) nanosphere with 2 nm PVP spacer. Inset colour maps show the normalized near-field intensity at the resonance wavelength, taken in the middle of the gap parallel to the substrate; white lines indicate the nanostructure edges. (g) Scattering from >200 nanoparticles of 75 nm Ag PVP-coated nanocubes placed on a Au mirror with BPT spacer. (h) Near-field distributions of antenna (l_1) and waveguide (s_{02}) modes for (left) cube and (right) sphere. Image adapted from ref. 191 with permission. Copyright (2017) American Chemical Society.

The shell thickness in SHINERS also allows one to control the Au or Ag core particle–substrate nanogap, consequently allowing determining the degree of particle–substrate EM coupling; also, the Au and Ag cores can increase the local EM field to enhance the Raman signals from the probe substrate without greatly perturbing its structure. The extinction spectra of shell-isolated particles on flat gold are shown in Fig. 26c. A double resonance is observed and a Fano-like dip at ∼600 nm (Fig. 26c and d). The role of plasmonic Fano resonances on SERS is discussed in Section 3.5. As the wavelength crosses 600 nm, the near field at B (the midpoint in the gap) reaches a minimum, while the near field at point *A* increases rapidly. As is typical for Fano resonances, the coupled dipole due to the nanoparticles induces an image dipole in the metal or dielectric surface, forming a magnetic-dipole consisting of a closed circle of electric dipoles (Fig. 26b). This is a plasmonic dark mode with low radiative efficiency, but with a strong near field. At longer wavelengths, the scattering becomes larger, and more effective for Raman scattering processes.[194]

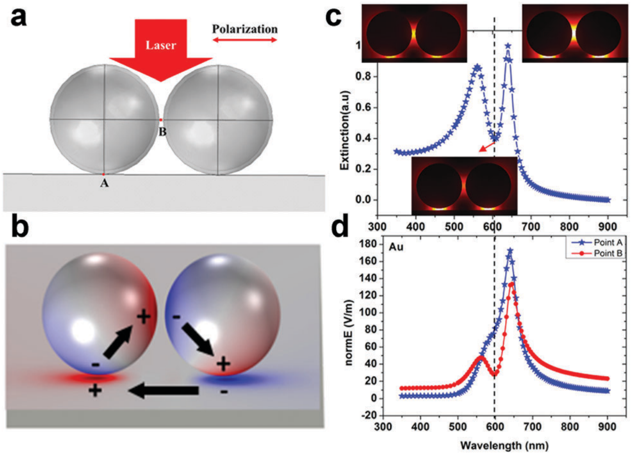

Fig. 26 (a) The simulation model of a 2 × 1 array of 55 nm Au@2 nm SiO_2 NPs placed on a single-crystal surface, which can be made of gold, silver, copper, nickel, silicon, *etc.* The shell-to-shell distance is 2 nm. The polarization of the incident light is parallel to the surface. (b) Surface charge distribution on the surface of gold core and on a flat surface. The simulated normalized extinction (c) and the norm of the electric field of Au@SiO_2 on flat Au surfaces (d). Here, points *A* and *B* are the two representative points between two SHINPs, and between SHINP and the substrates, respectively. The illumination configuration is depicted in (a). Images (a, c and d) adapted from ref. 194 with permission. Copyright (2015) Elsevier.

Published on 29 Junie 2017. Downloaded by Fail Open on 2025-05-07 9:23:53 vm..

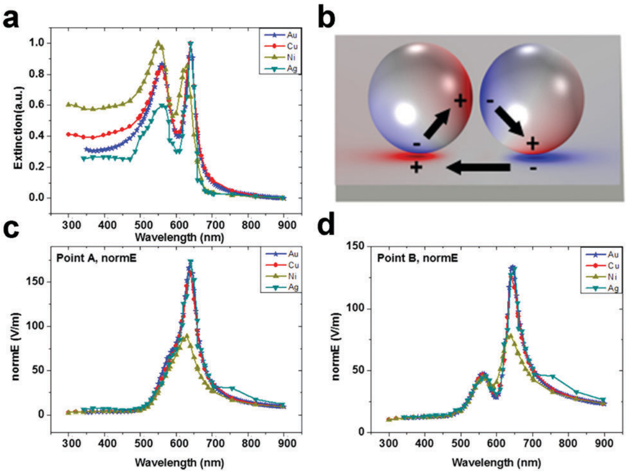

Fig. 27 The simulated normalized extinction (a) and surface charge distribution on the surface of a gold core and on a flat surface (b). The simulated norm of the electric field of Au@SiO$_2$ on flat Au, Cu, Ni, Ag surfaces at point *A* (c) and *B* (d) (point *A* and *B* are depicted in Fig. 26a). Here, points *A* and *B* are the two representative points between two SHINPs, and between SHINP and the substrates, respectively. The illumination configuration is depicted in Fig. 26a.

More interestingly, Au@SiO$_2$ shell-isolated nanoparticles (SHINPs) on various metal surfaces (Au, Ag, Au, Pt, Pd, Ni, Rh, *etc.*) show very similar plasmonic profiles both in extinction and in the distribution of the local EM field at the substrate surfaces (Fig. 27). The apparent difference is the average enhancement factor of the local field at the substrate surfaces. SHINERS, in principle, works well on other transition-metal single-crystal surfaces if the Raman cross-section of the adsorbates is not too small to be measured.

To obtain a higher sensitivity on a flat Au surface, Au@SiO$_2$ nanoparticle clusters can be used instead of single nanoparticles on the surface of the probe material. Yang and coworkers reported that the locations of the hotspots can be efficiently controlled in inter-particle nanogaps, particle–film nanogaps, or in both, by suppressing or promoting specific plasmonic coupling effects in specific wavelength ranges (Fig. 28).

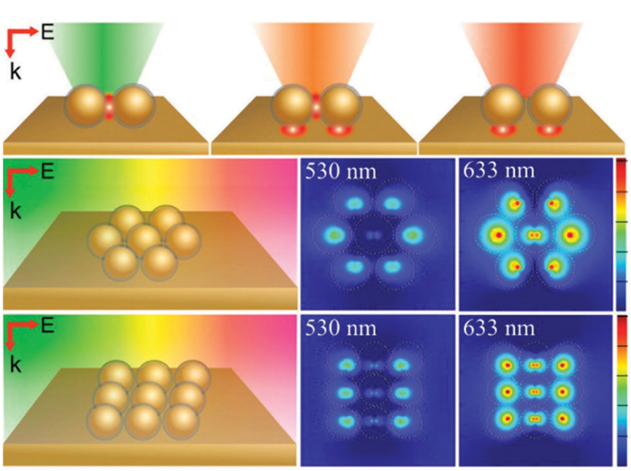

Fig. 28 Local field distribution of a Au nanosphere dimer, heptamer and nonamer on a flat Ag film. Image adapted from ref. 199 with permission. Copyright (2017) American Chemical Society.

3.3.3 Practical numerical simulation of SERS based on particle-on-surfaces. The calculation of a nanoparticle or nanoparticle oligomers coupled with a flat surface can be solved using finite element methods, such as those provided by several commercial packages, such as COMSOL Multiphysics. First, the background field in the absence of the nanosphere under *p*-polarized light excitation is computed. Then, the scattered field is computed. The total physical field is the sum of the background field and the scattered field.

There are two approaches to determine the scattered field, differing in the calculation method for the background field. The first approach is a two-step method. A full-field calculation is performed in the absence of the nanoparticles. Then, the scattered field is computed, setting the calculated field as the background field.

The second approach is to first analytically derive the background field in the absence of the nanoparticles using the Fresnel equations, and then to calculate the scattering field by using the field from the first-step calculation as the background field (Fig. 29).

Considering the reflection and refraction of a *p*-polarized plane wave at a plane interface, the transverse wavenumber is expressed in terms of the incident angle, θ, as follows:

$$k_{\parallel} = \sqrt{{k_x}^2 + {k_y}^2} = k_i \sin\theta \tag{43}$$

Also, the magnitudes of the longitudinal wavevectors are given by:

$$k_{z1} = \sqrt{k_i^2 - \left({k_x}^2 + {k_y}^2\right)}, k_{z2} = \sqrt{k_t^2 - \left({k_x}^2 + {k_y}^2\right)} \tag{44}$$

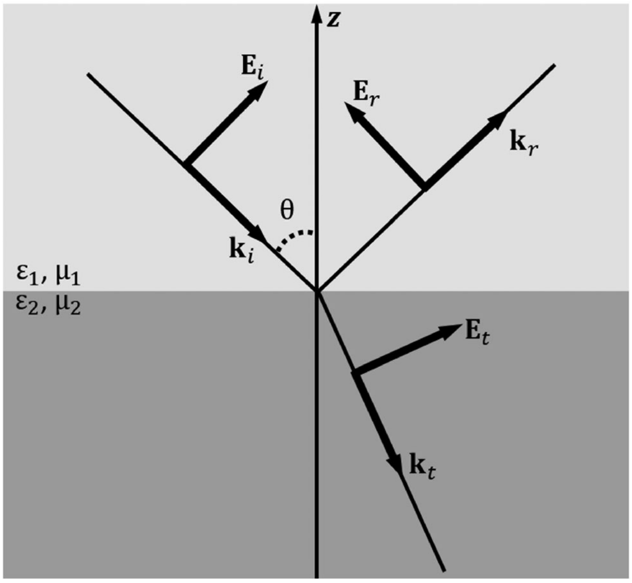

Fig. 29 Pre-definition of the background field for the next electrodynamic calculations of the light-scattering problems of substrate-coupled nanoparticles.

View Article Online

Published on 29 Junie 2017. Downloaded by Fail Open on 2025-05-07 9:23:53 vm..

where k_i, k_r and k_t are the incident, reflected and transmitted wavevectors, respectively.

$$k_\mathrm{i} = \frac{\omega}{c}\sqrt{\varepsilon_1\mu_1} \tag{45a}$$

$$k_\mathrm{t} = \frac{\omega}{c}\sqrt{\varepsilon_2\mu_2} \tag{45b}$$

The background field in the medium of incidence $\boldsymbol{E}_1$ and the medium of transmittance $\boldsymbol{E}_2$ are:

$$\boldsymbol{E}_1 = \boldsymbol{E}_\mathrm{in} + r\boldsymbol{E}_\mathrm{in} \tag{46a}$$

$$\boldsymbol{E}_2 = t\boldsymbol{E}_\mathrm{in} \tag{46b}$$

where the Fresnel reflection and transmission coefficients are defined as

$$r = \frac{\varepsilon_2 k_{z1} - \varepsilon_1 k_{z2}}{\varepsilon_2 k_{z1} + \varepsilon_1 k_{z2}} \tag{47a}$$

$$t = \frac{2k_{z1}\sqrt{\varepsilon_1\varepsilon_2}}{\varepsilon_2 k_{z1} + \varepsilon_1 k_{z2}} \tag{47b}$$

Here, the dielectric constants of the medium of the incidence and the medium of the transmittance are denoted as ε_1 and ε_2, while the magnetic permeability constants are denoted as μ_1 and μ_2.

To calculate the local and far-field optical properties and the SERS EFs of the particle-on-substrate structure, we carried out simulations as described in Section 2.3, as shown in Fig. 30.

The incident angle of the excitation was determined by the choice of the direction of the input power or the background field. If accurate scattered spectra are sought as a function of the numerical aperture (NA), eqn (22) can be modified to:

$$P_\mathrm{sca}(\Omega) = \iint_\Gamma \frac{1}{2}\mathrm{Re}\{\boldsymbol{E}_\mathrm{rel} \times \boldsymbol{H}_\mathrm{rel}{}^*\} \cdot \boldsymbol{n}\mathrm{d}s \tag{48}$$

where $\boldsymbol{E}_\mathrm{rel}$ and $\boldsymbol{H}_\mathrm{rel}$ are the relative electric and magnetic fields respectively, and Ω represents the solid angle, correlated to NA.

Note that surface-plasmon polaritons (SPP) will be excited at the metal substrate. To describe the SPP adequately, the assumed boundary needs to be at least half the decay length of the SPP (*e.g.* 4 μm in the visible).

3.3.4 Gap-mode TERS.

Tip-enhanced Raman scattering was developed by three independent groups, namely those of Zenobi, Anderson and Kawata, who combined atomic force microscopy (AFM) with Raman spectroscopy.[44–46] Pettinger constructed the first scanning tunnelling microscope with Raman spectroscopy (STM-TERS), which was also a gap-mode TERS.[47] TERS with its single hotspot can provide high spatial resolution. The strong coupling between the Au or Ag probe and the Au or Ag substrate results in strong local field enhancements, capable of yielding single-molecule detection with sub-nanometre spatial resolutions.[200]

A great deal of theoretical work has been carried out to elucidate the mechanism and to refine the design strategies for gap-mode TERS. The tip is usually modelled as a cone ending in a hemisphere. The tip sharpness is defined by the tip apex radius and the cone angle (Fig. 31). Plane-wave excitation is usually assumed.

In gap-mode TERS, the coupling strength between the tip and substrate strongly depends on the substrate material. Yang *et al.* reported that gold and silver substrates in gap-mode TERS produce larger enhancements than a platinum substrate due to the large intrinsic losses for platinum in the visible. Pt, in turn, produces a much larger enhancement than non-metallic substrates, such as Si.[201] Additionally, a dielectric substrate with low refractive index couples poorly to the tip and the field distribution is like with an isolated tip (Fig. 32).

Clearly, the tip–substrate distance is an important factor in gap-mode TERS. The resonance wavelength red-shifts as the tip approaches the substrate, accompanied by a higher local electric field enhancement and confinement.[201–208] For distances smaller than 5 nm, the local field enhancement increases dramatically.

Moreover, the tip sharpness will also strongly influence the coupling efficiency. The resonance wavelength blue-shifts with increasing the tip radius, accompanied by a decrease in the local field enhancement.[201,203,205,208,209] Furthermore, the tip material and refractive index of the environment will affect the resonance wavelength and local field intensity.[210]

Metal-coated tips are widely used in AFM-TERS. Kautek and coworkers were the first to consider the influence of coating thickness on the AFM probe.[211] Better spatial resolution is achieved with a thinner coating layer. However, the optimum local electric field enhancement can be achieved by optimizing

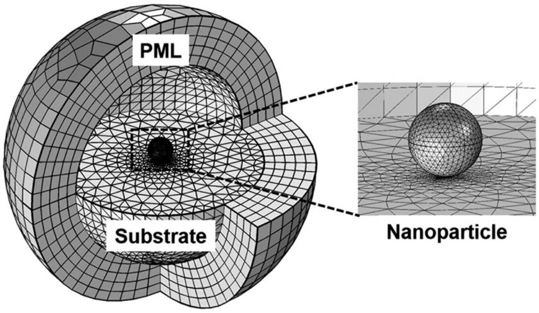

Fig. 30 Simulation model of a nanoparticle on a substrate. The nanoparticle is placed on the substrate. A zoom-in view is on the right. The outside layer is PML.

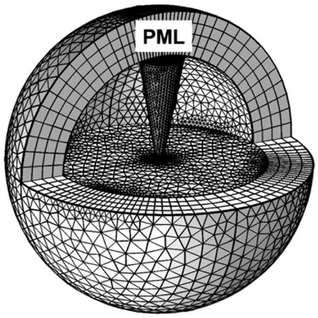

Fig. 31 Typical model in TERS simulations. A metal tip coupled with the substrate; all of the tip, substrate and air are surrounded by the perfect match layer.

This journal is © The Royal Society of Chemistry 2017

Published on 29 Junie 2017. Downloaded by Fail Open on 2025-05-07 9:23:53 vm..

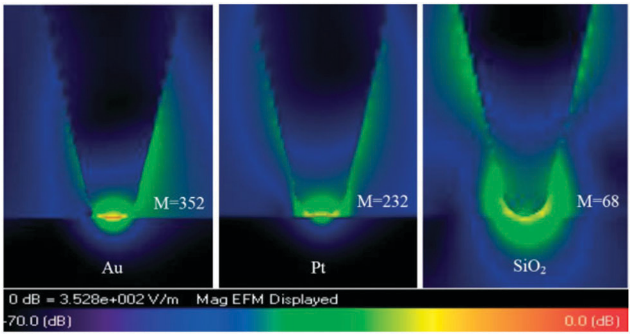

Fig. 32 FDTD simulations of the electric field distribution of a Au tip at a 1 nm distance from Au (left), Pt (middle) and SiO_2 (right) substrates. *M* is the maximum field enhancement. Image adapted from ref. 201 with permission. Copyright (2009) Wiley & Sons, Ltd.

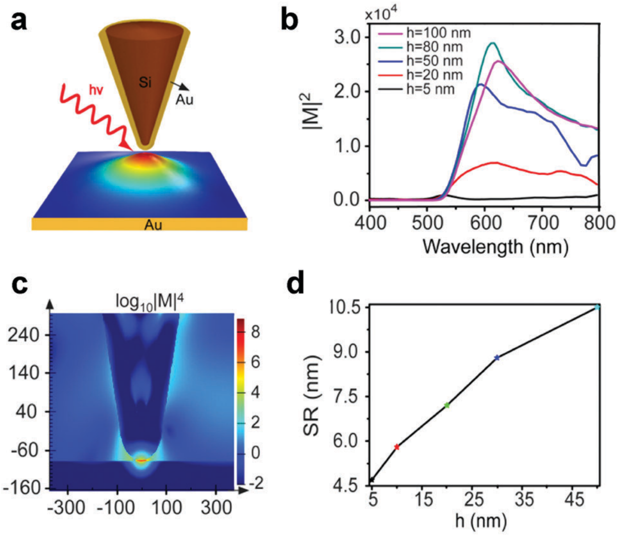

Fig. 33 (a) Calculation model for a Si@Au AFM tip over a gold substrate; (b) the dependence of the electric field enhancement on the thickness (*h*) of the gold coating; (c) the near-field distribution of a Si@Au AFM tip on a gold substrate excited at 615 nm, where θ = 40°, *d* = 2 nm, *h* = 80 nm, *r* = 5 nm; (d) the dependence of the spatial resolution (SR) (using 632.8 nm as the excitation wavelength) on the thickness (*h*) of the gold coating. Image adapted from ref. 209 with permission. Copyright (2015) Optical Society of America.

the coating thickness. Ren, Yang and coworkers found that a coating thickness of 80 nm produced the best results[209] (Fig. 33).

The local field enhancement also depends on the polarization and direction of the incident beams (Fig. 34).

Lagugné-Labarthet and coworkers demonstrated that *p*-polarized light with the polarization along the tip–substrate axis will excite the gap mode, whereas when the polarization is parallel to the substrate coupling is weak (Fig. 35b and d). Furthermore, a radially polarized light will generate much higher local field enhancements than *p*-polarized wave excitation.[206]

3.4 LSPR *vs.* wavelength-scanned SERS

Because SERS arises as a result of surface-plasmon resonances, the SERS enhancement is wavelength dependent. Van Duyne and coworkers performed wavelength-scanned SERS (WS-SERS) measurements on benzenethiol monolayers uniformly adsorbed on four nanosphere lithography (NSL) Ag nanoparticles arrays with four values of LSPR λ_{max} (Fig. 35). The WS-SERS profiles approximately tracked the extinction spectrum of the substrate.[212] Moreover, the maximum SERS enhancement was found to occur when the LSPR max was located between the peak excitation frequency and the vibrational frequency – a "compromise" location, where both the incident and scattered photons can be resonantly enhanced.[212,213]

However, in many other systems, the extinction and scattering spectra correlate poorly with WS-SERS enhancement.[214,215] Van Duyne, Schatz and coworkers showed that hotspot-dominated systems, such as a trimer, show little dependence on the far-field scattering properties due to the differences in the LSPR modes

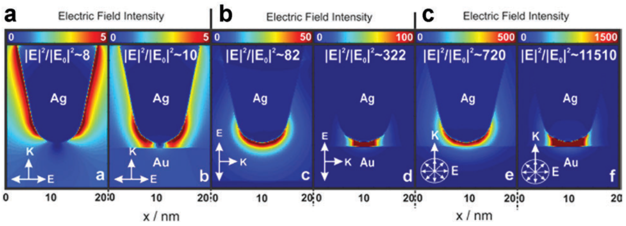

Fig. 34 Field distribution in the tip vicinity under excitation with (a) polarization parallel to the substrate, (b) polarization perpendicular to the substrate, (c) radial polarized light. Image adapted from ref. 206 with permission. Copyright (2013) Optical Society of America.

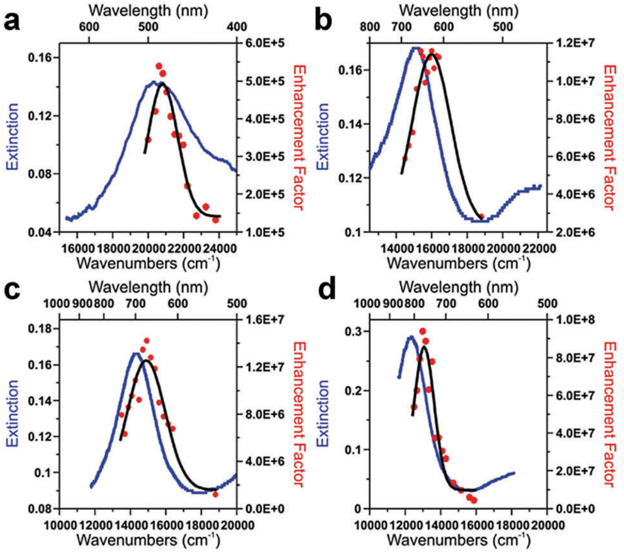

Fig. 35 Wavelength-scanned surface-enhanced Raman excitation spectra of benzenethiol adsorbed on four NSL-derived Ag nanoparticle surfaces of different sizes. Cyclohexane is the intensity standard. (a) Substrate annealed at 300 °C for 1 h. LSPR λ_{max} = 489 nm, profile fit maximum at $\lambda_{ex,max}$ = 480 nm, EF = 5.5 × 10^5. (b) LSPR λ_{max} = 663 nm, profile fit maximum at $\lambda_{ex,max}$ = 625 nm, EF = 1.2 × 10^7. (c) LSPR λ_{max} = 699 nm, profile fit maximum at $\lambda_{ex,max}$ = 671 nm, EF = 1.4 × 10^7. (d) LSPR λ_{max} = 810 nm, profile fit maximum at $\lambda_{ex,max}$ = 765 nm, EF = 9.4 × 10^8. Image adapted from ref. 212 with permission. Copyright (2006) Royal Society of Chemistry publishing.

Published on 29 Junie 2017. Downloaded by Fail Open on 2025-05-07 9:23:53 vm..

excited by the incident waves and the modes locally excited by the molecular dipole (Fig. 36). The authors probed the relationship between the near- and far-field light interactions using a correlated high-resolution transmission electron microscopy (HRTEM)-LSPR-surface-enhanced Raman excitation spectroscopy (SERES) technique. The magnitude of the maximum EF did not correlate with the number of cores in the nanoantenna or with the spectral position of the LSPR, suggesting a separation between near-field SERS enhancement and far-field Rayleigh scattering. Computational electrodynamics confirmed the decoupling of the maximum SERS enhancement from the peak of the scattering spectrum.[214]

The two aforementioned examples show that it is very difficult to perform WS-SERS experiments for individual nanoparticles. To reliably correlate LSPR spectra (or scattering spectra for dark-field spectroscopy) and WS-SERS in individual nanoparticles, one needs to carefully fix the orientation of the nanoparticles and to use a fixed polarization when measuring the dark-field spectra and WS-SERS. Likewise, when comparing simulation results with experimental data, one needs to ensure that such parameters are equivalent in both the experiment and theory. Furthermore, one should take into consideration whether the SERS EF is averaged over all the surfaces in the laser spots (or computed) to ensure that the contribution of all of the hotspots (as well as all of the areas of weak enhancement) are properly taken into account.

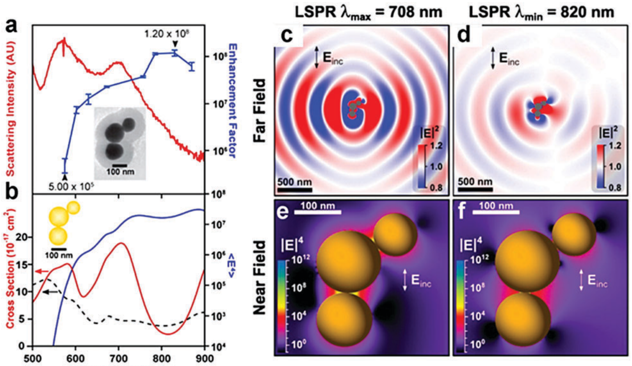

Fig. 36 Experimental and calculated correlated HRTEM-LSPR-SERES data for the nanoantenna trimer presented in the inset of panel (a). (a) Experimental dark-field scattering spectrum (red) and excitation profile for the 1200 cm^{-1} band (blue) of the trimer. (b) Electromagnetic modelling of the nanoantenna trimer, displaying the $\langle \boldsymbol{E}^4 \rangle$ enhancement in solid blue, scattering in solid red, and absorbance with the black dashed line (b). Both experimentally and theoretically, the trimer provides maximal SERS enhancement, where the far-field scattering is relatively weak. Far- (c and d) and near-field (e and f) electromagnetic interactions for peaks and troughs in the LSPR spectrum for the nanoantenna: (c and e) λ_{ex} = 708 nm and (d and f) λ_{ex} = 820 nm. The lower panels show the large electric field enhancement in the gap region between touching spheres. For both wavelengths, the near-field intensity is very similar, as manifested in similar EFs. The far-field scattering intensity is smaller at 820 nm than at 708 nm, as manifested in different LSPR intensities at the studied wavelengths and as illustrated by the difference in the light waves emanating from the particle upon irradiation. Image adapted from ref. 214 with permission. Copyright (2012) American Chemical Society.

3.5 Plasmonic Fano resonance for SERS

Recently, many researchers have reported that plasmonic nanostructures with Fano resonances arise from spectral interferences between broad superradiant modes, such as a dipolar antenna mode, and sharp subradiant modes, such as the high-order modes and photonic crystal modes. The interferences can produce narrow and asymmetric extinction and/or scattering features and a dramatic local field enhancement. Such features have made many groups use or propose to use plasmonic Fano resonance in applications such as sensing, lasing, switching and surface-enhanced spectroscopies, such as SERS and surface-enhanced infrared spectroscopy. Comprehensive descriptions of the fundamental Fano resonance theory and its progress in plasmonic nanostructures can be found in recent reviews.[216–218]

A mechanical analogy of a Fano resonance in a plasmonic system was proposed based on two coupled, damped oscillators driven by an external harmonic force:

$$\ddot{x}_{\mathrm{a}} + 2\gamma_{\mathrm{a}}\dot{x}_{\mathrm{a}} + {\omega_{\mathrm{a}}}^2 x_{\mathrm{a}} + g x_{\mathrm{d}} = f\mathrm{e}^{i\omega t} \tag{49a}$$

$$\ddot{x}_{\mathrm{d}} + 2\gamma_{\mathrm{d}}\dot{x}_{\mathrm{d}} + {\omega_{\mathrm{d}}}^2 x_{\mathrm{d}} + g x_{\mathrm{a}} = 0 \tag{49b}$$

where $x_{\mathrm{a,d}}$, $\gamma_{\mathrm{a,d}}$ and $\omega_{\mathrm{a,d}}$, denote the displacement, friction coefficients and oscillating resonance frequency of two oscillators, the bright (radiative) mode, a, and dark (nonradiative) mode, d, respectively, and parameter g describes the coupling of the two oscillators.

The bright (radiative) mode, which is driven by a harmonic external force $f\mathrm{e}^{i\omega t}$, is highly damped and eqn (49) has a steady state solution in the form of harmonics $x_{\mathrm{a}} = c_{\mathrm{a}}\mathrm{e}^{i\omega t}$ and $x_{\mathrm{d}} = c_{\mathrm{d}}\mathrm{e}^{i\omega t}$, in which the amplitudes c_{a} and c_{d} are given by:[218,219]

$$c_{\mathrm{a}} = \frac{({\omega_{\mathrm{d}}}^2 - \omega^2 + 2i\gamma_{\mathrm{d}}\omega)}{({\omega_{\mathrm{a}}}^2 - \omega^2 + 2i\gamma_{\mathrm{a}}\omega)({\omega_{\mathrm{a}}}^2 - \omega^2 + 2i\gamma_{\mathrm{d}}\omega) - g^2} f \tag{50a}$$

$$c_{\mathrm{d}} = \frac{g}{({\omega_{\mathrm{a}}}^2 - \omega^2 + 2i\gamma_{\mathrm{a}}\omega)({\omega_{\mathrm{d}}}^2 - \omega^2 + 2i\gamma_{\mathrm{d}}\omega) - g^2} f \tag{50b}$$

When ω approached ω_{d}, the two oscillators interfere, giving rise to an asymmetric resonance. For the typical condition $\gamma_{\mathrm{d}} \ll \gamma_{\mathrm{a}} \ll \omega_{\mathrm{a,d}}$, the first denominator $({\omega_{\mathrm{a}}}^2 - \omega^2 + 2i\gamma_{\mathrm{a}}\omega)$ is a constant C that equals $({\omega_{\mathrm{a}}}^2 - {\omega_{\mathrm{d}}}^2 + 2i\gamma_{\mathrm{a}}\omega_{\mathrm{d}})$, and c_{a} could be evaluated in the limit of ω going to ω_{d}. The line shape of $|c_{\mathrm{a}}|^2$ then follows the modified Fano shape:

$$|c_{\mathrm{a}}|^2 = \frac{(\kappa + q)^2 + b}{\kappa^2 + 1} |f/C|^2 \tag{51}$$

where $\kappa = (\omega^2 - {\omega_{\mathrm{d}}}^2 - \omega_{\mathrm{d}}\varDelta)/\varGamma$ is the reduced frequency, $\varDelta = [({\omega_{\mathrm{d}}}^2 - {\omega_{\mathrm{a}}}^2)/g^2]/(|C|^2\omega_{\mathrm{d}})$ is the resonance shift, $\varGamma = 2\gamma_{\mathrm{a}}\omega_{\mathrm{d}}g^2/|C|^2$ is its width, $q = ({\omega_{\mathrm{d}}}^2 - {\omega_{\mathrm{a}}}^2)/(2\gamma_{\mathrm{a}}\omega_{\mathrm{d}})$ is the asymmetric parameter and $b = 4{\gamma_{\mathrm{d}}}^2q^2/\varDelta^2$ is the screening parameter.

An example solution for the absolute value of x_{a} in the frequency domain is shown in Fig. 37b. Eqn (51), which is a mechanical analogy of the Fano resonance for a plasmonic system, is simple and intuitive, yet possesses all of the important features of the plasmonic properties, but in classical electrodynamics terms. Gallinet, Martin and coworkers developed an *ab initio* electromagnetic model for FR in plasmonic

Published on 29 Junie 2017. Downloaded by Fail Open on 2025-05-07 9:23:53 vm..

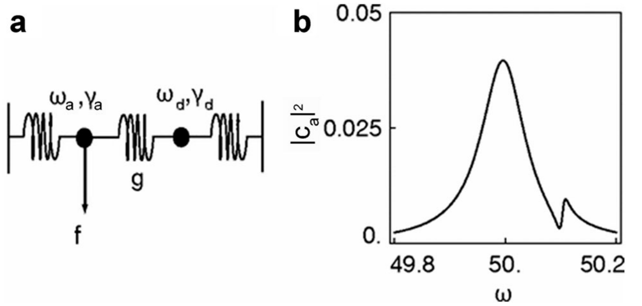

Fig. 37 (a) Mechanical model of Fano resonances: two coupled oscillators of resonance frequencies ω_a and ω_d, and damping γ_a and γ_d. One of them is forced by an external excitation of amplitude *f*. The coupling constant is *g*. (b) Amplitude of the forced oscillator as a function of the excitation frequency for ω_a = 50.0, ω_d = 50.1, g = 2.0, γ_a = 0.05 and γ_d = 0.005. Image adapted from ref. 219 with permission. Copyright (2011) American Physical Society.

nanostructures using the Feshbach formalism by splitting the electric field wavefunction into radiative (bright) and nonradiative (dark) parts.[219,220] The mechanical and electromagnetic models both featured the same four independent parameters, namely Δ, Γ, q and b, describing the asymmetric resonance.

This new approach is more general than the original work by Fano, since the new model includes losses in the materials composing the system. In this approach, the intrinsic losses drive the resonance contrast, while the width is determined mostly by the coupling strength between the nonradiative mode and the continuum.[219] The analytical model is in excellent agreement with numerical simulations of a broad variety of plasmonic nanostructures with Fano resonance, including dolmens, oligomers and gratings.[221] The authors further showed how their comprehensive and insightful theory could be applied to refractive-index sensing by subradiant modes,[222] and to understand the relation between the near-field and far-field properties of plasmonic Fano resonant nanostructures.[223] The radiance or reflectance of the entire plasmonic nanostructure is given by the product of the reflectance of a radiative wave with a symmetrical Lorentzian line shape $R_b(\omega)$ and a Fano-like asymmetric modulation function $\sigma(\omega)$:

$$R(\omega) = R_b(\omega)\sigma(\omega) = \frac{a^2}{\left(\dfrac{\omega^2-{\omega_s}^2}{2W_s\omega_s}\right)^2+1}\,\frac{\left(\dfrac{\omega^2-{\omega_a}^2}{2W_a\omega_a}+q\right)^2+b}{\left(\dfrac{\omega^2-{\omega_a}^2}{2W_a\omega_a}\right)^2+1} \tag{52}$$

where a is the maximum amplitude of the resonance, ω_s and W_s are the resonance frequency and the spectral width of the bright mode, typically, $W_s \ll \omega_s$. ω_a and W_a are the resonance frequency and the spectral width of the dark mode, q is the asymmetric parameter and b is the modulation damping parameter originating from the intrinsic losses, where:

$$b = \frac{{\gamma_i}^2}{(\gamma_c+\gamma_i)^2} \tag{53}$$

The $|c_d|^2$ is the indicator the stored energy,

$$|c_d|^2 \propto \frac{\gamma_c}{(\gamma_c+\gamma_i)^2} \tag{54}$$

Thus, the stored energy reaches its maximum when $\gamma_c = \gamma_i$.

Three regions can be defined according to the relative value of the coupling term γ_c to that of the intrinsic loss γ_i. When $\gamma_c \ll \gamma_i$, we have weak coupling, where the local field is very small, and the peak in the radiance is very sharp, thus weak coupling is suitable for refractive-index sensing. When $\gamma_c \gg \gamma_i$, we have strong coupling, where the local field is also small, and Rabbi-splitting takes place. When $\gamma_c \approx \gamma_i$, the coupling is intermediate, and the local field is at its maximum. Intermediate coupling is the most suitable condition for SERS (Fig. 38).[220]

Crozier and coworkers prepared periodic structures as SERS substrates with two main peaks in the extinction spectra. The resonance wavelengths of the two main peaks could be systematically tuned by varying the periodicity length Λ_x and Λ_y of the periodic structures. By choosing the incident wavelength to coincide with the shorter resonance wavelength and by making the Raman-scattered wavelengths coincide with the second resonance band, a huge SERS enhancement could be obtained[224] (Fig. 39).

Ye, Halas and coworkers reported another example of SERS using nanodisk heptamers, which showed a Fano resonance. They found that in all cases, the largest SERS enhancement was found when both the excitation and the Stokes-shifted wavelengths overlap the Fano resonances[225] (Fig. 40).

Although very many papers have been published on plasmonic Fano resonance, few deal with SERS, likely because of the difficulty of ensuring the simultaneous resonance of both the excitation and the Stokes Raman scattering fields for a molecule resident in a given hotspot. As a result, many opportunities remain for exploiting Fano resonance for SERS.

3.6 Approximation of the $|E|^4$ relation in SERS

The EF $\propto$ $|\boldsymbol{E}|^4$ approximation has been widely used to estimate the SERS enhancements factor. Despite its approximate nature, it is helpful in guiding the design of SERS-active substrates, and for optimizing the choice of excitation conditions. Nevertheless, one needs to use the approximation carefully under some circumstances.

3.6.1 Theoretical background of the approximation of the $|E|^4$ relation in SERS. A model proposed by Le Ru and depicted in Fig. 41a positions a molecule at point O near a dielectric or metallic substrate.[4] The refractive index of the surrounding environment is n_M. A plane wave, with frequency ω_L, is incident along $\boldsymbol{e}_{inc}$ and polarized along $\boldsymbol{e}_e$, perpendicular to $\boldsymbol{e}_{inc}$. By applying Maxwell's equations, we can solve for the local electric field, $\boldsymbol{E}_{loc}(\omega_L)$, at point O, and for $M_{loc}(\omega_L) = |\boldsymbol{E}_{loc}(\omega_L)/\boldsymbol{E}_0(\omega_L)|^2$.

As was done for the radiative enhancement, we consider the signal emitted by the molecule in a given direction along $\boldsymbol{e}_{Det}$. This signal can be divided into two orthogonal signals along $\boldsymbol{e}_{P1}$ and $\boldsymbol{e}_{P2}$, both perpendicular to $\boldsymbol{e}_{Det}$ (Fig. 41b). Here, the optical reciprocal theorem (ORT) can be used to transform the point-dipole problem to plane-wave excitation problems. The ORT

Published on 29 Junie 2017. Downloaded by Fail Open on 2025-05-07 9:23:53 vm..

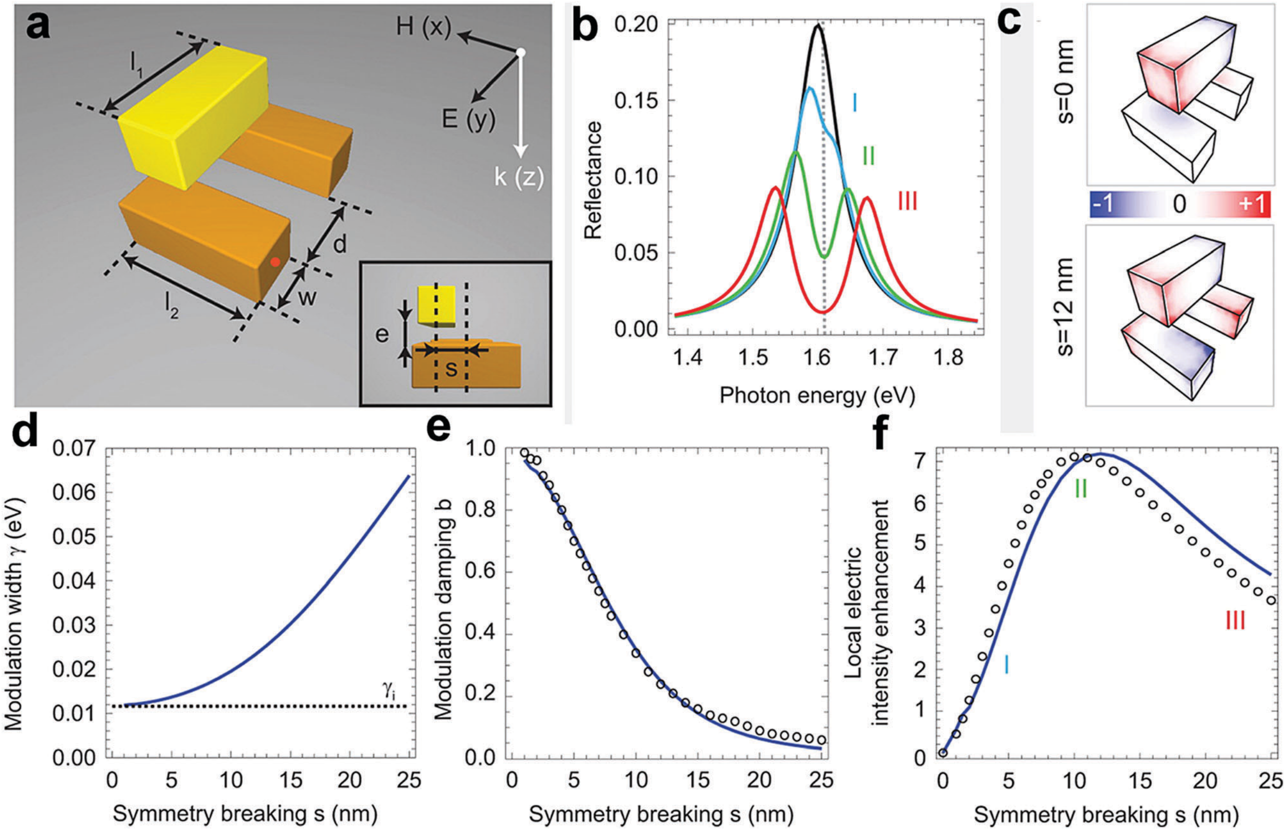

Fig. 38 Symmetry breaking in a plasmonic nanostructure. (a) Schematic of a single nanostructure and definition of the geometrical parameters: $l_1 = l_2 = 100$ nm, $w = 40$ nm, $d = 60$ nm, $e = 20$ nm. (b) Reflectance of a two-dimensional array with a period of 500 nm in both x and y directions for various values of the symmetry breaking s. The permittivity of gold is interpolated from experimental data and the refractive index of the surrounding environment is 1.33 (water). The black, blue, red and green curves correspond to $s = 0$ nm, $s = 5$ nm, $s = 12$ nm and $s = 25$ nm, respectively. In the system with broken symmetry, the resonant excitation of the quadrupolar mode supported by the bottom nanoparticles induces a modulation of the reflectance spectrum. The symbols I, II and III represent the three different coupling regimes. (c) Surface charge distribution at a resonant energy of 1.61 eV for $s = 0$ nm and $s = 12$ nm, respectively. (d) Spectral width of the modulation as a function of the symmetry breaking. The solid blue and the dashed black lines represent the total and the intrinsic width, respectively. (e) Modulation damping b as a function of the symmetry breaking. The solid blue line corresponds to the ratio of the reflectance at a photon energy of 1.61 eV in the symmetry broken system ($s \neq 0$) to the reflectance in the symmetric system ($s = 0$) at the same energy. The black circles correspond to calculations using panel d and the expression of b in eqn (53). In panels d and e, the modulation width and damping are fitted from eqn (52) for $q = 0$. (f) Electric field intensity enhancement related to the quadrupolar mode at 1.61 eV as a function of the symmetry breaking. The solid blue line corresponds to a direct evaluation at 4 nm from the surface of the bottom bar, as shown by a red point in panel a. The black circles correspond to calculations using panel d and eqn (54). Image adapted from ref. 220 with permission. Copyright (2013) American Chemical Society.

states that the field $\boldsymbol{E}$ at point M produced by a dipole $\boldsymbol{p}_A$ (at point O) is related to the field $\boldsymbol{E}_2$ at point O but created by a dipole $\boldsymbol{p}_B$ (at point M).

$$\boldsymbol{p}_A \cdot \boldsymbol{E}_2 = \boldsymbol{p}_B \cdot \boldsymbol{E} \tag{55}$$

Accordingly, we consider the virtual problem of plane-wave excitation with frequency ω_R incoming along $-\boldsymbol{e}_{Det}$ and polarized along $\boldsymbol{e}_{P1}$ or $\boldsymbol{e}_{P2}$. The local field enhancement $|E_{loc}(\omega_R)/E_{inc}(\omega_R)|^2$ at point O is equal to the emission enhancement in the direction $\boldsymbol{e}_{Det}$. This virtual problem has little relation with the real excitation here but will be used as a mathematical strategy with the ORT to solve the re-emission problem. The application of ORT implies that the $|\boldsymbol{E}|^4$ approximation is correct in backscattering.

As discussed in Section 2.2, the SERS enhancement factor can be approximately expressed by:

$$\mathrm{EF}(\omega_0, \omega_R, \boldsymbol{r}_m) = M_{loc}(\omega_0, \boldsymbol{r}_m) M_{Rad}(\omega_R, \boldsymbol{r}_m) \tag{20}$$

The $|\boldsymbol{E}|^4$ approximation consists of three factors. The first is the radiation enhancement, which is roughly equal to the local field enhancement at ω_R, as shown in eqn (17).

$$M_{Rad}(\omega_0, \boldsymbol{r}_m) = \frac{P_{Rad}}{P_0} \approx \left|\frac{\boldsymbol{E}_{loc}(\omega_R, \boldsymbol{r}_m)}{\boldsymbol{E}_0(\omega_R, \boldsymbol{r}_m)}\right|^2 \tag{17}$$

We discuss the derivation of eqn (17) in the next section.

The second is the local field enhancement at ω_R, which is approximately equal to that at ω_0. This leads to:

$$\left|\frac{\boldsymbol{E}_{loc}(\omega_R, \boldsymbol{r}_m)}{\boldsymbol{E}_0(\omega_R, \boldsymbol{r}_m)}\right|^2 \approx \left|\frac{\boldsymbol{E}_{loc}(\omega_0, \boldsymbol{r}_m)}{\boldsymbol{E}_0(\omega_0, \boldsymbol{r}_m)}\right|^2 \tag{56}$$

Substituting eqn (17) and (56) into eqn (20), we get the famous $|\boldsymbol{E}|^4$ approximation, as eqn (21). Now we discuss the

Published on 29 Junie 2017. Downloaded by Fail Open on 2025-05-07 9:23:53 vm..

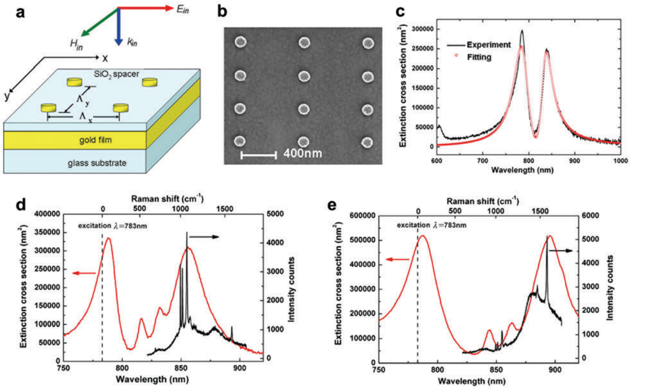

Fig. 39 Measured extinction (left-hand axes) and SERS (right-hand axes) spectra of double resonance structures on which monolayers of benzenethiol are formed. (a) Double resonance structure with a 23 nm thick SiO_2 spacer, gold nanoparticles with diameters of 133 nm and *x*- and *y*-axis periods of 780 nm. (b) Double resonance structure with a 60 nm thick SiO_2 spacer, gold nanoparticles with diameters of 150 nm and *x*- and *y*-axis periods of 760 nm. Dashed line: wavelength of the excitation laser (λ = 783 nm). Image adapted from ref. 224 with permission. Copyright (2011) Optical Society of America.

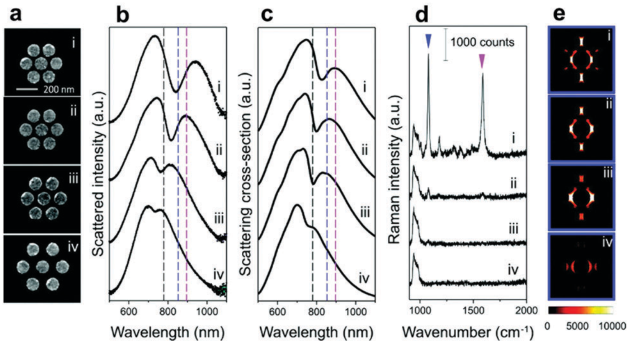

Fig. 40 Scattering spectra and SERS properties of individual Au heptamers with varying gap sizes: (i) ~15 nm, (ii) ~20 nm, (iii) ~30 nm and (iv) ~60 nm. In all cases, the height of the discs is 30 nm and the diameter of the discs is 130 nm. (a) SEM images, (b) experimentally obtained dark-field scattering spectra, (c) calculated scattering spectra (FDTD) and (d) SERS spectra of a monolayer of p-MA molecules on individual heptamers (i–iv) with horizontal incident polarization. Black dashed lines in (b and c) show the excitation laser at 785 nm; blue and pink dashed lines show the Raman Stokes lines of p-MA molecules at 1080 and 1590 cm^{-1} (indicated by the blue and pink arrows in (d)), respectively. (e) SERS maps for the 1080 cm^{-1} Stokes mode of p-MA on heptamers (i–iv) evaluated at one-half the height of the structure. Image adapted from ref. 225 with permission. Copyright (2012) American Chemical Society.

rationality and accuracy of these two factors. In nanostructures with Fano resonance, the resonance peak is very sharp with a full-width at half-maximum (FWHM) ~20 nm. In this case, eqn (56) clearly will not often be appropriate for evaluating EFs for mid- and high-frequency vibrational normal modes. Moreover, the maximum near-field enhancement usually corresponds to a scattering minimum, which means the scattering efficiency is poor at the wavelength of the Fano resonance, in which case, the observed SERS enhancement may deviate significantly from what is predicted by the $|\boldsymbol{E}|^4$ approach.

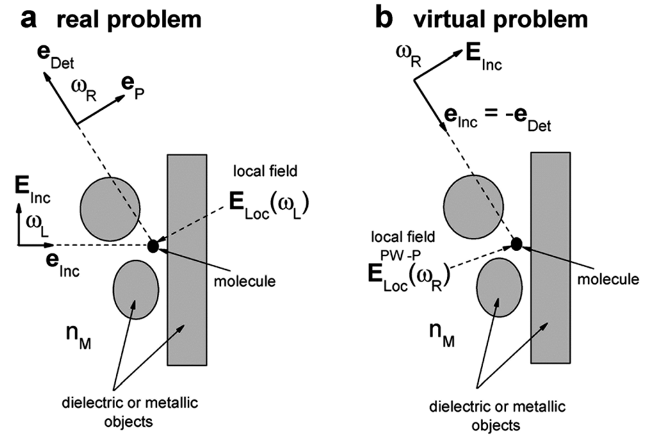

Fig. 41 Schematic representation of the SERS EM problem (for polarized detection), which is solved by considering both the real excitation problem (a) and the 'virtual' plane-wave-excitation problem for re-emission (b). Using the optical reciprocity theorem, the 'virtual' problem (b) allows the calculation of the SERS EF without solving the EM problem of emission from a localized dipole at the molecule position. Image adapted from ref. 4 with permission. Copyright (2009) Elsevier, Amsterdam.

The third is the dependence of the second-step enhancement on the first. This is because the direction of the local field in the first-step enhancement determines the direction of the molecular oscillating dipole moment, which further influences the second-step enhancement. The third factor is strongly related to the surface selection rule of SERS.

3.6.2 Dipole re-radiation effect. The first approximation can be understood by applying the optical reciprocal theorem, as discussed above. We can also calculate the radiation enhancement accurately by taking the dipole re-radiation into account, as described in Section 2. Schatz and coworkers investigated the correlation between dipole re-radiation and $|\boldsymbol{E}|^4$ for a single nanosphere and its dimer (Fig. 42).[122] They found that for small nanospheres, when the detection direction is perpendicular to the incident direction and polarization, the dipole re-radiation will be approximately equal to what is obtained using $|\boldsymbol{E}|^4$. For large nanospheres, however, differences between the two approaches arise primarily due to multimode excitation. Moreover, for molecules positioned at some locations and for some detection directions, the two approaches can produce significantly different results. For the backscattered signal from nanosphere arrays, they found that the dipole re-radiation and $|\boldsymbol{E}|^4$ results were very similar in the long wavelength limit; however, some deviation occurred at short wavelengths and for observer positions other than backscattered (Fig. 43).[125]

Although the $|\boldsymbol{E}|^4$-approximation has been checked in a single-nanoparticle or nanoparticle oligomers-based SERS, it has not been sufficiently analysed for particle-on-substrate systems, including for TERS. For the nanoparticle-on-substrate, the dimensions along *x* and *y* are usually much larger than the incident wavelength. By contrast, for the probe-on-substrate, the dimensions along all directions are larger than the wavelength. Thus, it is necessary to carefully check the validity of the $|\boldsymbol{E}^4|$-approximation in those systems. Moreover, it is also worthwhile

Published on 29 Junie 2017. Downloaded by Fail Open on 2025-05-07 9:23:53 vm..

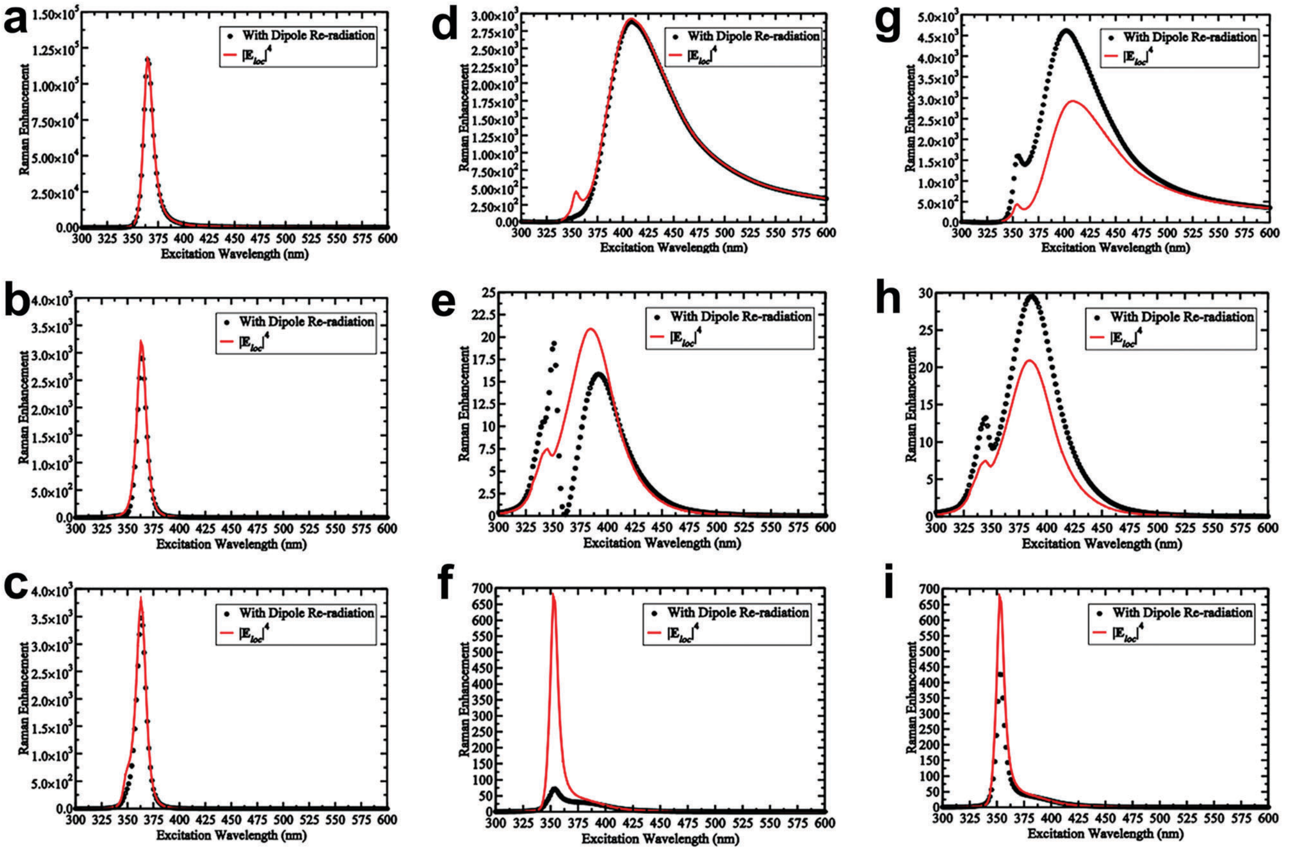

Fig. 42 Comparison between dipole re-radiation and $|E|^4$ of 50 nm Ag nanosphere (a–c) and 100 nm Ag nanosphere (d–i). Dipole is 0.25 nm off the nanosphere in the x (in a, d and g), y (in b, e and h), z (in c, f and i) directions from top to bottom. The origin of the coordinate system is the centre of the nanosphere. The incident plane-wave is along the z direction and polarized along the x direction. The detecting direction is along the y direction in (a–c and d–f), and along the xy direction in (g–i). Image adapted from ref. 122 with permission. Copyright (2009) American Institute of Physics.

to numerically verify the validity of the optical reciprocal theorem in those systems.

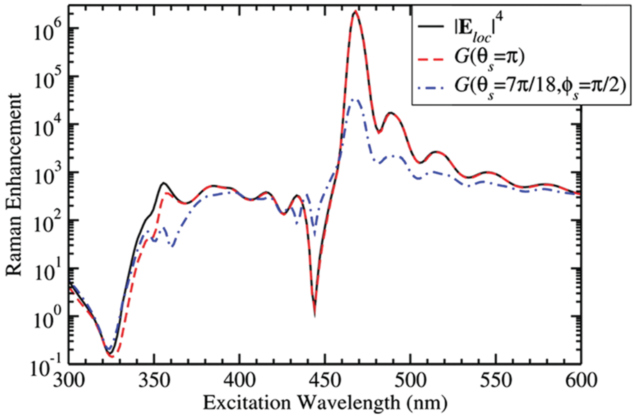

Fig. 43 Comparison between dipole re-radiation and $|E|^4$ of a 112 nm Ag nanosphere 40 × 10 array with a periodicity of 450 nm in the x and y directions. The black line corresponds to the plane wave. The red dashed line corresponds to the backscattering condition of dipole re-radiation. The blue dashed-dotted line represents the result at 70° from the normal. Image adapted from ref. 125 with permission. Copyright (2012) American Chemical Society.

3.7 Hotspots for surface-enhanced nonlinear Raman

Surface or tip-enhanced nonlinear spectroscopies, such as surface-enhanced sum frequency generation, surface-enhanced coherent anti-Stokes Raman spectroscopy (CARS) and surface-enhanced femtosecond stimulated Raman spectroscopy, are very promising for material analysis due to their much higher temporal resolution compared to linear SERS. However, such spectroscopies may require the design and fabrication of appropriate plasmonic nanomaterials and nanostructures.

In CARS, the pump (ω_P) and Stokes (ω_S) fields interact coherently through the third-order polarizability of the dipole-forbidden vibronic modes of the molecule, generating an anti-Stokes signal $\omega_{AS} = 2\omega_P - \omega_S$ with the intensity dependence of a third-order nonlinear optical process:

$$I_{\text{CARS}} \propto |\chi^{(3)}|^2 I_P{}^2 I_S \tag{57}$$

where $\chi(3)$ is the third-order polarizability derivative and I_P and I_S are, respectively, the intensity of incident pumping and of the Stokes field.

The EM enhancement factor in SE-CARS is given by:

$$I_{\text{SE-CARS}} \propto \left|\chi^{(3)}\right|^2 I_P{}^2 I_S \left|\frac{\boldsymbol{E}(\omega_P)}{\boldsymbol{E}_0(\omega_P)}\right|^4 \left|\frac{\boldsymbol{E}(\omega_S)}{\boldsymbol{E}_0(\omega_S)}\right|^2 \left|\frac{\boldsymbol{E}(\omega_{AS})}{\boldsymbol{E}_0(\omega_{AS})}\right|^2 \tag{58}$$

Published on 29 Junie 2017. Downloaded by Fail Open on 2025-05-07 9:23:53 vm..

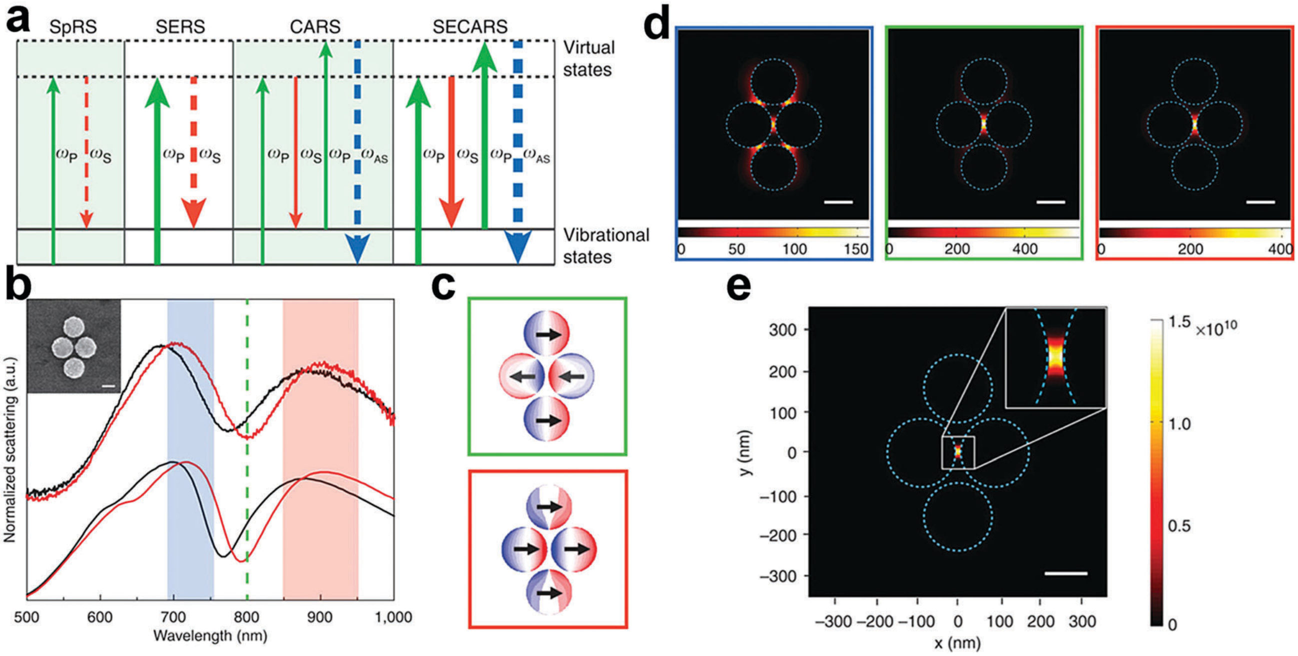

Fig. 44 Different types of Raman processes and the SE-CARS configuration. (a) Energy level diagram showing four types of Raman processes of a molecule. The arrow thickness indicates the transition strength. (b) SE-CARS configuration of two diluted molecules on a nanoquadrumer. A single-wavelength pump laser (ω_P) and a supercontinuum Stokes laser (ω_S) generate an enhanced anti-Stokes scattering (ω_S) of a molecule in the quadrumer central gap. Experimental and FDTD-simulated properties of the quadrumer with a p-MA molecule monolayer coating. (b) Experimental (top) and calculated (bottom) linear scattering spectra of a single quadrumer before (black) and after (red) the p-MA absorption, obtained with horizontal polarization. The calculated spectra for both cases are consistent with their corresponding experimental results. Green dashed line: the pump beam (800 nm); red zone: the Stokes scattering region (848–952 nm); blue zone: the anti-Stokes scattering region (756–690 nm). The Stokes and anti-Stokes regions correspond to Raman shifts of 700–2000 cm^{-1}. The inset shows an SEM image of a gold quadrumer. (c) Charge densities on the top surface of the quadrumer excited at 800 nm pump (top) and 900 nm Stokes (bottom), corresponding to the subradiant and superradiant modes, respectively. (d) Field enhancement intensity (g^2) distribution at the anti-Stokes (left), pump (middle) and Stokes (right) frequencies for the p-MA 1070 cm^{-1} mode evaluated at mid-height of the quadrumer. (e) SE-CARS enhancement ($G_{\text{SE-CARS}} = g_P{}^4 g_S{}^2 g_{AS}{}^2$) map for the mode in d. The maximum enhancement factor is $\sim 1.5 \times 10^{10}$ in the central gap, and significantly lower ($\sim 2.5 \times 10^6$) in the four peripheral gaps. Scale bar, 100 nm. Image adapted from ref. 54 with permission. Copyright (2014) Nature Publishing group.

where $|\boldsymbol{E}(\omega_P)/\boldsymbol{E}_0(\omega_P)|$, $|\boldsymbol{E}(\omega_S)/\boldsymbol{E}_0(\omega_S)|$ and $|\boldsymbol{E}(\omega_{AS})/\boldsymbol{E}_0(\omega_{AS})|$ are, respectively, the local field enhancement at the pumping frequency, the Stokes frequency and the anti-Stokes frequency.

Halas and coworkers reported that single-molecule SE-CARS could be achieved on well-designed nanostructures, such as a quadrumer of nanodiscs (Fig. 44), which supports three localized SPR peaks that correspond to the three beams (two incident beams at different wavelengths and one anti-Stokes Raman-scattered beam) in CARS. Therefore, all the three terms $|\boldsymbol{E}(\omega_P)/\boldsymbol{E}_0(\omega_P)|$, $|\boldsymbol{E}(\omega_S)/\boldsymbol{E}_0(\omega_S)|$ and $|\boldsymbol{E}(\omega_{AS})/\boldsymbol{E}_0(\omega_{AS})|$ could be simultaneously enhanced, which results in a strong enhancement capable of single-molecule detection.[54]

However, the EFs measured in several preliminary experiments were several orders of magnitude less than the predicted values. Clearly more work needs to be done in this exciting area. Perhaps phase matching might be required in addition to energy matching.[226] Surface-enhanced femtosecond stimulated Raman spectroscopy (SE-FSRS) combines the merits of the ultrahigh sensitivity of SERS and the high temporal resolution of FSRS. Van Duyne's group reported the first ground-state SE-FSRS spectra taken on a gold nanoantenna consisting of gold nanoparticle cores functionalized with embedded molecular reporters and capped with a silica shell, which enclosed the molecules, thereby ensuring their location near the gold nanoparticle hotspots (Fig. 45).[55] The authors estimated the ensemble-averaged enhancement factor to be in the range of 10^4–10^6. Furthermore, the authors found that the signal-to-noise ratio could be significantly improved by using 1 MHz repetition rates of the amplified femtosecond laser system instead of the more usual 100 kHz repletion rates.[227]

4 Outlook

4.1 Expanding the theoretical framework to sub-molecule and more complex systems

Along with helpful developments in physics and computational sciences, electromagnetic theories will continue to be a fertile source of new ideas. At the same time, new, exciting experimental results arising from the progress of nanoscience and material science will continue to pose interesting challenges to theoreticians. For instance, Dong and coworkers improved the spatial resolution of TERS to 0.5 nm by dramatically reducing the thermal drift of STM, thereby suppressing the lateral

Published on 29 Junie 2017. Downloaded by Fail Open on 2025-05-07 9:23:53 vm..

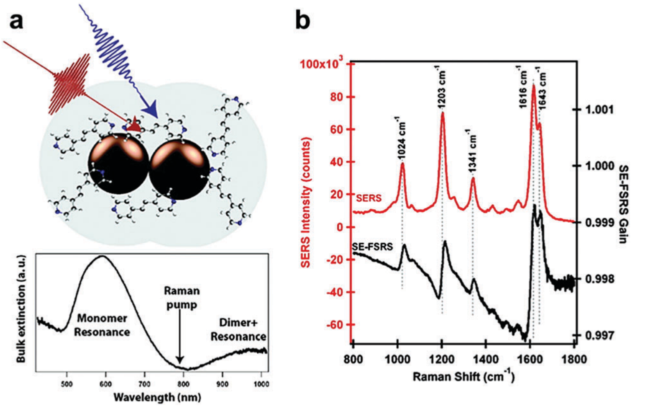

Fig. 45 Schematic depiction of the nanoantennas used in the SE-FSRS experiments. (bottom) Extinction spectrum of the BPE-functionalized nanoantennas, showing the monomer resonance at 600 nm, the 795 nm Raman pump and the multiple core resonances in the NIR region. The band from 500 to 700 nm also contains contributions from dimer, trimer and higher-order core assemblies because these constructs have two localized surface-plasmon resonance peaks. SERS spectrum and SE-FSRS spectrum of *trans*-1,2-bis(4-pyridyl)ethylene (BPE)-functionalized nanoantennas. Both methods obtain high S/N spectra of the well-characterized Raman resonances of BPE, although the SE-FSRS spectrum shows dispersive peaks due to resonance effects from the plasmon. The SE-FSRS spectrum was obtained with 2.0 nJ per pulse Raman pump energy and 100 pJ per pulse probe energy, with an acquisition time of ~8 min, corresponding to 4.5 × 10^7 laser pulses. Peak powers are estimated to be ~10^7 W cm^{-2} for the probe pulse and ~10^5 W cm^{-2} for the Raman pump pulse. Image adapted from ref. 55 with permission. Copyright (2011) American Chemical Society.

movement of molecules at those ultralow temperature.[200] In this way, they were able to resolve adjacent two different porphyrin molecules—metal-centred zinc-5,10,15,20-tetraphenyl-porphyrin (ZnTPP) and free-base meso-tetrakis(3,5-di-tertiarybutyl-phenyl)-porphyrin (H_2TBPP)—immobilized on atomically clean Ag(111) surfaces.[228] In a separate and earlier work, the same group was even able to resolve the internal molecular structure and adsorption configuration of a single H_2TBPP molecule on a Ag(111) surface.[200] Several theoretical studies have been published to interpret the ultrahigh spatial resolution of TERS.[207,229–231] However, the detailed mechanism underlying this unprecedented spatial resolution is still not fully understood.

Single molecules located in plasmonic nanogaps under an external optical field continue to pose significant challenges for TERS, SERS and plasmonics. As an illustrative example, Luo and coworkers considered the inhomogeneous distributions of local fields, modifying the Hamiltonian with a position-dependent electric field to calculate the position-dependent derived polarizability. In this way, the authors tried to interpret the TERS images of a single molecule at a spatial resolution below 1 nm.[229,231]

Several new interesting phenomena have been observed when using TERS or SERS to measure single-molecule conductance.[232–235] For example, Ren and coworkers discovered a correlation between the TERS enhancement and the molecular conductance, especially in the nonlinear regime of the current–voltage response curve.[234] Theoretical studies along these lines are very promising and deepen our understanding of TERS and SERS under external fields.[236,237]

Recently, more complex plasmonic systems have been developed that better utilize the advantages of SERS as a tool for analytical science. Such applications will surely require new, appropriate theories to help interpret the results and guide their development. Third-generation hotspots, which make use of structures based both on non-traditional SERS-active metals and other materials with weak or no SERS activity, are still in the early stages of development. EM coupling in hybrid structures of Au or Ag nanoparticle clusters on non-traditional SERS-active metallic substrates can be very strong if the structural details of the particle–substrate nanogap can be judiciously controlled, as is the case with the shell-isolated strategy. But for the hybrid structures with Au or Ag nanoparticles clusters on dielectric material substrates with a low refractive index, such as Al_2O_3 and bio-membranes, only a small fraction of the hotspots are located at the material surface.

One possible way to overcome this problem is to develop Au and Ag nanocrystals that support coupling plasmonic modes within a single particle, thus supporting hotspots specifically located at the surface of the probe materials. For example, nanocubes can support plasmonic hybridization of a dipolar mode (D) and a quadrupolar mode (Q), which results in a (D + Q) mode with hotspots located on the surfaces of the dielectric substrate, and a (D–Q) mode with hotspots located at the upper vertices of the nanocube.[238] Another way is to use an incident beam at a high angle to the normal. However, to achieve a large range of solid angles, a lens with a high numerical aperture needs to be used at a high incident angle, a condition that is difficult to achieve with most ordinary lenses. Thus, a special lens would need to be designed to simultaneously meet these two requirements.[239] A third way is to use vector polarized light, such as radially polarized light, to more efficiently excite third-generation hotspots on non-metallic substrates. A fourth way is to design hierarchical structures coupled with third-generation hotspots by subwavelength coupling.

Although current EM computational methods are highly developed and widely used, relatively few studies have appeared dedicated to massively screening newly proposed architectures that are claimed to produce better or novel SERS, TERS and/or SHINERS performance. Some intelligent algorithms are employed to solve this problem. For example, Sukharev and coworkers reported an optimal control approach based on multiple parameter genetic algorithms to the design of plasmonic nanostructures with pre-determined optical properties and functionalities.[240] Soliman and coworkers employed an artificial neutral network to predict the propagation characteristics of plasmonic nanostrips and coupling nanostrip transmission lines.[241]

4.2 Towards a unified theoretical framework for SERS

SERS primarily results from near-field enhancements associated with the excitation of intense localized surface plasmons. However, other effects, referred to collectively as ''chemical enhancement'', including molecular resonances, charge-transfer transitions and other processes involving the molecule,

Published on 29 Junie 2017. Downloaded by Fail Open on 2025-05-07 9:23:53 vm..

clearly contribute to the observed enhancement. These contributions vary from molecule to molecule, and account for many interesting aspects of SERS. Several attempts have been made to unify EM and certain non-EM contributions to SERS. The key issue is to develop a way to describe the EM field and the molecular details in a unified theoretical framework. This would help us to analyse in greater detail the spectral features observed in the SERS spectra of surface complexes, adsorbates and reactants. Such a unified theory would also be very helpful towards establishing comprehensive surface selection rules for SERS, TERS and/or SHINERS, which are crucial in surface chemistry.

Lombardi and coworkers developed a discrete-continuum model theory to unify the three possible resonances pertinent to SERS, *i.e.* the surface-plasmon resonance, the molecular electronic resonances within molecules and the charge-transfer resonances between molecules and the metal. In their model, the molecule and metal form a conjoined system, the molecules with discrete levels, while the metal possesses continuum energy levels filled to the Fermi energy, which was assumed to lie between the highest occupied and lowest unoccupied orbitals of the molecules. Fano's protocol[242] was used to address the discrete-continuum coupling. Lombardi *et al.* derived an expression for the transition amplitude between the ground stationary state and some excited stationary state of the molecule–metal system taking all the three resonances into account. Moreover, these resonances were linked by terms in the numerator, which resulted in a SERS selection rule.[243]

Schatz and coworkers developed a hybrid model that coupled classical electrodynamics to quantum mechanics to simulate SERS. The classical electrodynamic method was described by Mie theory or FDTD, while the quantum mechanics was described by time-dependent density-functional theory. In the time-dependent effective potential of time-dependent Kohn–Sham (TDKS) equations, the classic EM field is a dressed external potential. Thus, the hybrid methods, Mie-TDDFT and FDTD-TDDFT, were developed to simulate the absorption and SERS of the metal NP–molecule hybrid system.[244–246] In the hybrid model, the optical response of either a molecule or a molecule–metal complex is described quantum mechanically, while the optical response of the metallic nanoparticles is described by Mie theory or FDTD. This hybrid model appears to use one-way rather than full coupling. In other words, the optical resonance of molecules as an external source could result in an additional response by the nanoparticles; furthermore, the modified optical response of the nanoparticles will likely contribute the modified effective external potential in the TDKS equations. However, no electron transport occurs between the metal nanoparticles and the adsorbed molecules in the hybrid model. An interface through which current can flow and an effective potential connecting QM and EM might be considered as a means to complete the model.[247]

Jensen and coworkers developed a hybrid method called the discrete interaction model/quantum mechanics (DIM/QM) method, which consisted of an atomistic electrodynamics model of the metal nanoparticle and a TDDFT description of the molecule. The DIM/QM method retains the detailed atomistic structure of the nanoparticle by using the atomic polarizability to provide a natural bridge between the electronic structure methods and the macroscopic electrodynamics description provided by TDDFT. The additional external potential in the TDKS equation contains two parts, where $U^{\mathrm{POL}}[\rho]$ is the polarization energy (the energy required to induce the dipoles and charges in the DIM system) and U^{vdW} accounts for the dispersion and repulsion energy between the DIM and the QM system. The authors incorporated their method into a commercial package, called the Amsterdam Density Functional (ADF). Using this approach, they developed a model to simulate the absorption of the metal NP–molecule hybrid system, taking into account the image dipole effect, the inhomogeneous local field effect, the molecule–metal distance effect and the size dependence of the nanoparticle on the resulting SERS spectra.[248,249] Further efforts to treat the short-range charge-transfer by considering a molecule–metal cluster complex and by reformulating the theory to deal with the possible charge transfer between the assembly of polarizable metal atoms and the adsorbed molecules promise to further advance the unified theory of SERS.

Some other methods or models to unify SERS theory have also been reported, including, the polarizable continuum model by Corni,[250] the many-body theory of SERS by Masiello and Schatz,[251] a newly developed molecular cavity optomechanic theory of SERS by Kippenberg and coworkers[252] and its variants by others.[253]

5. Postscript

Our current operational understanding of SERS and related phenomena, in terms of plasmonics, is rather advanced, allowing workers to predict and design SERS-active systems rationally. Nevertheless, an international effort to apply plasmonic theory systematically to develop radically more efficient systems that are able to massively concentrate optical fields so as to exploit the chemical and physical capabilities of such systems has not yet been attempted. This will likely happen in the next few years.

Of course, the theory of SERS as a holistic quantum theory has not yet been achieved. A theory of this sort would remove the artificial divide between the electromagnetic and the chemical views of SERS. Such a holistic theory was the abiding goal of some SERS pioneers.[254]

The near future will certainly bring us a much better understanding of and greater facility in engineering nanomaterials. Also, the advances in theory will guide us to produce high performance SERS substrates and other plasmonic nanosystems that are able to harvest and concentrate photons in ever smaller volumes, leading not only to spectroscopic opportunities but also to important applications in materials science, photochemistry and plasmonics, which ultimately owe their currency to the great international effort that has been dedicated to SERS since its discovery over four decades ago.

Acknowledgements

The authors acknowledge funding supported by the National Natural Science Foundation of China (21403179, 21533006, and

Published on 29 Junie 2017. Downloaded by Fail Open on 2025-05-07 9:23:53 vm..

21621091) and MOST of China (2015CB932300). E.-M.Y. would like to thank Mr Yuan Fang for editing Fig. 1 and 2 of this manuscript, and to thank Mr Mao-Xin Zhang for editing all formulas in right format. S.-Y.D. would like to thank Prof. Hongxing Xu for stimulating discussion on two-step enhancement in SERS, thank Prof. Javier Aizpurua for helpful discussion on nonlocal effect and quantum tunnelling effect in plasmonics, thank Prof. Peter Nordlander for stimulating discussion on plasmonic Fano resonance, thank Prof. Zhilin Yang for discussion on third-generation hotspots, thank Prof. Deyin Wu for discussion on chemical contribution to SERS, thank Prof. Yi Zhao for discussion on charge-transfer contribution to SERS and on quantum effect in plasmonic and SERS.

Notes and references

1 M. Moskovits, *Rev. Mod. Phys.*, 1985, **57**, 783–826.
2 M. Moskovits, *J. Chem. Phys.*, 1978, **69**, 4159–4161.
3 J. A. Creighton, C. G. Blatchford and M. G. Albrecht, *J. Chem. Soc., Faraday Trans. 2*, 1979, **75**, 790–798.
4 E. C. Le Ru and P. G. Etchegoin, *Principles of Surface-Enhanced Raman Spectroscopy and Related Plasmonic Effects*, Elsevier, Amsterdam, 2009.
5 S.-Y. Ding, J. Yi, J.-F. Li, B. Ren, D.-Y. Wu, R. Panneerselvam and Z.-Q. Tian, *Nat. Rev. Mater.*, 2016, **1**, 16021.
6 S. Nie and S. R. Emory, *Science*, 1997, **275**, 1102–1106.
7 K. Kneipp, Y. Wang, H. Kneipp, L. T. Perelman, I. Itzkan, R. R. Dasari and M. S. Feld, *Phys. Rev. Lett.*, 1997, **78**, 1667–1670.
8 G. Haran, *Acc. Chem. Res.*, 2010, **43**, 1135–1143.
9 E. C. Le Ru and P. G. Etchegoin, *Annu. Rev. Phys. Chem.*, 2012, **63**, 65–87.
10 M. Fleischmann, P. J. Hendra and A. J. McQuillan, *Chem. Phys. Lett.*, 1974, **26**, 163–166.
11 D. L. Jeanmaire and R. P. Van Duyne, *J. Electroanal. Chem.*, 1977, **84**, 1–20.
12 M. G. Albrecht and J. A. Creighton, *J. Am. Chem. Soc.*, 1977, **99**, 5215–5217.
13 M. Moskovits and D. P. DiLella, *J. Chem. Phys.*, 1980, **73**, 6068–6075.
14 P. F. Liao, J. G. Bergman, D. S. Chemla, A. Wokaun, J. Melngailis, A. M. Hawryluk and N. P. Economou, *Chem. Phys. Lett.*, 1981, **82**, 355–359.
15 Z.-Q. Tian, B. Ren, J.-F. Li and Z.-L. Yang, *Chem. Commun.*, 2007, 3514–3534.
16 C. G. Blatchford, J. R. Campbell and J. A. Creighton, *Surf. Sci.*, 1981, **108**, 411–420.
17 R. G. Freeman, K. C. Grabar, K. J. Allison, R. M. Bright, J. A. Davis, A. P. Guthrie, M. B. Hommer, M. A. Jackson, P. C. Smith, D. G. Walter and M. J. Natan, *Science*, 1995, **267**, 1629–1632.
18 C. L. Haynes and R. P. Van Duyne, *J. Phys. Chem. B*, 2003, **107**, 7426–7433.
19 H. Wang, D. W. Brandl, P. Nordlander and N. J. Halas, *Acc. Chem. Res.*, 2007, **40**, 53–62.
20 M. J. Mulvihill, X. Y. Ling, J. Henzie and P. Yang, *J. Am. Chem. Soc.*, 2010, **132**, 268–274.
21 L. Qin, S. Zou, C. Xue, A. Atkinson, G. C. Schatz and C. A. Mirkin, *Proc. Natl. Acad. Sci. U. S. A.*, 2006, **103**, 13300–13303.
22 J. F. Li, Y. F. Huang, Y. Ding, Z. L. Yang, S. B. Li, X. S. Zhou, F. R. Fan, W. Zhang, Z. Y. Zhou, D. Y. Wu, B. Ren, Z. L. Wang and Z. Q. Tian, *Nature*, 2010, **464**, 392–395.
23 W. Li, P. H. C. Camargo, X. Lu and Y. Xia, *Nano Lett.*, 2009, **9**, 485–490.
24 M. Hu, F. S. Ou, W. Wu, I. Naumov, X. Li, A. M. Bratkovsky, R. S. Williams and Z. Li, *J. Am. Chem. Soc.*, 2010, **132**, 12820–12822.
25 R. A. Alvarez-Puebla, A. Agarwal, P. Manna, B. P. Khanal, P. Aldeanueva-Potel, E. Carbo-Argibay, N. Pazos-Perez, L. Vigderman, E. R. Zubarev, N. A. Kotov and L. M. Liz-Marzan, *Proc. Natl. Acad. Sci. U. S. A.*, 2011, **108**, 8157–8161.
26 N. G. Greeneltch, M. G. Blaber, A.-I. Henry, G. C. Schatz and R. P. Van Duyne, *Anal. Chem.*, 2013, **85**, 2297–2303.
27 X. Zhang, Y. Zheng, X. Liu, W. Lu, J. Dai, D. Y. Lei and D. R. MacFarlane, *Adv. Mater.*, 2015, **27**, 1090–1096.
28 J.-F. Li, Y.-J. Zhang, S.-Y. Ding, R. Panneerselvam and Z.-Q. Tian, *Chem. Rev.*, 2017, **117**, 5002–5069.
29 S. J. Oldenburg, S. L. Westcott, R. D. Averitt and N. J. Halas, *J. Chem. Phys.*, 1999, **111**, 4729–4735.
30 L. A. Dick, A. D. McFarland, C. L. Haynes and R. P. Van Duyne, *J. Phys. Chem. B*, 2002, **106**, 853–860.
31 H. Raether, *Surface Plasmons on Smooth and Rough Surfaces and on Gratings*, Springer Berlin/Heidelberg, 1988, vol. 111, pp. 91–116.
32 P. L. Stiles, J. A. Dieringer, N. C. Shah and R. P. Van Duyne, *Annu. Rev. Anal. Chem.*, 2008, **1**, 601–626.
33 A. Boltasseva and H. A. Atwater, *Science*, 2011, **331**, 290–291.
34 G. V. Naik, V. M. Shalaev and A. Boltasseva, *Adv. Mater.*, 2013, **25**, 3264–3294.
35 S. Maier, *Plasmonics: Fundamentals and Applications*, Springer, New York, 2007.
36 K. A. Willets and R. P. Van Duyne, *Annu. Rev. Phys. Chem.*, 2007, **58**, 267–297.
37 S. Lal, N. K. Grady, J. Kundu, C. S. Levin, J. B. Lassiter and N. J. Halas, *Chem. Soc. Rev.*, 2008, **37**, 898–911.
38 M. J. Banholzer, J. E. Millstone, L. Qin and C. A. Mirkin, *Chem. Soc. Rev.*, 2008, **37**, 885–897.
39 B. Sharma, R. R. Frontiera, A.-I. Henry, E. Ringe and R. P. Van Duyne, *Mater. Today*, 2012, **15**, 16–25.
40 B. Sharma, M. F. Cardinal, S. L. Kleinman, N. G. Greeneltch, R. R. Frontiera, M. G. Blaber, G. C. Schatz and R. P. Van Duyne, *MRS Bull.*, 2013, **38**, 615–624.
41 N. J. Halas and M. Moskovits, *MRS Bull.*, 2013, **38**, 607–611.
42 M. D. Sonntag, J. M. Klingsporn, A. B. Zrimsek, B. Sharma, L. K. Ruvuna and R. P. Van Duyne, *Chem. Soc. Rev.*, 2014, **43**, 1230–1247.
43 S. Schlücker, *Angew. Chem., Int. Ed.*, 2014, **53**, 4756–4795.
44 R. M. Stöckle, Y. D. Suh, V. Deckert and R. Zenobi, *Chem. Phys. Lett.*, 2000, **318**, 131–136.
45 M. S. Anderson, *Appl. Phys. Lett.*, 2000, **76**, 3130–3132.
46 N. Hayazawa, Y. Inouye, Z. Sekkat and S. Kawata, *Opt. Commun.*, 2000, **183**, 333–336.

This journal is © The Royal Society of Chemistry 2017

Published on 29 Junie 2017. Downloaded by Fail Open on 2025-05-07 9:23:53 vm..

47 B. Pettinger, G. Picardi, R. Schuster and G. Ertl, *Electrochemistry*, 2000, **68**, 942–949.

48 B. Ren, X.-F. Lin, Z.-L. Yang, G.-K. Liu, R. F. Aroca, B.-W. Mao and Z.-Q. Tian, *J. Am. Chem. Soc.*, 2003, **125**, 9598–9599.

49 Z.-Q. Tian, Z.-L. Yang, B. Ren and D.-Y. Wu, in *Surface-Enhanced Raman Scattering*, ed. K. Kneipp, M. Moskovits and H. Kneipp, Springer Berlin Heidelberg, 2006, ch. 7, vol. 103, pp. 125–146.

50 D. B. Chase and B. A. Parkinson, *Appl. Spectrosc.*, 1988, **42**, 1186–1187.

51 S. Efrima, *J. Chem. Phys.*, 1985, **83**, 1356–1362.

52 S. Abdali and E. W. Blanch, *Chem. Soc. Rev.*, 2008, **37**, 980–992.

53 E. J. Liang, A. Weippert, J. M. Funk, A. Materny and W. Kiefer, *Chem. Phys. Lett.*, 1994, **227**, 115–120.

54 Y. Zhang, Y.-R. Zhen, O. Neumann, J. K. Day, P. Nordlander and N. J. Halas, *Nat. Commun.*, 2014, **5**, 4424.

55 R. R. Frontiera, A.-I. Henry, N. L. Gruenke and R. P. Van Duyne, *J. Phys. Chem. Lett.*, 2011, **2**, 1199–1203.

56 H. K. Wickramasinghe, M. Chaigneau, R. Yasukuni, G. Picardi and R. Ossikovski, *ACS Nano*, 2014, **8**, 3421–3426.

57 S. Nie, L. A. Lipscomb and N.-T. Yu, *Appl. Spectrosc. Rev.*, 1991, **26**, 203–276.

58 N. L. Gruenke, M. F. Cardinal, M. O. McAnally, R. R. Frontiera, G. C. Schatz and R. P. Van Duyne, *Chem. Soc. Rev.*, 2016, **45**, 2263–2290.

59 R. F. Aroca, *Phys. Chem. Chem. Phys.*, 2013, **15**, 5355–5363.

60 T. E. Furtak and J. Reyes, *Surf. Sci.*, 1980, **93**, 351–382.

61 *Surface Enhanced Raman Scattering*, ed. R. K. Chang and T. E. Furtak, Plenum Press, New York and London, 1982.

62 T. E. Furtak, *J. Electroanal. Chem.*, 1983, **150**, 375–388.

63 M. Kerker, *Acc. Chem. Res.*, 1984, **17**, 271–277.

64 H. Metiu and P. Das, *Annu. Rev. Phys. Chem.*, 1984, **35**, 507–536.

65 G. C. Schatz, *Acc. Chem. Res.*, 1984, **17**, 370–376.

66 A. Otto, in *Light Scattering in Solids IV: Electronics Scattering, Spin Effects, SERS, and Morphic Effects*, ed. M. Cardona and G. Güntherodt, Springer Berlin Heidelberg, Berlin, Heidelberg, 1984, pp. 289–418, DOI: 10.1007/3-540-11942-6_24.

67 A. Campion, *Annu. Rev. Phys. Chem.*, 1985, **36**, 549–572.

68 M. Moskovits, *Notes Rec. R. Soc.*, 2012, **66**, 195–203.

69 C. G. Blatchford, J. R. Campbell and J. A. Creighton, *Surf. Sci.*, 1982, **120**, 435–455.

70 J. A. Creighton, *Notes Rec. R. Soc.*, 2010, **64**, 175–183.

71 Y. J. Chen, W. P. Chen and E. Burstein, *Phys. Rev. Lett.*, 1976, **36**, 1207–1210.

72 R. Dornhaus, R. E. Benner, R. K. Chang and I. Chabay, *Surf. Sci.*, 1980, **101**, 367–373.

73 P. W. Barber, R. K. Chang and H. Massoudi, *Phys. Rev. Lett.*, 1983, **50**, 997–1000.

74 B. Pettinger, U. Wenning and H. Wetzel, *Surf. Sci.*, 1980, **101**, 409–416.

75 J. C. Tsang, J. R. Kirtley and T. N. Theis, *Solid State Commun.*, 1980, **35**, 667–670.

76 J. I. Gersten, *J. Chem. Phys.*, 1980, **72**, 5779–5780.

77 J. I. Gersten, *J. Chem. Phys.*, 1980, **72**, 5780–5781.

78 J. Gersten and A. Nitzan, *J. Chem. Phys.*, 1980, **73**, 3023–3037.

79 S. L. McCall and P. M. Platzman, *Phys. Rev. B: Condens. Matter Mater. Phys.*, 1980, **22**, 1660–1662.

80 S. L. McCall, P. M. Platzman and P. A. Wolff, *Phys. Lett. A*, 1980, **77**, 381–383.

81 M. Kerker, *Appl. Opt.*, 1979, **18**, 1180–1189.

82 M. Kerker, D.-S. Wang and H. Chew, *Appl. Opt.*, 1980, **19**, 4159–4174.

83 P. K. Aravind, A. Nitzan and H. Metiu, *Surf. Sci.*, 1981, **110**, 189–204.

84 P. K. Aravind and H. Metiu, *Surf. Sci.*, 1983, **124**, 506–528.

85 U. Laor and G. C. Schatz, *Chem. Phys. Lett.*, 1981, **82**, 566–570.

86 U. Laor and G. C. Schatz, *J. Chem. Phys.*, 1982, **76**, 2888–2899.

87 M. J. Dignam and M. Moskovits, *J. Chem. Soc., Faraday Trans. 2*, 1973, **69**, 65–78.

88 H. Xu, E. J. Bjerneld, M. Käll and L. Börjesson, *Phys. Rev. Lett.*, 1999, **83**, 4357–4360.

89 F. W. King, R. P. Van Duyne and G. C. Schatz, *J. Chem. Phys.*, 1978, **69**, 4472–4481.

90 C. M. Teodorescu, *Phys. Chem. Chem. Phys.*, 2015, **17**, 21302–21314.

91 B. N. J. Persson, *Chem. Phys. Lett.*, 1981, **82**, 561–565.

92 S. Efrima and H. Metiu, *J. Chem. Phys.*, 1979, **70**, 2297–2309.

93 S. Efrima and H. Metiu, *Surf. Sci.*, 1980, **92**, 417–432.

94 H. Ueba and S. Ichimura, *J. Chem. Phys.*, 1981, **74**, 3070–3075.

95 H. Ueba, S. Ichimura and H. Yamada, *Surf. Sci.*, 1982, **119**, 433–448.

96 J. R. Lombardi, R. L. Birke, T. Lu and J. Xu, *J. Chem. Phys.*, 1986, **84**, 4174–4180.

97 D. Roy and T. E. Furtak, *Chem. Phys. Lett.*, 1986, **124**, 299–303.

98 J. F. Arenas, M. S. Woolley, J. C. Otero and J. I. Marcos, *J. Phys. Chem.*, 1996, **100**, 3199–3206.

99 D. Y. Wu, M. Hayashi, S. H. Lin and Z. Q. Tian, *Spectrochim. Acta, Part A*, 2004, **60**, 137–146.

100 L. Zhao, L. Jensen and G. C. Schatz, *J. Am. Chem. Soc.*, 2006, **128**, 2911–2919.

101 D.-Y. Wu, X.-M. Liu, S. Duan, X. Xu, B. Ren, S.-H. Lin and Z.-Q. Tian, *J. Phys. Chem. C*, 2008, **112**, 4195–4204.

102 A. Otto, I. Mrozek, H. Grabhorn and W. Akemann, *J. Phys.: Condens. Matter*, 1992, **4**, 1143–1212.

103 A. Otto, M. Lust, A. Pucci and G. Meyer, *Can. J. Anal. Sci. Spectrosc.*, 2007, **52**, 150–171.

104 L. Jensen, C. M. Aikens and G. C. Schatz, *Chem. Soc. Rev.*, 2008, **37**, 1061–1073.

105 R. H. Ritchie, *Phys. Rev.*, 1957, **106**, 874–881.

106 C. J. Powell and J. B. Swan, *Phys. Rev.*, 1960, **118**, 640–643.

107 E. Kretschmann and H. Raether, *Z. Naturforsch., A: Phys. Sci.*, 1968, **23**, 2135–2136.

108 A. Otto, *Z. Phys. A: Hadrons Nucl.*, 1968, **216**, 398–410.

109 U. Kreibig and P. Zacharias, *Z. Phys. A: Hadrons Nucl.*, 1970, **231**, 128–143.

Published on 29 Junie 2017. Downloaded by Fail Open on 2025-05-07 9:23:53 vm..

110 H. Ueba, *Surf. Sci.*, 1983, **131**, 347–366.

111 T. E. Furtak and D. Roy, *Phys. Rev. Lett.*, 1983, **50**, 1301–1304.

112 Z.-Q. Tian, *Faraday Discuss.*, 2006, **132**, 309–319.

113 S.-Y. Ding, X.-M. Zhang, B. Ren and Z.-Q. Tian, *Encyclopedia of Analytical Chemistry*, John Wiley & Sons, Ltd, 2014, DOI: 10.1002/9780470027318.a9276.

114 D.-Y. Wu, B. Ren, Y.-X. Jiang, X. Xu and Z.-Q. Tian, *J. Phys. Chem. A*, 2002, **106**, 9042–9052.

115 Z.-Q. Tian, B. Ren and D.-Y. Wu, *J. Phys. Chem. B*, 2002, **106**, 9463–9483.

116 A. Vivoni, R. L. Birke, R. Foucault and J. R. Lombardi, *J. Phys. Chem. B*, 2003, **107**, 5547–5557.

117 S. M. Morton and L. Jensen, *J. Am. Chem. Soc.*, 2009, **131**, 4090–4098.

118 S.-Y. Ding, B.-J. Liu, Q.-N. Jiang, D.-Y. Wu, B. Ren, X. Xu and Z.-Q. Tian, *Chem. Commun.*, 2012, **48**, 4962–4964.

119 K. Iida, M. Noda and K. Nobusada, *J. Chem. Phys.*, 2014, **141**, 124124.

120 V. R. Rojas and F. Claro, *J. Chem. Phys.*, 1993, **98**, 998–1006.

121 T. Itoh, K. Yoshida, V. Biju, Y. Kikkawa, M. Ishikawa and Y. Ozaki, *Phys. Rev. B: Condens. Matter Mater. Phys.*, 2007, **76**, 085405.

122 L. K. Ausman and G. C. Schatz, *J. Chem. Phys.*, 2009, **131**, 084708.

123 K.-i. Yoshida, T. Itoh, H. Tamaru, V. Biju, M. Ishikawa and Y. Ozaki, *Phys. Rev. B: Condens. Matter Mater. Phys.*, 2010, **81**, 115406.

124 L. Novotny and B. Hecht, *Principles of Nano-Optics, second edition*, Cambridge, New York, 2012.

125 L. K. Ausman, S. Li and G. C. Schatz, *J. Phys. Chem. C*, 2012, **116**, 17318–17327.

126 M. Moskovits and J. S. Suh, *J. Phys. Chem.*, 1984, **88**, 5526–5530.

127 J. Zhao, A. O. Pinchuk, J. M. McMahon, S. Li, L. K. Ausman, A. L. Atkinson and G. C. Schatz, *Acc. Chem. Res.*, 2008, **41**, 1710–1720.

128 C. F. Bohren and D. R. Huffman, *Absorption and Scattering of Light by Small Particles*, Wiley-VCH Verlag GmbH, New York, 1998.

129 V. M. Shalaev and A. K. Sarychev, *Phys. Rev. B: Condens. Matter Mater. Phys.*, 1998, **57**, 13265–13288.

130 H. Xu, J. Aizpurua, M. Käll and P. Apell, *Phys. Rev. E: Stat. Phys., Plasmas, Fluids, Relat. Interdiscip. Top.*, 2000, **62**, 4318–4324.

131 J. Jiang, K. Bosnick, M. Maillard and L. Brus, *J. Phys. Chem. B*, 2003, **107**, 9964–9972.

132 M. Moskovits, *J. Raman Spectrosc.*, 2005, **36**, 485–496.

133 E. C. Le Ru, P. G. Etchegoin and M. Meyer, *J. Chem. Phys.*, 2006, **125**, 204701.

134 J.-F. Li, S.-Y. Ding, Z.-L. Yang, M.-L. Bai, J. R. Anema, X. Wang, A. Wang, D.-Y. Wu, B. Ren, S.-M. Hou, T. Wandlowski and Z.-Q. Tian, *J. Am. Chem. Soc.*, 2011, **133**, 15922–15925.

135 J. M. McMahon, S. Li, L. K. Ausman and G. C. Schatz, *J. Phys. Chem. C*, 2012, **116**, 1627–1637.

136 A. Moreau, C. Ciraci, J. J. Mock, R. T. Hill, Q. Wang, B. J. Wiley, A. Chilkoti and D. R. Smith, *Nature*, 2012, **492**, 86–89.

137 B. Pettinger, P. Schambach, C. J. Villagómez and N. Scott, *Annu. Rev. Phys. Chem.*, 2012, **63**, 379–399.

138 S. L. Kleinman, R. R. Frontiera, A.-I. Henry, J. A. Dieringer and R. P. Van Duyne, *Phys. Chem. Chem. Phys.*, 2013, **15**, 21–36.

139 H. Wei and H. Xu, *Nanoscale*, 2013, **5**, 10794–10805.

140 A. Shiohara, Y. Wang and L. M. Liz-Marzán, *J. Photochem. Photobiol., C*, 2014, **21**, 2–25.

141 Y. Fang, N.-H. Seong and D. D. Dlott, *Science*, 2008, **321**, 388–392.

142 C. E. Talley, J. B. Jackson, C. Oubre, N. K. Grady, C. W. Hollars, S. M. Lane, T. R. Huser, P. Nordlander and N. J. Halas, *Nano Lett.*, 2005, **5**, 1569–1574.

143 J. M. McLellan, A. Siekkinen, J. Chen and Y. Xia, *Chem. Phys. Lett.*, 2006, **427**, 122–126.

144 B. J. Wiley, Y. Chen, J. M. McLellan, Y. Xiong, Z.-Y. Li, D. Ginger and Y. Xia, *Nano Lett.*, 2007, **7**, 1032–1036.

145 J. Fang, S. Liu and Z. Li, *Biomaterials*, 2011, **32**, 4877–4884.

146 K. A. Bosnick, H. M. Wang, T. L. Haslett and M. Moskovits, *J. Phys. Chem. C*, 2016, **120**, 20506–20511.

147 G. Chen, Y. Wang, L. H. Tan, M. Yang, L. S. Tan, Y. Chen and H. Chen, *J. Am. Chem. Soc.*, 2009, **131**, 4218–4219.

148 D.-K. Lim, K.-S. Jeon, H. M. Kim, J.-M. Nam and Y. D. Suh, *Nat. Mater.*, 2010, **9**, 60–67.

149 S. L. Kleinman, E. Ringe, N. Valley, K. L. Wustholz, E. Phillips, K. A. Scheidt, G. C. Schatz and R. P. Van Duyne, *J. Am. Chem. Soc.*, 2011, **133**, 4115–4122.

150 V. V. Thacker, L. O. Herrmann, D. O. Sigle, T. Zhang, T. Liedl, J. J. Baumberg and U. F. Keyser, *Nat. Commun.*, 2014, **5**, 3448.

151 J. P. Camden, J. A. Dieringer, Y. Wang, D. J. Masiello, L. D. Marks, G. C. Schatz and R. P. Van Duyne, *J. Am. Chem. Soc.*, 2008, **130**, 12616–12617.

152 K. L. Wustholz, A.-I. Henry, J. M. McMahon, R. G. Freeman, N. Valley, M. E. Piotti, M. J. Natan, G. C. Schatz and R. P. Van Duyne, *J. Am. Chem. Soc.*, 2010, **132**, 10903–10910.

153 L. Yang, P. Li, H. Liu, X. Tang and J. Liu, *Chem. Soc. Rev.*, 2015, **44**, 2837–2848.

154 S.-Y. Chen and A. A. Lazarides, *J. Phys. Chem. C*, 2009, **113**, 12167–12175.

155 N. Gandra, A. Abbas, L. Tian and S. Singamaneni, *Nano Lett.*, 2012, **12**, 2645–2651.

156 H. Wang, C. S. Levin and N. J. Halas, *J. Am. Chem. Soc.*, 2005, **127**, 14992–14993.

157 M. P. Cecchini, V. A. Turek, J. Paget, A. A. Kornyshev and J. B. Edel, *Nat. Mater.*, 2013, **12**, 165–171.

158 B. Peng, G. Li, D. Li, S. Dodson, Q. Zhang, J. Zhang, Y. H. Lee, H. V. Demir, X. Yi Ling and Q. Xiong, *ACS Nano*, 2013, **7**, 5993–6000.

159 E. Hao and G. C. Schatz, *J. Chem. Phys.*, 2004, **120**, 357–366.

160 J. M. McMahon, S. K. Gray and G. C. Schatz, *Phys. Rev. B: Condens. Matter Mater. Phys.*, 2011, **83**, 115428.

This journal is © The Royal Society of Chemistry 2017

Published on 29 Junie 2017. Downloaded by Fail Open on 2025-05-07 9:23:53 vm..

161 H. Fischer and O. J. F. Martin, *Opt. Express*, 2008, **16**, 9144–9154.

162 A. Ahmed and R. Gordon, *Nano Lett.*, 2011, **11**, 1800–1803.

163 A. Ahmed and R. Gordon, *Nano Lett.*, 2012, **12**, 2625–2630.

164 D. Wang, W. Zhu, Y. Chu and K. B. Crozier, *Adv. Mater.*, 2012, **24**, 4376–4380.

165 D. Wang, W. Zhu, M. D. Best, J. P. Camden and K. B. Crozier, *Nano Lett.*, 2013, **13**, 2194–2198.

166 F. M. Huang, D. Wilding, J. D. Speed, A. E. Russell, P. N. Bartlett and J. J. Baumberg, *Nano Lett.*, 2011, **11**, 1221–1226.

167 B. Joshi, A. Chakrabarty and Q. H. Wei, *IEEE Trans. Nanotechnol.*, 2010, **9**, 701–707.

168 R. Esteban, G. Aguirregabiria, A. G. Borisov, Y. M. Wang, P. Nordlander, G. W. Bryant and J. Aizpurua, *ACS Photonics*, 2015, **2**, 295–305.

169 Y. Kurokawa and H. T. Miyazaki, *Phys. Rev. B: Condens. Matter Mater. Phys.*, 2007, **75**, 035411.

170 B. P. Joshi and Q.-H. Wei, *Opt. Express*, 2008, **16**, 10315–10322.

171 J. A. Dionne, L. A. Sweatlock, H. A. Atwater and A. Polman, *Phys. Rev. B: Condens. Matter Mater. Phys.*, 2006, **73**, 035407.

172 S. I. Bozhevolnyi and T. Søndergaard, *Opt. Express*, 2007, **15**, 10869–10877.

173 W. Zhu and K. B. Crozier, *Nat. Commun.*, 2014, **5**, 5228.

174 J. Zuloaga, E. Prodan and P. Nordlander, *Nano Lett.*, 2009, **9**, 887–891.

175 K. J. Savage, M. M. Hawkeye, R. Esteban, A. G. Borisov, J. Aizpurua and J. J. Baumberg, *Nature*, 2012, **491**, 574–577.

176 J. A. Scholl, A. García-Etxarri, A. L. Koh and J. A. Dionne, *Nano Lett.*, 2013, **13**, 564–569.

177 S. F. Tan, L. Wu, J. K. W. Yang, P. Bai, M. Bosman and C. A. Nijhuis, *Science*, 2014, **343**, 1496–1499.

178 R. Esteban, A. G. Borisov, P. Nordlander and J. Aizpurua, *Nat. Commun.*, 2012, **3**, 825.

179 W.-H. Park, S.-H. Ahn and Z. H. Kim, *ChemPhysChem*, 2008, **9**, 2491–2494.

180 R. T. Hill, J. J. Mock, Y. Urzhumov, D. S. Sebba, S. J. Oldenburg, S.-Y. Chen, A. A. Lazarides, A. Chilkoti and D. R. Smith, *Nano Lett.*, 2010, **10**, 4150–4154.

181 S. Mubeen, S. Zhang, N. Kim, S. Lee, S. Krämer, H. Xu and M. Moskovits, *Nano Lett.*, 2012, **12**, 2088–2094.

182 L. Li, T. Hutter, U. Steiner and S. Mahajan, *Analyst*, 2013, **138**, 4574–4578.

183 J. Shen, J. Wang, C. Zhang, C. Min, H. Fang, L. Du, S. Zhu and X.-C. Yuan, *Appl. Phys. Lett.*, 2013, **103**, 191119.

184 J. Long, H. Yi, H. Li, Z. Lei and T. Yang, *Sci. Rep.*, 2016, **6**, 33218.

185 D. O. Sigle, S. Kasera, L. O. Herrmann, A. Palma, B. de Nijs, F. Benz, S. Mahajan, J. J. Baumberg and O. A. Scherman, *J. Phys. Chem. Lett.*, 2016, **7**, 704–710.

186 C. Ciracì, R. T. Hill, J. J. Mock, Y. Urzhumov, A. I. Fernández-Domínguez, S. A. Maier, J. B. Pendry, A. Chilkoti and D. R. Smith, *Science*, 2012, **337**, 1072–1074.

187 P. Nordlander and E. Prodan, *Nano Lett.*, 2004, **4**, 2209–2213.

188 M. Rycenga, X. Xia, C. H. Moran, F. Zhou, D. Qin, Z.-Y. Li and Y. Xia, *Angew. Chem., Int. Ed.*, 2011, **50**, 5473–5477.

189 P. T. Bowen and D. R. Smith, *Phys. Rev. B: Condens. Matter Mater. Phys.*, 2014, **90**, 195402.

190 C. Tserkezis, R. Esteban, D. O. Sigle, J. Mertens, L. O. Herrmann, J. J. Baumberg and J. Aizpurua, *Phys. Rev. A: At., Mol., Opt. Phys.*, 2015, **92**, 053811.

191 R. Chikkaraddy, X. Zheng, F. Benz, L. J. Brooks, B. de Nijs, C. Carnegie, M.-E. Kleemann, J. Mertens, R. W. Bowman, G. A. E. Vandenbosch, V. V. Moshchalkov and J. J. Baumberg, *ACS Photonics*, 2017, **4**, 469–475.

192 F. Minkowski, F. Wang, A. Chakrabarty and Q.-H. Wei, *Appl. Phys. Lett.*, 2014, **104**, 021111.

193 Y.-F. Huang, C.-Y. Li, I. Broadwell, J.-F. Li, D.-Y. Wu, B. Ren and Z.-Q. Tian, *Electrochim. Acta*, 2011, **56**, 10652–10657.

194 S.-Y. Ding, J. Yi, J.-F. Li and Z.-Q. Tian, *Surf. Sci.*, 2015, **631**, 73–80.

195 D. P. Butcher, S. P. Boulos, C. J. Murphy, R. C. Ambrosio and A. A. Gewirth, *J. Phys. Chem. C*, 2012, **116**, 5128–5140.

196 N. R. Honesty and A. A. Gewirth, *J. Raman Spectrosc.*, 2012, **43**, 46–50.

197 A. V. Rudnev, A. Kuzume, Y. Fu and T. Wandlowski, *Electrochim. Acta*, 2014, **133**, 132–145.

198 C.-Y. Li, J.-C. Dong, X. Jin, S. Chen, R. Panneerselvam, A. V. Rudnev, Z.-L. Yang, J.-F. Li, T. Wandlowski and Z.-Q. Tian, *J. Am. Chem. Soc.*, 2015, **137**, 7648–7651.

199 S. Chen, L.-Y. Meng, H.-Y. Shan, J.-F. Li, L. Qian, C. T. Williams, Z.-L. Yang and Z.-Q. Tian, *ACS Nano*, 2016, **10**, 581–587.

200 R. Zhang, Y. Zhang, Z. C. Dong, S. Jiang, C. Zhang, L. G. Chen, L. Zhang, Y. Liao, J. Aizpurua, Y. Luo, J. L. Yang and J. G. Hou, *Nature*, 2013, **498**, 82–86.

201 Z. L. Yang, J. Aizpurua and H. X. Xu, *J. Raman Spectrosc.*, 2009, **40**, 1343–1348.

202 M. Micic, N. Klymyshyn, Y. D. Suh and H. P. Lu, *J. Phys. Chem. B*, 2003, **107**, 1574–1584.

203 A. L. Demming, F. Festy and D. Richards, *J. Chem. Phys.*, 2005, **122**, 184716.

204 A. Downes, D. Salter and A. Elfick, *J. Phys. Chem. B*, 2006, **110**, 6692–6698.

205 R. M. Roth, N. C. Panoiu, M. M. Adams, R. M. Osgood, C. C. Neacsu and M. B. Raschke, *Opt. Express*, 2006, **14**, 2921–2931.

206 N. Kazemi-Zanjani, S. Vedraine and F. Lagugne-Labarthet, *Opt. Express*, 2013, **21**, 25271–25276.

207 L. Meng, Z. Yang, J. Chen and M. Sun, *Sci. Rep.*, 2015, **5**, 9240.

208 S. F. Becker, M. Esmann, K. Yoo, P. Gross, R. Vogelgesang, N. Park and C. Lienau, *ACS Photonics*, 2016, **3**, 223–232.

209 L. Meng, T. X. Huang, X. Wang, S. Chen, Z. Yang and B. Ren, *Opt. Express*, 2015, **23**, 13804–13813.

210 X. D. Cui, W. H. Zhang, B. S. Yeo, R. Zenobi, C. Hafner and D. Erni, *Opt. Express*, 2007, **15**, 8309–8316.

211 C. Huber, A. Trugler, U. Hohenester, Y. Prior and W. Kautek, *Phys. Chem. Chem. Phys.*, 2014, **16**, 2289–2296.

212 J. A. Dieringer, A. D. McFarland, N. C. Shah, D. A. Stuart, A. V. Whitney, C. R. Yonzon, M. A. Young, X. Zhang and R. P. Van Duyne, *Faraday Discuss.*, 2006, **132**, 9–26.

Published on 29 Junie 2017. Downloaded by Fail Open on 2025-05-07 9:23:53 vm..

213 K. M. Kosuda, J. M. Bingham, K. L. Wustholz and R. P. Van Duyne, in *Comprehensive Nanoscience and Technology*, Editors-in-Chief: ed. L. A. David, D. S. Gregory and P. W. Gary, Academic Press, Amsterdam, 2011, pp. 263–301.

214 S. L. Kleinman, B. Sharma, M. G. Blaber, A.-I. Henry, N. Valley, R. G. Freeman, M. J. Natan, G. C. Schatz and R. P. Van Duyne, *J. Am. Chem. Soc.*, 2012, **135**, 301–308.

215 E. C. Le, Ru, C. Galloway and P. G. Etchegoin, *Phys. Chem. Chem. Phys.*, 2006, **8**, 3083–3087.

216 B. Luk'yanchuk, N. I. Zheludev, S. A. Maier, N. J. Halas, P. Nordlander, H. Giessen and C. T. Chong, *Nat. Mater.*, 2010, **9**, 707–715.

217 N. J. Halas, S. Lal, W.-S. Chang, S. Link and P. Nordlander, *Chem. Rev.*, 2011, **111**, 3913–3961.

218 M. Rahmani, B. Luk'yanchuk and M. Hong, *Laser Photonics Rev.*, 2013, **7**, 329–349.

219 B. Gallinet and O. J. F. Martin, *Phys. Rev. B: Condens. Matter Mater. Phys.*, 2011, **83**, 235427.

220 B. Gallinet, T. Siegfried, H. Sigg, P. Nordlander and O. J. F. Martin, *Nano Lett.*, 2013, **13**, 497–503.

221 B. Gallinet and O. J. F. Martin, *ACS Nano*, 2011, **5**, 8999–9008.

222 B. Gallinet and O. J. F. Martin, *ACS Nano*, 2013, **7**, 6978–6987.

223 B. Gallinet and O. J. F. Martin, *Opt. Express*, 2011, **19**, 22167–22175.

224 Y. Chu, D. Wang, W. Zhu and K. B. Crozier, *Opt. Express*, 2011, **19**, 14919–14928.

225 J. Ye, F. Wen, H. Sobhani, J. B. Lassiter, P. V. Dorpe, P. Nordlander and N. J. Halas, *Nano Lett.*, 2012, **12**, 1660–1667.

226 X. Hua, D. V. Voronine, C. W. Ballmann, A. M. Sinyukov, A. V. Sokolov and M. O. Scully, *Phys. Rev. A: At., Mol., Opt. Phys.*, 2014, **89**, 043841.

227 L. E. Buchanan, N. L. Gruenke, M. O. McAnally, B. Negru, H. E. Mayhew, V. A. Apkarian, G. C. Schatz and R. P. Van Duyne, *J. Phys. Chem. Lett.*, 2016, **7**, 4629–4634.

228 S. Jiang, Y. Zhang, R. Zhang, C. Hu, M. Liao, Y. Luo, J. Yang, Z. Dong and J. G. Hou, *Nat. Nanotechnol.*, 2015, **10**, 865–869.

229 S. Duan, G. Tian, Y. Ji, J. Shao, Z. Dong and Y. Luo, *J. Am. Chem. Soc.*, 2015, **137**, 9515–9518.

230 C. Zhang, B.-Q. Chen and Z.-Y. Li, *J. Phys. Chem. C*, 2015, **119**, 11858–11871.

231 S. Duan, G. Tian and Y. Luo, *Angew. Chem., Int. Ed.*, 2016, **55**, 1041–1045.

232 J.-H. Tian, B. Liu, X. Li, Z.-L. Yang, B. Ren, S.-T. Wu, N. Tao and Z.-Q. Tian, *J. Am. Chem. Soc.*, 2006, **128**, 14748–14749.

233 D. R. Ward, N. J. Halas, J. W. Ciszek, J. M. Tour, Y. Wu, P. Nordlander and D. Natelson, *Nano Lett.*, 2008, **8**, 919–924.

234 Z. Liu, S.-Y. Ding, Z.-B. Chen, X. Wang, J.-H. Tian, J. R. Anema, X.-S. Zhou, D.-Y. Wu, B.-W. Mao, X. Xu, B. Ren and Z.-Q. Tian, *Nat. Commun.*, 2011, **2**, 305.

235 R. Matsushita and M. Kiguchi, *Phys. Chem. Chem. Phys.*, 2015, **17**, 21254–21260.

236 M. Galperin, M. A. Ratner and A. Nitzan, *J. Chem. Phys.*, 2009, **130**, 144109.

237 M. Galperin, *Chem. Soc. Rev.*, 2017, DOI: 10.1039/C7CS00067G.

238 S. Zhang, K. Bao, N. J. Halas, H. Xu and P. Nordlander, *Nano Lett.*, 2011, **11**, 1657–1663.

239 S.-Y. Ding, E.-M. You, J. Yi, J.-F. Li and Z.-Q. Tian, *Faraday Discuss.*, 2017, DOI: 10.1039/C7FD00144D.

240 J. Yelk, M. Sukharev and T. Seideman, *J. Chem. Phys.*, 2008, **129**, 064706.

241 R. R. Andrawis, M. A. Swillam, M. A. El-Gamal and E. A. Soliman, *Appl. Opt.*, 2016, **55**, 2780–2790.

242 U. Fano, *Phys. Rev.*, 1961, **124**, 1866–1878.

243 J. R. Lombardi and R. L. Birke, *J. Chem. Phys.*, 2012, **136**, 144704.

244 H. Chen, J. M. McMahon, M. A. Ratner and G. C. Schatz, *J. Phys. Chem. C*, 2010, **114**, 14384–14392.

245 J. Mullin, N. Valley, M. G. Blaber and G. C. Schatz, *J. Phys. Chem. A*, 2012, **116**, 9574–9581.

246 G. C. Schatz and N. A. Valley, *Frontiers of Surface-Enhanced Raman Scattering*, John Wiley & Sons, Ltd, 2014, pp. 1–17, DOI: 10.1002/9781118703601.ch1.

247 C. Yam, L. Meng, Y. Zhang and G. Chen, *Chem. Soc. Rev.*, 2015, **44**, 1763–1776.

248 S. M. Morton and L. Jensen, *J. Chem. Phys.*, 2011, **135**, 134103.

249 J. L. Payton, S. M. Morton, J. E. Moore and L. Jensen, *Acc. Chem. Res.*, 2014, **47**, 88–99.

250 S. Corni, *Handbook of Molecular Plasmonics*, Pan Stanford Publishing, 2013, DOI: 10.1201/b15328-7.

251 D. J. Masiello and G. C. Schatz, *Phys. Rev. A: At., Mol., Opt. Phys.*, 2008, **78**, 042505.

252 P. Roelli, C. Galland, N. Piro and T. J. Kippenberg, *Nat. Nanotechnol.*, 2016, **11**, 164–169.

253 M. K. Schmidt, R. Esteban, A. González-Tudela, G. Giedke and J. Aizpurua, *ACS Nano*, 2016, **10**, 6291–6298.

254 A. Otto, *J. Raman Spectrosc.*, 2005, **36**, 497–509.

This journal is © The Royal Society of Chemistry 2017